STATE OF THE CLIMATE IN 2021

THE ARCTIC

R. Thoman, M. L. Druckenmiller, and T. Moon, Eds.

Special Online Supplement to the *Bulletin of the American Meteorological Society*, Vol. 103, No. 8, August 2022

https://doi.org/10.1175/BAMS-D-22-0082.1.

Corresponding author: Richard Thoman / rthoman@alaska.edu

STATE OF THE CLIMATE IN 2021

The Arctic

Editors

Jessica Blunden
Tim Boyer

Chapter Editors

Freya Aldred
Peter Bissolli
Kyle R. Clem
Howard J. Diamond
Matthew L. Druckenmiller
Robert J. H. Dunn
Catherine Ganter
Nadine Gobron
Gregory C. Johnson
Rick Lumpkin
Ademe Mekonnen
John B. Miller
Twila A. Moon
Marilyn N. Raphael
Ahira Sánchez-Lugo
Carl J. Schreck III
Richard L. Thoman
Kate M. Willett
Zhiwei Zhu

Technical Editor

Laura Ohlmann

BAMS Special Editor for Climate

Michael A. Alexander

American Meteorological Society

Cover credit:
Cover image courtesy of Gay Sheffield. The mountain at Cape Prince of Wales in the background with sea ice breaking up. Sky is cloudy and tinted orange from smoke from wildfires in Chukotka, Russia.

The Arctic is one chapter from the *State of the Climate in 2021* annual report and is available from https://doi.org/10.1175/BAMS-D-22-0082.1. Compiled by NOAA's National Centers for Environmental Information, *State of the Climate in 2021* is based on contributions from scientists from around the world. It provides a detailed update on global climate indicators, notable weather events, and other data collected by environmental monitoring stations and instruments located on land, water, ice, and in space.
The full report is available from https://doi.org/10.1175/2022BAMSStateoftheClimate.1.

How to cite this document:

Citing the complete report:
Blunden, J. and T. Boyer, Eds., 2022: "State of the Climate in 2021". *Bull. Amer. Meteor. Soc.*, **103** (8), Si–S465, https://doi.org/10.1175/2022BAMSStateoftheClimate.1.

Citing this chapter:
Thoman, R., M. L. Druckenmiller, and T. Moon, Eds., 2022: "State of the Climate in 2021"]. *Bull. Amer. Meteor. Soc.*, **103** (8), S257–S306, https://doi.org/10.1175/BAMS-D-22-0082.1.

Citing a section (example):
Meier, W. N., D. Perovich, S. Farrell, C. Haas, S. Hendricks, A. Petty, M. Webster, D. Divine, S. Gerland, L. Kaleschke, R. Ricker, A. Steer, X. Tian-Kunze, M. Tschudi, and K. Wood, 2022: Sea ice [in "State of the Climate in 2021"]. *Bull. Amer. Meteor. Soc.*, **103** (8), S270–S273, https://doi.org/10.1175/BAMS-D-22-0082.1.

Editor and Author Affiliations (alphabetical by name)

Andreassen, L. M., Section for Glaciers, Snow and Ice, Norwegian Water Resources and Energy Directorate, Oslo, Norway
Baker, E., United States Geological Survey, Alaska Science Center, Anchorage, Alaska
Ballinger, Thomas J., International Arctic Research Center, University of Alaska Fairbanks, Fairbanks, Alaska
Berner, Logan T., School of Informatics, Computing, and Cyber Systems, Northern Arizona University, Flagstaff, Arizona
Bernhard, Germar H., Biospherical Instruments Inc., San Diego, California, United States
Bhatt, Uma S., Geophysical Institute, University of Alaska Fairbanks, Fairbanks, Alaska
Bjerke, Jarle W., Norwegian Institute for Nature Research, FRAM and High North Research Centre for Climate and the Environment, Tromsø, Norway
Boisvert, L.N., NASA Goddard Space Flight Center, Greenbelt, Marylamd
Box, Jason E., Geological Survey of Denmark and Greenland, Copenhagen, Denmark
Brettschneider, B., National Weather Service Alaska Region, NOAA, Anchorage, Alaska
Burgess, D., Geological Survey of Canada, Ottawa, Ontario, Canada
Butler, Amy H., NOAA Chemical Sciences Laboratory, Boulder, Colorado
Cappelen, John, Danish Meteorological Institute, Copenhagen, Denmark
Christiansen, Hanne H., Geology Department, University Centre in Svalbard, The University Center in Svalbard, Longyearbyen, Norway
Decharme, B., Centre National de Recherches Météorologiques, Toulouse, France
Derksen, C., Climate Research Division, Environment and Climate Change Canada, Downsview, Ontario, Canada
Divine, Dmitry, Norwegian Polar Institute, Fram Centre, Tromsø, Norway
Drozdov, D. S., Earth Cryosphere Institute, and Tyumen State University, Tyumen, Russia
Druckenmiller, Matthew L., National Snow and Ice Data Center, Cooperative Institute for Research in Environmental Sciences, University of Colorado, Boulder, Colorado
Elias Chereque, A., Department of Physics, University of Toronto, Toronto, Canada
Epstein, Howard E., Department of Environmental Sciences, University of Virginia, Charlottesville, Virginia
Farrell, Sinead L., Department of Geographical Sciences, University of Maryland, College Park, Maryland
Fausto, Robert S., Geological Survey of Denmark and Greenland, Copenhagen, Denmark
Fettweis, Xavier, SPHERES research unit, University of Liège, Liège, Belgium
Fioletov, Vitali E., Environment and Climate Change Canada, Toronto, Ontario, Canada
Forbes, Bruce C., Arctic Centre, University of Lapland, Rovaniemi, Finland
Frost, Gerald V., ABR, Inc. Environmental Research & Services, Fairbanks, Alaska
Gerland, Sebastian, Norwegian Polar Institute, Fram Centre, Tromsø, Norway
Goetz, Scott J., School of Informatics, Computing, and Cyber Systems, Northern Arizona University, Flagstaff, Arizona
Grooß, Jens-Uwe, Forschungszentrum Jülich, Jülich, Germany
Haas, Christian, Alfred Wegener Institute, Helmholtz Centre for Polar and Marine Research, Bremerhaven, Germany
Hanna, Edward, School of Geography and Lincoln Centre for Water and Planetary Health, University of Lincoln, Lincoln, United Kingdom
Hanssen-Bauer, Inger, Norwegian Meteorological Institute, Blindern, Oslo, Norway
Heijmans, M. M. P. D., Department of Environmental Sciences, Wageningen University & Research, Wageningen, Netherlands
Hendricks, Stefan, Alfred Wegener Institute, Helmholtz Centre for Polar and Marine Research, Bremerhaven, Germany
Ialongo, Iolanda, Finnish Meteorological Institute, Helsinki, Finland
Isaksen, K., Norwegian Meteorlogical Institute, Blindern, Oslo, Norway
Jensen, C. D., Danish Meteorological Survey, Copenhagen, Denmark
Johnsen, Bjørn, Norwegian Radiation and Nuclear Safety, Østerås, Norway
Kaleschke, L., Alfred Wegener Institute, Helmholtz Centre for Polar and Marine Research, Bremerhaven, Germany
Kholodov, A. L., Earth Cryosphere Institute, Tyumen Science Center, Tyumen, Russia
Kim, Seong-Joong, Korea Polar Research Institute, Incheon, Republic of Korea
Kohler, J., Norwegian Polar Institute, Tromsø, Norway
Korsgaard, Niels J., Geological Survey of Denmark and Greenland, Copenhagen, Denmark
Labe, Zachary, Colorado State University, Fort Collins, Colorado, United States
Lakkala, Kaisa, Finnish Meteorological Institute, Sodankylä, Finland
Lara, Mark J., Department of Plant Biology, University of Illinois at Urbana-Champaign, Urbana, Illinois
Lee, Simon H., Department of Applied Physics and Applied Mathematics, Columbia University, New York, New York
Loomis, Bryant, NASA Goddard Space Flight Center, Greenbelt, Maryland
Luks, B., Institute of Geophysics, Polish Academy of Sciences, Warsaw, Poland
Luojus, K., Arctic Research Centre, Finnish Meteorological Institute, Helsinki, Finland
Macander, Matthew J., ABR, Inc., Environmental Research & Services, Fairbanks, Alaska
Magnússon, R. Í, Department of Environmental Sciences, Wageningen University & Research, Wageningen, Netherlands
Malkova, G. V., Earth Cryosphere Institute, Tyumen Science Center, Tyumen, Russia
Mankoff, Kenneth D., Geological Survey of Denmark and Greenland, Copenhagen, Denmark
Manney, Gloria L., NorthWest Research Associates, Socorro, New Mexico
Meier, Walter N., National Snow and Ice Data Center, Cooperative Institute for Research in Environment Sciences at the University of Colorado, Boulder, Colorado
Moon, Twila A., National Snow and Ice Data Center, Cooperative Institute for Research in Environmental Sciences, University of Colorado, Boulder, Colorado
Mote, Thomas, Department of Geography, University of Georgia, Athens, Georgia
Mudryk, Lawrence, Climate Research Division, Environment and Climate Change Canada, Downsview, Ontario, Canada
Müller, Rolf, Forschungszentrum Jülich, Jülich, Germany
Nyland, K. E., Department of Geography, George Washington University, Washington, D.C.
Overland, James E., NOAA/OAR Pacific Marine Environmental Laboratory, Seattle, Washington
Pálsson, F., Institute of Earth Sciences, University of Iceland, Reykjavík, Iceland
Park, T., NASA Ames Research Center, Mountain View, California, and Bay Area Environmental Research Institute, Moffett Field, California
Parker, C. L., NASA Goddard Space Flight Center, Greenbelt, MD; Earth System Science Interdisciplinary Center, University of Maryland, College Park, Maryland
Perovich, Don, Thayer School of Engineering, Dartmouth College, Hanover, New Hampshire
Petty, Alek, NASA Goddard Space Flight Center, Greenbelt, Maryland
Phoenix, Gareth K., Department of Animal and Plant Sciences, University of Sheffield, Sheffield, United Kingdom
Pinzon, J. E., NASA Goddard Space Flight Center, Greenbelt, Maryland

Editor and Author Affiliations (alphabetical by name)

Ricker, Robert, Alfred Wegener Institute, Helmholtz Centre for Polar and Marine Research, Bremerhaven, Germany

Romanovsky, Vladimir E., Geophysical Institute, University of Alaska Fairbanks, Fairbanks, Alaska; Earth Cryosphere Institute, Tyumen Science Center, Tyumen, Russia

Serbin, S. P., Environmental and Climate Sciences Department, Brookhaven National Laboratory, Upton, New York

Sheffield, G., University of Alaska Fairbanks, Marine Advisory Program, Alaska Sea Grant, Nome, Alaska

Shiklomanov, Nikolai I., Department of Geography, George Washington University, Washington, D.C.

Smith, Sharon L., Geological Survey of Canada, Natural Resources Canada, Ottawa, Ontario, Canada

Stafford, K.M., Oregon State University, Marine Mammal Institute, Newport, Oregon

Steer, A., Norwegian Polar Institute, Fram Centre, Tromsø, Norway

Streletskiy, Dimitri A., Department of Geography, George Washington University, Washington, D.C.

Svendby, Tove, NILU-Norwegian Institute for Air Research, Kjeller, Norway

Tedesco, Marco, Lamont Doherty Earth Observatory, Columbia University, Palisades, New York, and NASA Goddard Institute of Space Studies, New York, New York

Thoman, Richard L., International Arctic Research Center, University of Alaska Fairbanks, Fairbanks, Alaska

Thomson, L., Queen's University, Kingston, Ontario, Canada

Thorsteinsson, T., Icelandic Meteorological Office, Reykjavík, Iceland

Tian-Kunze, X., Alfred Wegener Institute, Helmholtz Centre for Polar and Marine Research, Bremerhaven, Germany

Timmermans, Mary-Louise, Yale University, New Haven, Connecticut

Tømmervik, Hans, Norwegian Institute for Nature Research, FRAM and High North Research Centre for Climate and the Environment, Tromsø, Norway

Tschudi, Mark, Aerospace Engineering Sciences, University of Colorado, Boulder, Colorado

Tucker, C. J., Environmental and Climate Sciences Department, Brookhaven National Laboratory, Upton, New York

Walker, Donald A., Institute of Arctic Biology, University of Alaska Fairbanks, Alaska

Walsh, John E., International Arctic Research Center, University of Alaska Fairbanks, Fairbanks, Alaska

Wang, Muyin, NOAA/OAR Pacific Marine Environmental Laboratory, and Cooperative Institute for Climate, Ocean, and Ecosystem Studies, University of Washington, Seattle, Washington

Webster, Melinda, Geophysical Institute, University of Alaska Fairbanks, Fairbanks, Alaska; University of Alaska, Fairbanks, Alaska

Wehrlé, A., Institute of Geography, University of Zurich, Zurich, Switzerland

Winton, Øyvind, Geological Survey of Denmark and Greenland, Copenhagen, Denmark

Wolken, G., Alaska Division of Geological & Geophysical Surveys, Fairbanks, Alaska

Wood, K., NOAA, Pacific Marine Environmental Laboratory, Seattle, Washington

Wouters, B., Institute for Marine and Atmospheric Research, Utrecht University, Utrecht, Netherlands

Yang, D., Environmental and Climate Sciences Department, Brookhaven National Laboratory, Upton, New York; Department of Ecology and Evolution, Stony Brook University, Stony Brook, New York

Editorial and Production Team

Allen, Jessicca, Graphics Support, Cooperative Institute for Satellite Earth System Studies, North Carolina State University, Asheville, North Carolina

Hammer, Gregory, Content Team Lead, Communications and Outreach, NOAA/NESDIS National Centers for Environmental Information, Asheville, North Carolina

Love-Brotak, S. Elizabeth, Lead Graphics Production, NOAA/NESDIS National Centers for Environmental Information, Asheville, North Carolina

Misch, Deborah J., Graphics Support, Innovative Consulting and Management Services, LLC, NOAA/NESDIS National Centers for Environmental Information, Asheville, North Carolina

Ohlmann, Laura, Technical Editor, Innovative Consulting and Management Services, LLC, NOAA/NESDIS National Centers for Environmental Information, Asheville, North Carolina

Riddle, Deborah B., Graphics Support, NOAA/NESDIS National Centers for Environmental Information, Asheville, North Carolina

Veasey, Sara W., Visual Communications Team Lead, Communications and Outreach, NOAA/NESDIS National Centers for Environmental Information, Asheville, North Carolina

5. Table of Contents

*Please refer to Chapter 8 (Relevant datasets and sources) for a list of all climate variables and datasets used in this chapter for analyses, along with their websites for more information and access to the data.

5. THE ARCTIC

R. Thoman, M. L. Druckenmiller, and T. Moon, Eds.

a. Overview—R. Thoman, M. L. Druckenmiller, and T. Moon

Disruptive environmental change in the Arctic continued in 2021. While few indicators were at record levels, the ongoing trends provide a stark illustration of an Arctic that is a very different place than the Arctic of the twentieth century. Air and ocean temperatures in the Arctic are intimately linked with sea ice and are directly connected to the biological productivity of the region. Terrestrial snow cover, or the lack thereof, plays an important role in modulating air temperatures and the hydrologic cycle. During the winter, lower latitude drivers such as the El Niño-Southern Oscillation, the Madden-Julian Oscillation, and the evolution of the stratospheric polar vortex affect regional conditions and sub-seasonal variability. These processes add to the complexity of annually assessing the state of the Arctic, despite numerous examples of observed broadscale directional change across the region.

For the Arctic (poleward of 60°N) as a whole, 2021 was the coolest year since 2013. Yet, 2021 was still the 13th-warmest year on record (since 1900), highlighting the dominance of the strong warming trend in recent decades. Within the Arctic, both the European (0°–90°E) and Asian (90°E–180°) sectors each experienced spring (April–June) temperatures among their highest 10% among all springs, while the Greenland-Iceland region experienced mean temperatures in the highest 10th percentile during all seasons, except spring. Collectively, these contributed substantially to the annual temperature anomaly for the entire Arctic. Spring and summer air temperatures are linked to the strong increase in tundra vegetation productivity that emerged in the late 1990s, a phenomenon known as "the greening of the Arctic." The overall trend in circumpolar "greening" is strongly positive but recent years have seen the emergence of increased regional variability, such as strong greening on the Alaska North Slope, but "browning" in parts of northeast Asia. In 2021, the circumpolar greening index was the second highest since observations commenced in 2000, just 2.7% lower than in 2020.

Evidence for increasing Arctic precipitation (liquid and frozen) comes from the intensifying hydrologic cycle and long-term trend of increasing river discharge (Holmes et al. 2021), but has not been previously been reported in the *State of the Climate* reports. Today, advances in reanalysis now allow for regionally reliable year-round precipitation estimates (Barrett et al. 2020; Wang et al. 2019). In 2021, total precipitation was modestly higher than the 1991–2020 climatology, but on average consisted of a considerably lower percentage of snowfall, relative to the 30-year average. Timing of the seasonal transition of the predominant phase of precipitation, the terrestrial snow cover establishment in autumn and melt in spring, has profound effects on air temperatures. Similarly, the snowpack mass at the end of the accumulation season drives ecosystem and hydrologic responses during and beyond the melt season. Snow accumulation during the 2020/21 winter was near-normal across the Eurasian Arctic and above normal across the North American Arctic. Despite the absence of a significant negative trend in snow mass, spring snow extent has been persistently below normal for the last 15 years due to earlier snow melt.

The seasonal maximum sea ice extent for the Arctic is typically reached in March. In 2021, the March extent was the ninth lowest since 1979. Spring melt was rapid in the Laptev Sea, resulting in record low ice extent for May and June in this region, and the East Greenland Sea was nearly ice-free during much of the summer. This early loss of sea ice contributed to August 2021 mean

SSTs that were 1° to 3.5°C above the 1982–2010 average in the Kara, Laptev, and East Greenland Seas. In contrast, cloudy and cool weather, combined with more unusually high concentrations of multi-year ice for recent years in the Chukchi and Beaufort Seas, resulted in the 12th-lowest September mean extent in the 43-year record. Also, northern Barents Sea, Baffin Bay, and Chukchi Sea were marked by anomalously low SSTs in August 2021, up to 1°C lower than the 1982–2010 mean. Yet, near the end of the melt season in September 2021, the amount of multiyear ice remaining in the Arctic was still the second lowest on record, indicating the Arctic's sustained transition to a younger, thinner ice cover. Changes in sea ice seasonality and warming ocean ecosystems allow for expanded Arctic maritime activity, increasing pollution in the region. This takes the form of conventional "trash" and potentially toxic materials, and of increased ocean noise levels, with potential impacts to marine species, especially marine mammals for whom underwater sounds can disrupt communication that is critical to their normal activities.

Mass changes on the Greenland Ice Sheet and other Arctic glaciers and ice caps that make up the Arctic year-round terrestrial cryosphere are quite sensitive to summer temperatures. Although Greenland Ice Sheet mass loss in the 2020/21 season was about half of the 2000–21 average, the ice sheet has now lost mass every year since 1998. Extreme events during summer 2021 included a widespread melt event on 14 August, the latest on record, which produced for the first time on record (since 1989) rain at Summit Station (3216 m a.s.l.). Outside of Greenland, observations of monitored Arctic glaciers and ice caps from 2020 and 2021 show regional and inter-annual variations in mass change, with a continuing trend of significant ice loss throughout the Arctic, especially in Alaska and Arctic Canada.

Permafrost refers to ground materials that remain at or below 0°C for at least two consecutive years and underlies extensive regions of the high-latitude landscape. Permafrost temperatures continue to increase across the Arctic. Greater increases in permafrost temperature are generally observed in colder permafrost at higher latitudes, where the largest increase in air temperature has been observed. Permafrost temperatures in 2021 were generally higher than those observed in 2020 and the highest on record at many monitoring sites. However, some recent, slight cooling occurred at a few sites as well.

During the polar night, the very cold stratospheric polar vortex facilitates ozone depletion through chemical reactions that are inactive at temperatures higher than –78°C, while strong anomalies in stratospheric temperatures and winds can descend to the lower stratosphere where they persist for many weeks, affecting both the stratospheric ozone layer and the jet stream. Early stratospheric polar vortex formation in November 2020, which was conducive to ozone depletion, was cut short by a major Sudden Stratospheric Warming event in January 2021. Another result was that the average Arctic total ozone columns (ozone amounts integrated from Earth's surface to the top of the atmosphere) in March 2021 were close to normal, and spring UV index values were generally within two standard deviations of the 2005–20 mean.

(This chapter includes a focus on glaciers and ice caps outside Greenland, section 5f, which alternates yearly with a section on Arctic river discharge, as the scales of regular observation for both of these climate components are best suited for reporting every two years.)

b. Surface air temperature—T. J. Ballinger, J. E. Overland, R. Thoman, M. Wang, M. A. Webster, L. N. Boisvert, C. L. Parker, U. S. Bhatt, B. Brettschneider, E. Hanna, I. Hanssen-Bauer, S.-J. Kim, and J. E. Walsh

1) ARCTIC TERRESTRIAL SURFACE AIR TEMPERATURES: A HISTORICAL REVIEW

Increased air temperatures are a fundamental indicator of Arctic change (Box et al. 2019). Warming has been linked with changing frequency, intensity, and duration of high-latitude atmospheric extremes that impact snow and ice melt (Walsh et al. 2020). The 2021 annual surface air temperature (SAT) anomaly for terrestrial areas within 60°–90°N was 0.4°C above the 1991–2020 mean, marking the eighth consecutive year that Arctic land temperatures have exceeded the 30-year

average (Fig. 5.1). With respect to the 1900–2021 historical period, 2021 ranked as the 13th-warmest year on record but coolest since 2013. The Arctic experienced its fourth-warmest spring (April–June), which contributed substantially to the annual temperature anomaly. Within the Arctic, both the European (0°–90°E) and Asian (90°–180°E) sectors' temperatures exceeded the 90th percentile during spring (Ballinger et al. 2021). Air temperatures throughout other seasons were above normal, but not extreme for most Arctic areas. The Greenland-Iceland region (60°W–0°) was the exception, with warming above the 90th percentile during winter (January–March), summer (July–September), and autumn (October–December; Ballinger et al. 2021). As discussed below in subsection 2, much of this region's seasonal warming was confined to marine and coastal areas. Despite the warm pattern, the region's air temperatures remained broadly subfreezing in winter and autumn, coincident with ~50% less Greenland Ice Sheet mass loss in 2020/21 than the 2000–21 mean (section 5e). The year 2021 was marked by near-normal temperatures over the central Arctic with large deviations over the subarctic continents in response to jet stream variability. In the following section, we characterize seasonal air temperature anomalies in further detail.

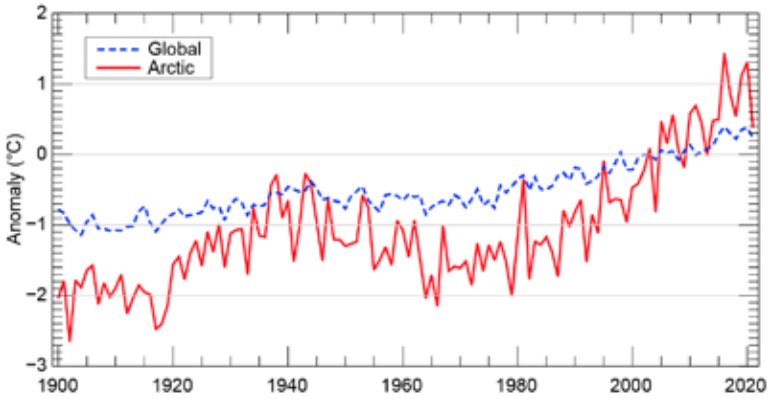

Fig. 5.1. Annual mean SAT anomalies (°C) for weather stations located on Arctic lands, 60°–90°N (red line), and globally (blue line) from 1900 to 2021. The temperature anomalies are shown with respect to their 1991–2020 mean. It is worth noting that the 1991–2020 mean was > 0.6°C higher than the 1981–2010 mean. (Source: CRUTEM5 SAT data are obtained from the Climate Research Unit [University of East Anglia] and Met Office.)

2) SUMMARY OF 2021 SEASONAL AIR TEMPERATURES

Air temperature anomalies, relative to the 1991–2020 mean, are discussed for 2021 by season and presented in Fig. 5.2. Seasonal temperature anomalies at the 925-hPa level are described to emphasize large-scale spatial patterns rather than local-scale variability.

In winter 2021, a distinct temperature gradient was found between the higher-than-average Atlantic side of the Arctic Ocean, including areas stretching northward from the eastern Canadian Arctic and Hudson Bay, and lower-than-average Eurasia and northwest North America. Air temperatures around the central Arctic Ocean extending south into northern Greenland and Svalbard were 2–4°C higher than normal. Western Greenland and adjacent Baffin Bay, Davis Strait, and Labrador Sea saw temperature anomalies of +2° to +3°C that increased westward to a +5° to +6°C maximum over northern Quebec and Newfoundland. Cold anomalies extended southward from Arctic coastal zones to northern Russia, Chukotka, Alaska, and the Yukon and Northwest Territories (Fig. 5.2a). Two upper-level low geopotential height centers over north-central Siberia and the Canadian Archipelago were concurrent with this swath of below-normal temperatures (Fig. 5.3a).

Spring was characterized by above-normal temperatures extending from the Arctic Ocean margins southward into adjacent lands (Fig. 5.2b), associated with a low over the central Arctic and primarily zonal (west-to-east) flow over these areas (Fig. 5.3b). For example, air temperatures over northern Eurasian coastal areas and adjacent Arctic waters were 2–4°C higher than the 1991–2020 average. Baffin Bay and the Labrador Sea were also higher than normal. The Eurasian spring temperature anomalies were linked to low regional snow cover (section 5g) and early sea ice melt in the Laptev Sea (section 5d). Several Arctic weather stations reported record air temperatures during spring 2021, including 39.9°C observed at Fort Smith, Northwest Territories, Canada, on 30 June, which set the maximum surface temperature record in the province (Henson and Masters 2021).

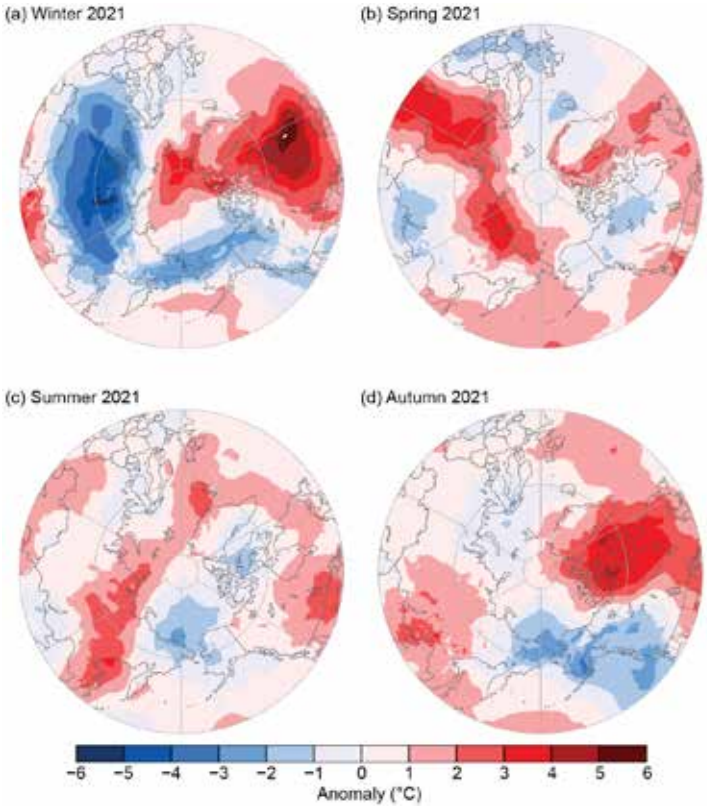

Fig. 5.2. Near-surface (925 hPa) seasonal air temperature anomalies (°C) in 2021 for (a) winter, (b) spring, (c) summer, and (d) autumn. Anomalies are shown relative to their 1991–2020 means. (Source: ERA5 reanalysis air temperature data are obtained from the Copernicus Climate Change Service.)

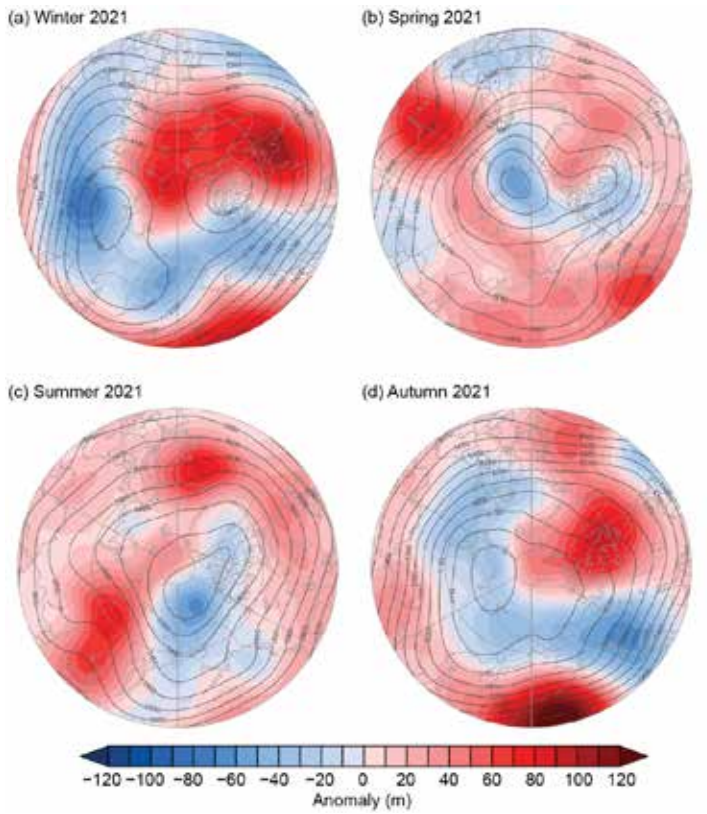

Fig. 5.3. Seasonal atmospheric circulation patterns in 2021 for (a) winter, (b) spring, (c) summer, and (d) autumn. The contours (shading) represent 500-hPa geopotential height values (anomalies relative to the 1991–2020 seasonal means, m). Upper-level winds tend to circulate clockwise around higher geopotential height values. (Source: ERA5 reanalysis geopotential height data are obtained from the Copernicus Climate Change Service.)

Notably warm summer air temperature anomalies were found over northern Iceland and the southern Greenland Sea (+2° to +3°C) and extended from the northern Sea of Okhotsk (+2° to +4°C) into northeastern Siberia (Fig. 5.2c). The corresponding 500-hPa flow was similar to spring, though the low center moved into the Pacific Arctic sector (Fig. 5.3c). Following on from recent warm, fire-prone summers, above-normal Siberian air temperatures coincided with an extreme fire season during 2021 (York et al. 2020; Ponomarev et al. 2022). In contrast, 1–2°C below-normal temperatures occurred over portions of the Beaufort, Chukchi, and East Siberian Seas.

Exceptional summer warmth over the Greenland-Iceland region was primarily found over marine, coastal, and low-elevation areas of the Greenland Ice Sheet (Fig. 5.2c). These seasonal anomalies were punctuated by anomalous air temperature events that occurred in late July and mid-August, producing widespread Greenland Ice Sheet melt. The latter event coincided with remarkably late and extensive ice sheet melt and the first rain event at Summit Station, Greenland's highest elevation area, since it was established in 1989 (section 5e).

Autumn air temperature anomalies of 2–4°C above average were found from western Greenland to eastern Canada (Fig. 5.2d), concurrent with a jet stream trough over Hudson Bay that funneled warm air into these areas from lower latitudes (Fig. 5.3d). Upstream regions of the Pacific Arctic, including Chukotka, Alaska, and south-central Yukon and Northwest Territories, experienced temperatures 1–3°C below normal due to a relatively zonal jet stream that prevented incursions of warm air masses (Fig. 5.3d).

3) ARCTIC PRECIPITATION IN 2021: A RESPONSE TO WARMING

Increased precipitation and greater probabilities of rain at the expense of snow are impacts of a warming Arctic (Łupikasza and Cielecka-Nowak 2020; McCrystall et al. 2021). Using ERA5, these characteristics manifested in 2021 as modestly higher total precipitation but, on average, consisted of considerably less snowfall relative to the 1991–2020 climatology (Fig. 5.4). Winter, summer, and autumn were characterized by anomalously low snowfall (blue shading) and high rainfall (red shading; Figs. 5.4e,g,h,i,k,l), while spring had markedly more snowfall (Fig. 5.4f) and total precipitation (Fig. 5.4b). Canada broke a new spring record, receiving 19% more total precipitation than normal. Alaska and the Pacific Arctic sector (60°–90°N, 150°E–120°W) had the second-highest spring snowfall amounts since 1979, totaling 19 mm and 14 mm water equivalent, respectively. Anomalously low precipitation fell on Russia during spring, but of that precipitation more than 90% fell as rain rather than snow (Figs. 5.4b,f,j), aligned with persistent warm air temperatures (Fig. 5.2b).

Summer warmth during 2021 (Fig. 5.2c) also contributed to diminished Arctic snowfall (Fig. 5.4g). Overall, there was 7% less snowfall than average with the largest anomalies occurring in Alaska (–16 mm) and the Pacific Arctic sector (–11 mm). Similarly, Greenland saw more precipitation (+23 mm) and more rainfall (+22 mm) than any year during 1991–2020, including the Summit Station rain event (section 5e). During autumn, snowfall amounts were 3% below average for the Arctic with the Alaska and Pacific Arctic sectors receiving the least snowfall (23–24% below normal). Alaska received 13% more rainfall than the 1991–2020 autumn average, tied to a late December rain-on-snow event.

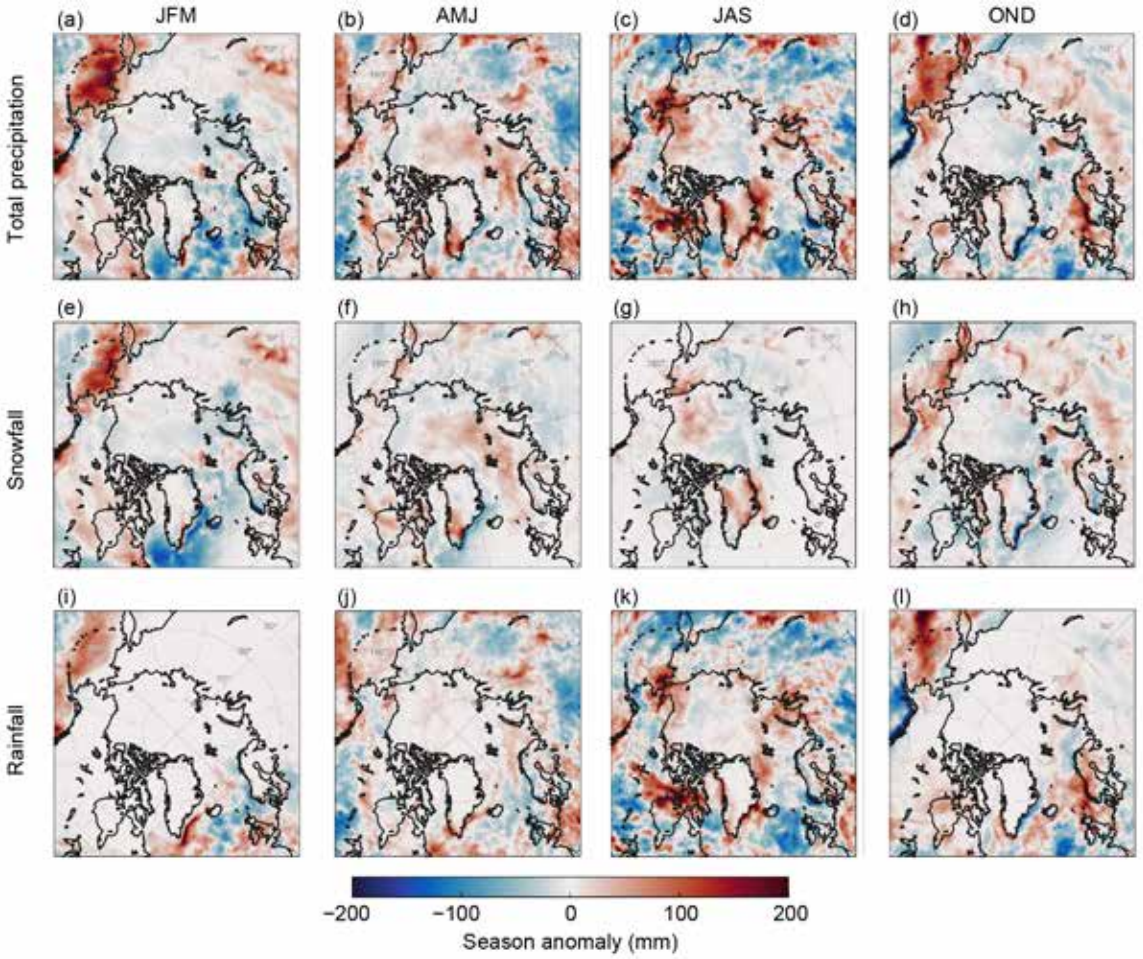

Fig. 5.4. The 2021 season anomalies (mm) in (a–d) total precipitation, (e–h) snowfall, and (i–l) rainfall for the winter (JFM, panels a,e,i), spring (AMJ, panels b,f,j), summer (JAS, panels c,g,k), and autumn (OND, panels d,h,l) relative to the 1991–2020 climatology. Rainfall is inferred from the difference between total precipitation and snowfall. (Source: ERA5 total precipitation and snowfall data are obtained from the Copernicus Climate Change Service.)

c. Sea surface temperature—M.-L. Timmermans and Z. Labe

Arctic Ocean sea surface temperatures (SSTs) in the summer (June–August) are driven by the amount of incoming solar radiation absorbed by the sea surface and by the flow of warm waters into the Arctic from the North Atlantic and North Pacific Oceans. Solar warming of the Arctic Ocean surface is influenced by the distribution of sea ice (with greater warming occurring in ice-free regions), cloud cover, and upper-ocean stratification. Discharge of relatively warm Arctic river waters can provide an additional source of heat to the surface of marginal seas.

Arctic SST is an essential indicator of the role of the ice–albedo feedback mechanism in any given summer sea ice melt season. As the area of sea ice cover decreases, more incoming solar radiation is absorbed by the ocean and, in turn, the warmer ocean melts more sea ice. In addition, higher SSTs are associated with delayed autumn freeze-up and increased ocean heat storage throughout the year. In another positive (amplifying) feedback related to global warming, higher SSTs can be associated with reduced ocean uptake of carbon dioxide from the atmosphere. Marine ecosystems are also influenced by SSTs, which affect the timing and development of production cycles, as well as available habitat.

The SST data presented here are a blend of in situ and satellite measurements from August 1982 to August 2021, taken from the monthly mean NOAA Optimum Interpolation (OI) SST Version 2 product (OISSTv2; Reynolds et al. 2002, 2007). In the Arctic Ocean overall, the OISSTv2 product has been found to exhibit a cold bias (i.e., underestimate SST) of up to 0.5°C compared to in situ measurements (Stroh et al. 2015). The OISSTv2 product uses a simplified linear relationship with

sea ice concentration to infer SST under sea ice (Reynolds et al. 2007), which means SSTs may be too low by up to 0.2°C where there is sea ice cover. The potential cool bias under sea ice can be reflected in trends and variability in the vicinity of the ice edge. We focus on August mean SSTs, which provide the most appropriate representation of Arctic Ocean summer SSTs because they are not affected by the cooling and subsequent sea ice growth that typically takes place in the latter half of September. Note that the SST reference period is August 1982–2010 because the satellite SST record begins in December 1981.

August 2021 mean SSTs ranged from 6° to 10°C in the southeast Chukchi and Barents Seas to around 0° to 3°C in the East Siberian, Kara and Laptev Seas, Baffin Bay, and in the ice-free waters east of Greenland (Fig. 5.5a). August 2021 mean SSTs were notably high (around 1–3.5°C higher than the 1982–2010 August mean) in the Kara and Laptev Seas (Fig. 5.5b). This is consistent with early-season sea ice retreat in these regions (section 5d), and anomalously warm spring (April–June) 2021 air temperatures over northern Eurasia (section 5b). SSTs in the waters east of Greenland were also higher than the 1982–2010 August mean by around 1–3°C. It is notable that in the same region, summer 2021 surface air temperatures were about 2–5°C higher than the climatological mean (section 5b).

The northern Barents Sea, Baffin Bay, and the Chukchi Sea experienced anomalously cool SSTs in August 2021, around 0.5° to 1°C below the 1982–2010 mean (Fig. 5.5b). Surface air temperatures in summer (June–August) were below average in the Beaufort and Chukchi Sea regions, and conditions were cloudy, limiting solar fluxes to the surface ocean. Lower SSTs are also consistent with greater sea ice extents (closer to normal) in the Chukchi and Beaufort Sea regions compared to recent past years, related to wind-driven transport of thick multiyear ice into the region in early 2021 (section 5d).

There is significant variability from year to year in the particular regions that exhibit anomalously low or high SSTs. The strong interannual variability in spatial patterns are evident in the differences between August 2021 and August 2020 SSTs (Fig. 5.5c). August 2021 SSTs were around 0.5°C (and up to 2°C) cooler than

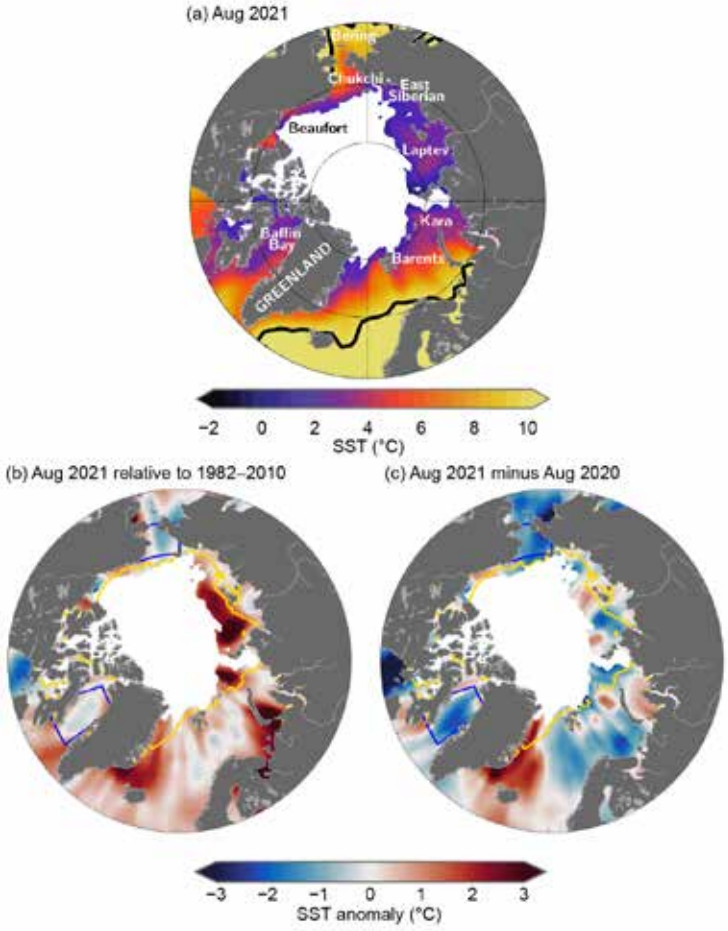

Fig. 5.5. (a) Mean sea surface temperature (SST; °C) in Aug 2021. Black contours indicate the 10°C SST isotherm. (b) SST anomalies (°C) in Aug 2021 relative to the Aug 1982–2010 mean. (c) Difference between Aug 2021 SSTs and Aug 2020 SSTs (negative values indicate where 2021 was cooler). White shading in all panels is the Aug 2021 mean sea ice extent. The yellow lines in (b) and (c) indicate the median ice edge for Aug 1982–2010. The two regions marked by blue boxes in (b) and (c) indicate regions of Baffin Bay and the Chukchi Sea and relate to data presented in Figs. 5.6c,d. (Data sources: SST data are the NOAA OISSTv2 provided by the NOAA/OAR/ESRL PSD, Boulder, Colorado, https://psl.noaa.gov/data/gridded/data.noaa.oisst.v2.html [accessed 8 Feb 2022; Reynolds et al. 2007]; sea ice concentration data are the NOAA/NSIDC Climate Data Record of Passive Microwave Sea Ice Concentration, Version 4 (https://nsidc.org/data/g02202) and Near-Real-Time NOAA/NSIDC Climate Data Record of Passive Microwave Sea Ice Concentration, Version 2 (https://nsidc.org/data/g10016) [Peng et al. 2013; Meier et al. 2021a,b], where a threshold of 15% concentration is used to calculate extent.)

in August 2020 over a significant portion of the ice-free regions, with some exceptions, including (up to 3°C) higher SSTs off of east Greenland (Fig. 5.5c).

Mean August SST warming trends from 1982 to 2021 persist over much of the Arctic Ocean, with statistically significant (at the 95% confidence interval) linear warming trends shown in Fig. 5.6a. Mean August SSTs for the entire Arctic (the Arctic Ocean and marginal seas north of 67°N) exhibit a linear warming trend of +0.03 ± 0.01°C yr^{-1} (Fig. 5.6b). Even while anomalously low SSTs in Baffin Bay and the Chukchi Sea were prominent in the August 2021 SST field (Figs. 5.5b, 5.6c,d), SSTs in both of these regions show long-term warming. Baffin Bay August SSTs exhibit a linear warming trend over 1982–2021 of +0.05 ± 0.01°C yr^{-1} (Fig. 5.6c). Similarly, Chukchi Sea August mean SSTs are warming with a linear trend of +0.06 ± 0.03°C yr^{-1} (Fig. 5.6d). The cooling trend (~−0.06°C yr^{-1}) in mean August SSTs in the north-central Barents Sea region remains a notable exception (Timmermans et al. 2020), although the cooling trend is not observed for most other months, nor for other parts of the Barents Sea (Lind et al. 2018; Smedsrud et al. 2022). Further, in this region Barents Sea waters contact cooler, fresher Arctic waters, and shifts in this boundary complicate interpretation of trends (see Barton et al. 2018).

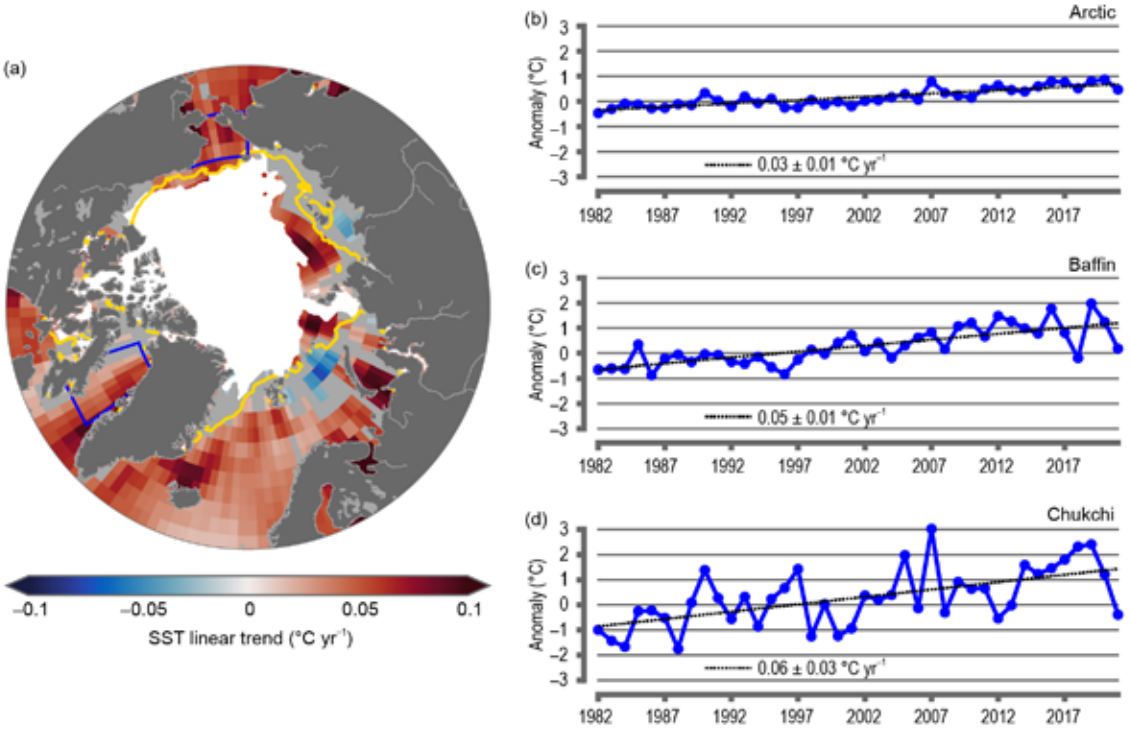

Fig. 5.6. (a) Linear SST trend (°C yr^{-1}) for Aug of each year from 1982 to 2021. The trend is only shown for values that are statistically significant at the 95% confidence interval; the region is shaded gray otherwise. White shading is the Aug 2021 mean sea ice extent, and the yellow line indicates the median ice edge for Aug 1982–2010. (b,c,d) Area-averaged SST anomalies (°C) for Aug of each year (1982–2021) relative to the 1982–2010 Aug mean for (b) the entire Arctic Ocean north of 67°N, (c) Baffin Bay, and (d) Chukchi Sea regions shown by blue boxes in (a). The dotted lines show the linear SST anomaly trends over the period shown and trends in °C yr^{-1} (with 95% confidence intervals) are indicated on the plots. (Data sources: see Fig. 5.5 caption.) (Source: Data are from NSIDC and University of Colorado [Tschudi et al. 2019, 2020]).

d. Sea ice—W. N. Meier, D. Perovich, S. Farrell, C. Haas, S. Hendricks, A. Petty, M. Webster, D. Divine, S. Gerland, L. Kaleschke, R. Ricker, A. Steer, X. Tian-Kunze, M. Tschudi, and K. Wood

Arctic sea ice is the frozen interface between the ocean and atmosphere in the North, limiting ocean–atmosphere exchanges of energy and moisture and playing a critical role in Arctic ecosystems and Earth's climate. Sea ice also plays a key role in Arctic human activities, including

Indigenous hunting and transportation, marine navigation, and national security responsibilities. Overall, 2021 continued to demonstrate the profound changes underway in the Arctic sea ice system.

1) SEA ICE EXTENT

Arctic sea ice began 2021 recovering from record or near-record low coverage and a notably late freeze-up in autumn 2020. By January 2021, sea ice extent (defined as the total area covered by at least 15% ice concentration) was lower than the 1981–2010 average in the Bering and Barents Seas, but near-average elsewhere. Extent values are from the NSIDC Sea Ice Index (Fetterer et al. 2017), one of several extent products (Lavergne et al. 2019; Ivanova et al. 2014) derived from satellite-borne passive microwave sensors operating since 1979. Persistent high pressure in the Siberian Arctic sector during January–February resulted in divergence of ice from the Siberian coast and strong advection of thicker, multiyear ice into the Beaufort and Chukchi Seas.

By March, the month with the greatest ice cover, the total sea ice extent of 14.64 $\times 10^6$ km^2 was 0.79 $\times 10^6$ km^2 (5.1%) lower than the 1981–2010 average and the ninth-lowest March extent in the 43-year record. The low sea ice extent in March 2021 was less extreme than during 2015–19, but continued the statistically significant downward trend of –2.6 % per decade over the 1979–2021 record (Fig. 5.7a). On a regional basis, March 2021 was characterized by below-average extent in the Bering Sea, Baffin Bay, and the Gulf of St. Lawrence and near-normal extent elsewhere (Fig. 5.7b).

After March, the seasonal retreat of ice began. The multiyear ice in the Beaufort and Chukchi Seas that developed earlier in winter delayed the retreat of sea ice on the North American side of the Arctic. On the Siberian side, strong pressure gradients facilitated early melt onset and local sea ice retreat in spring, leading to a record low extent in the Laptev Sea during May and June.

During summer 2021, the atmospheric circulation (marked by general low pressure over the Arctic Ocean; section 5b), along with the thicker ice in the Beaufort and Chukchi Seas, slowed the decline in ice extent. The summer circulation limited sea ice export through Fram Strait, resulting in the unusual occurrence of a nearly ice-free East Greenland Sea during much of the summer.

Sea ice extent in September 2021 was characterized by below-average coverage in the Siberian and East Greenland Seas

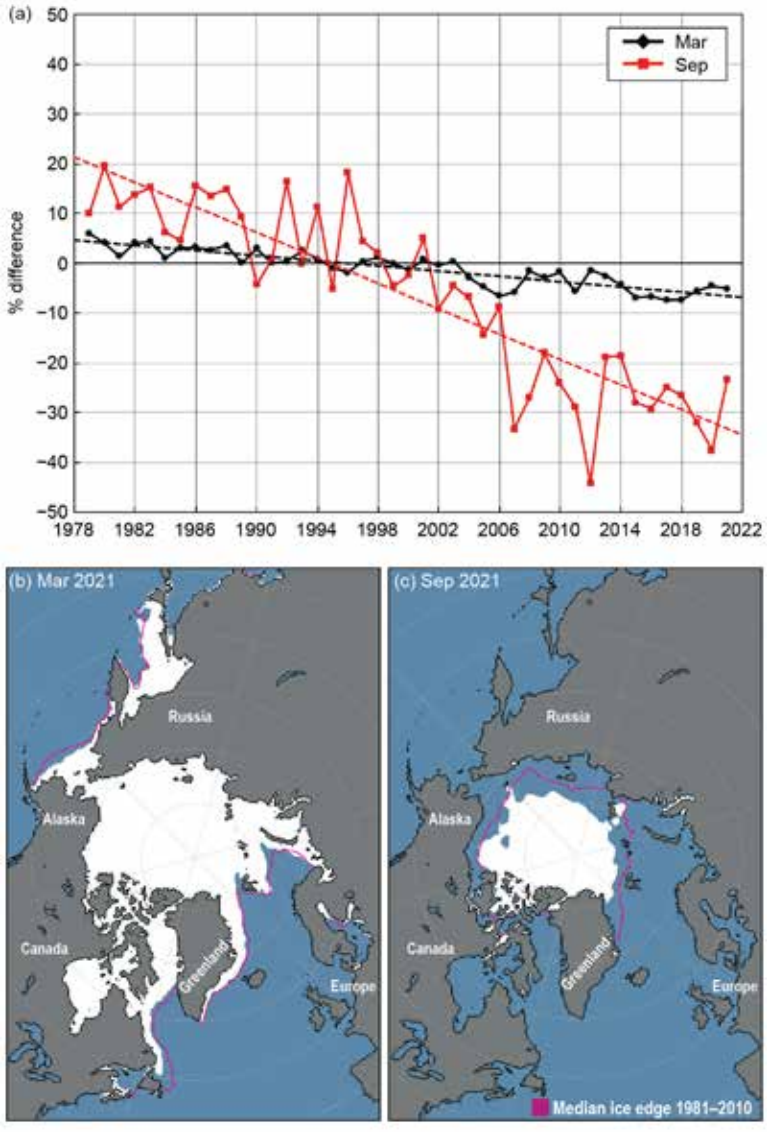

Fig. 5.7. (a) Monthly sea ice extent anomalies (solid lines) and linear trend lines (dashed lines) for Mar (black) and Sep (red) from 1979 to 2021. The anomalies are relative to the 1981–2010 average for each month. (b) Mar 2021 and (c) Sep 2021 monthly average sea ice extent; the median extent for 1981–2010 is shown by the magenta contour.

and closer-to-normal coverage in the Beaufort and Chukchi Seas (Fig. 5.7c). Arctic-wide, the slower summer decline resulted in a September 2021 total sea ice extent of 4.92×10^6 km^2, which was 1.49×10^6 km^2 (23.2%) lower than the 1981–2010 average and the 12th-lowest September extent on record. The September trend from 1979 through 2021 is –12.7% decade^{-1} and like all other months, is statistically significant. The 15 lowest September extents in the satellite record have all occurred in the last 15 years (2007–21).

2) SEA ICE AGE, THICKNESS, AND VOLUME

Sea ice age is a rough proxy for thickness as multiyear ice (ice that survives at least one summer melt season) grows thicker over successive winters. Sea ice age is presented here (Fig. 5.8) for the period 1985–2021, based on Tschudi et al. (2019a,b). One week before the 2021 annual minimum extent, when the age values of the remaining sea ice are incremented by one year, the amount of multiyear ice remaining in the Arctic was the second lowest on record (above only 2012). The September multiyear ice extent declined by 70.7%, from 4.40×10^6 km^2 in 1985 to 1.29×10^6 km^2 in 2021 (Fig. 5.8). Over the same period, the oldest ice (> 4 years old) declined by 94.1%, from 2.36×10^6 km^2 to 0.14×10^6 km^2. In the 37 years since ice-age records began in 1985, the Arctic has changed from a region dominated by multiyear sea ice to one where first-year sea ice prevails. A younger ice cover implies a thinner, less voluminous ice pack and one that is more fragile and vulnerable.

Sea ice drifts with wind and ocean currents, while growing and melting thermodynamically. Ice convergence leads to dynamic thickening, while ice divergence creates leads and, in winter, new ice. Sea ice thickness is an important indicator of overall ice conditions because it provides a record of the cumulative effect of dynamic and thermodynamic processes. The ESA CryoSat-2/SMOS satellites have provided a record of seasonal (October to April) ice thickness and volume (Ricker et al. 2017) since the 2010/11 winter. Since 2018, the NASA ICESat-2 satellite has also provided thickness estimates (Petty et al. 2020, 2021). Some differences between these two products are seen for April 2021 (the month of maximum annual thickness), with ICESat-2 indicating thicker ice along the Canadian Archipelago and Alaskan coast (Fig. 5.9a), while CryoSat-2/SMOS shows thicker ice in the eastern Arctic (Fig. 5.9b). However, the overall spatial patterns are similar. Compared to the 2011–20 April average, the 2021 CryoSat-2/SMOS product shows thinner ice along the northern Canadian Archipelago and Greenland coasts, the East Greenland and Barents Seas, and somewhat thicker-than-average ice in the Laptev Sea and along the Alaskan coast (Fig. 5.9c). On average, the 2020/21 winter sea ice was the thinnest in the CryoSat-2/SMOS record.

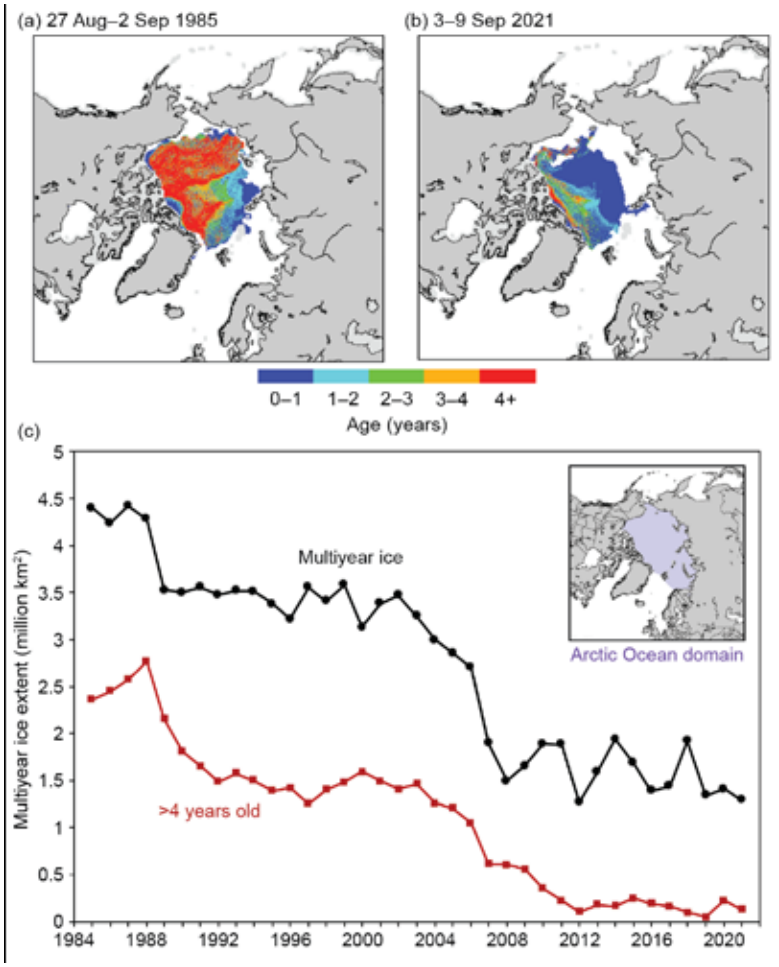

Fig. 5.8. Sea ice age coverage map for the week before minimum total extent (when age values are incremented to one year older) in (a) 1985 and (b) 2021; (c) extent of multiyear ice (black) and ice > 4 years old (red) within the Arctic Ocean (inset) for the week of the minimum total extent.

Sea ice thickness is integrated with ice concentration to provide winter volume estimates for 2010–21. The seasonal timeseries (Fig. 5.10) indicates below-average ice volume throughout the 2020/21 winter, with record low conditions spanning October to mid-November. Volume growth typically slows by early March as spring warming begins. In 2021, the volume experienced near-zero growth for much of March and decreased slightly thereafter. Ice volume in April 2021 was the lowest in the 2010–21 April record. While the rate of decline in September sea ice extent over the 2010–21 period has slowed compared to previous decades, Arctic sea ice volume continues to rapidly shrink.

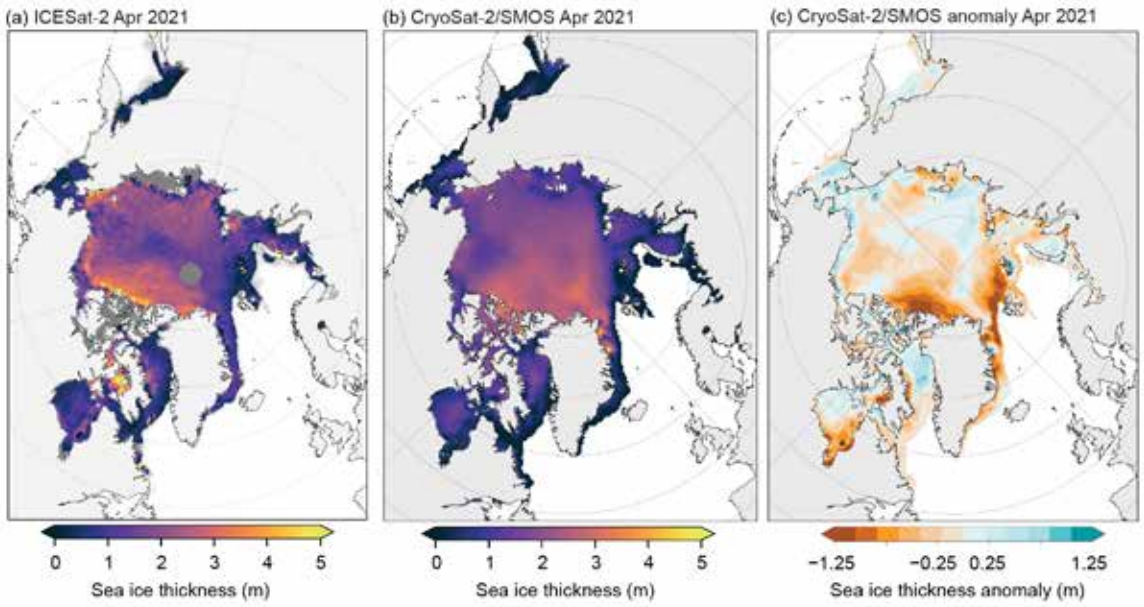

Fig. 5.9. (a) ICESat-2 (dark gray areas have no data) and (b) CryoSat-2/SMOS sea ice thickness (m) for Apr 2021; (c) CryoSat-2/SMOS thickness anomaly (m) for Apr 2021 (relative to the 2010–20 average). Note that ICESat-2 thickness estimates outside the Arctic Ocean domain (see the Fig. 5.8c inset) are not as reliable due to uncertainties in snow cover.

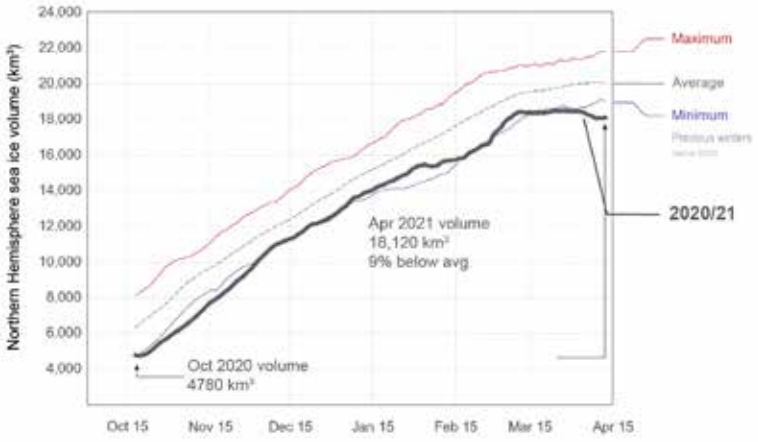

Fig. 5.10. CryoSat-2/SMOS Northern Hemisphere sea ice volume from 15 Oct to 15 Apr for the 2020/21 season. The maximum (red line), minimum (blue line), and average (dashed gray line) volume over the 11-year (2010–20) record are also provided.

SIDEBAR 5.1: IN TRANSITION: MARITIME POLLUTION AND THE BERING STRAIT REGION—G. SHEFFIELD AND K.M. STAFFORD

The Bering Strait region is a narrow transboundary waterway between eastern Chukotka (Russia) and western Alaska (United States) and is the only marine corridor from the Pacific to the Arctic Ocean. The maritime ecosystem of the northern Bering Sea/Bering Strait region is distinct from the southern Bering Sea, separated by a thermal barrier created and maintained by the once stable seasonal sea ice. The remote coastal communities of this region are ethnically diverse and reliant on the non-commercial acquisition of marine resources for their nutritional, cultural, and economic well-being (Fig. SB5.1).

The ongoing reduction in the quality, extent, and duration of sea ice in the Bering Strait region is rapidly transforming the environment and reorganizing marine ecosystems (Stevenson and Lauth 2019; Eisner et al. 2020; Thoman et al. 2020). More economic opportunities are resulting in an increase in the size, duration, and diversity of industrial ship traffic transiting and/or utilizing the region (Humpert 2021; Smith 2021; USCMTS 2019). Unprecedented numbers of multi-national ships are chasing southern Bering Sea fisheries that are advancing northwards and/or utilizing the Strait as a transportation corridor. Impacts of increased industrial ship traffic include increases and/or changes in marine debris and ambient noise.

Fig. SB5.1. Seal and walrus meat, harvested for subsistence purposes, drying on a wooden rack for preservation and later consumption by community members on Little Diomede Island, Alaska. Big Diomede Island, Chukotka, Russian Federation is in the background. Photo credit: G. Sheffield.

Marine Debris

During summer 2020, the Bering Strait region of Alaska experienced a novel foreign marine debris event. Through mid-November, individuals from 14 Alaskan coastal communities discovered and documented over 350 individual items ashore, most with Russian, Korean, and/or other Asian lettering or branding (Sheffield et al. 2021). This number was considered a minimum, with qualitative reports of mostly uncounted debris extending "for miles." Reporting communities included locations in Norton Sound, Bering Strait, and the Chukchi Sea region. Additional reports of debris ashore were received from the U.S. Coast Guard.

The novelty of this event was not due to foreign debris of commercial fishing equipment, but rather the widespread everyday garbage, including plastics, food items, and hazardous materials (Fig. SB5.2). Most plastic items were un-weathered, indicating they had entered the water recently. April 2020 was the most recent date of manufacturing noted on any item. Hazardous materials included cans and other containers that had and/or still contained insecticides, toilet cleaners, drain clog remover, lubricating oils, butane gas, and spray paints.

Regional residents, tribal leadership, and coastal communities provided awareness of the event, documented, reported, conducted clean-up activities, and investigated the source of debris on a voluntary basis using personal resources, little to no training, and limited response capacity (Sheffield et al. 2021). The foreign debris event negatively affected regional peoples' sense of security regarding the health of the transitioning northern Bering Sea marine ecosystem (Stevenson and Lauth 2019; Eisner et al. 2020; Spies et al. 2020) and the level of future risks and impacts from the forecasted and observed increase of industrial ship traffic in the Bering Strait region (USCMTS 2019; Humpert 2021).

Without regular and relevant collaborative transboundary communications between the United States and the Russian Federation and enforcement of existing international marine pollution rules (IMO 2021), the Bering Strait region can expect similar or higher levels of marine garbage in the future as industrial ship traffic increases.

Ambient Noise

In the ocean, the combination of naturally occurring sounds from wind, waves, and marine animals contribute to ambient noise. Unique to the polar regions are the sounds contributed by sea ice and icebergs, which generate noise via ice

Fig. SB5.2. Items from 2020 foreign marine debris event: (a) plastics scattered along the shoreline; photo credit: L. Apatiki, (b) shampoo bottle; photo credit: T. Pelowook, (c) miscellaneous aerosol cans of butane, paint, and lubricating oil, foods, and bottles of bathroom cleaners, water bottles, etc; photo credit: G. Sheffield, (d) 1L carton of milk; photo credit: A. Ahmasuk, (e) deck boot; photo credit: G. Sheffield, (f) longline anchor buoy from a Vladivostok-based fishing company with the Pacific cod permit attached; photo credit: R. Tokeinna.

formation and deformation, pressure ridging, and cracking, but also decrease noise due to the lack of wind-driven waves in ice-covered waters. The sounds from storms and from novel marine animals that have moved into the ice-free regions of the Arctic are changing underwater ambient noise profiles, but are also giving us insight into natural atmospheric and biologic changes that are occurring. While marine debris and oil spills provide visual evidence of pollution, underwater sound can also be considered a form of pollution. 'Sound' becomes 'noise' when it may negatively impact the health or behavior of marine animals and is driven by increased shipping, including cargo and fishing vessels (Rolland et al. 2013). Underwater noise is created from the rotation of ships' propellers; this noise is relatively continuous and low-frequency (under 1000 Hz). Noise is also created by icebreakers breaking through sea ice. Ship noise overlaps in frequency with the sounds produced and received by Arctic marine mammals. Signals in the same frequency band are more likely to interfere with animals' ability to hear and respond to important sounds (Blackwell and Thode 2021; Tervo et al. 2021). Increases in overall noise levels increase stress hormones in individual animals and may have long-term impacts on their ability to navigate, communicate, feed, and reproduce.

The most persistent anthropogenic noise source in the Bering Strait region is industrial ship traffic, most of which sails the Northern Sea Route (NSR) across waters north of Russia from the Pacific to the Atlantic (CHNL 2022). Most large ships traverse the NSR during July to October when sea ice coverage is minimal. However, in January 2021, at least four liquid natural gas tankers sailed the NSR without icebreaker support. Because large volumes of industrial maritime traffic in the Arctic are a relatively new phenomenon, Arctic marine wildlife may have a lower tolerance for, and react more strongly to, noise from these ships (PAME 2019).

Summary

With continued sea ice reduction and ecosystem-wide shifts expected, increased industrial ship traffic in/among the Bering Strait region will continue to elevate existing regional food security, public health, wildlife health, and conservation concerns. Potential risks to marine wildlife from marine debris include entanglements, exposure to hazardous chemicals, and ingestion of plastics and/or hazardous materials and chemicals. Potential risks to marine wildlife, from increasing ambient noise, include deflection from important feeding areas, changes in timing of movements, and a reduced ability to communicate opportunities or risks. Without enforcement of existing international pollution laws and/or mitigation efforts regarding emerging impacts from multi-national industrial ship traffic, the Arctic and the Bering Strait region can expect increasing amounts and types of marine debris and noise pollution.

For more details on the 2020 marine debris event in Bering Strait the changing Arctic marine soundscape, please see the 2021 Arctic Report Card (Sheffield et al. 2021; Stafford 2021).

:

e. Greenland ice sheet—T. A. Moon, K. D. Mankoff, R. S. Fausto, X. Fettweis, M. Tedesco, A. Wehrlé, B. D. Loomis, T. L. Mote, C. D. Jensen, N. Korsgaard, J. E. Box, J. Cappelen, and Ø. A. Winton

The Greenland Ice Sheet has lost mass every year since 1998, with negative impacts of ice loss experienced globally. The ice sheet contains enough ice to generate ~7.4 m of eustatic sea level rise (rise caused by ocean mass changes only; Morlighem et al. 2017). With multiple methods available for measuring Greenland Ice Sheet mass balance, we compare 1 September 2020 through 31 August 2021 mass change values derived from satellite gravimetry using Gravity Recovery and Climate Experiment Follow On (GRACE-FO) measurements (–125 ± 35 Gt) and an input-output (I/O) method (–165 ± 89 Gt; see Fig. 5.11 for details on methods and references). GRACE-FO values include Greenland glaciers and ice caps not directly connected to the main ice sheet, while I/O values do not, introducing a likely bias of ~15–20% (Bolch et al. 2013; though acknowledging potentially higher bias values) and lowering the agreement between methods. The change in GRACE-FO mass balance reported here as compared to Moon et al. (2021) is due to the availability of additional 2021 data to improve the calculation. Across the two methods, the estimated range in mass loss represents ~0.3–0.5 mm of global mean sea level rise in 2020/21 (excluding ongoing thermal expansion [IPCC 2021]). Using the satellite gravimetry time series, the 2020/21 ice loss was ~138 Gt less than the 2002–21 average of –263 ± 15 Gt yr^{-1}.

This year of moderate twenty-first century ice loss includes substantial variations in ice sheet surface conditions, particularly over the summer melt season. The ice sheet balance year (1 September–31 August) captures the annual cycle of snow accumulation (gain) and ice/snow ablation (loss), using seasonal breaks at September–November (autumn), December–February (winter), March–May (spring), and June–August (summer). Except for an above-average melt event on 27 April, the ice sheet daily melt extent as estimated by satellites remained low until 26 May and through mid-summer remained mostly within the 1981–2010 10th to 90th percentiles (Fig. 5.12).

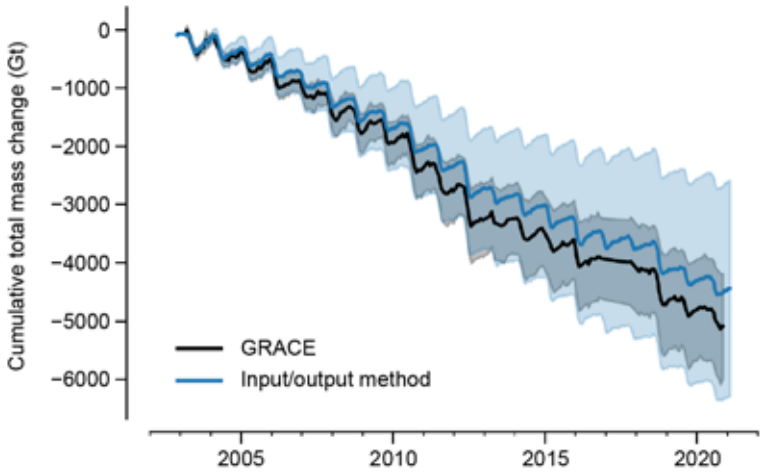

Fig. 5.11. Comparison of results using GRACE and GRACE-FO (black; includes peripheral glaciers and ice caps) and the input/output method (I/O; blue; does not include peripheral glaciers and ice caps) for total mass balance. Shading for I/O method represents the systematic or bias (not random) uncertainty (e.g., uncertain ice thickness), and shading for GRACE also includes monthly noise estimates. These uncertainties accumulate. GRACE (2002–17) and GRACE–FO (2018–present) satellite data and technical notes are hosted at https://podaac-tools.jpl.nasa.gov/drive/files/allData. GRACE and GRACE-FO data are corrected for glacial isostatic adjustment (Peltier et al. 2018). The I/O method is the mean of MAR, RACMO, and HIRHAM/HARMONIE regional climate models minus discharge from Mankoff et al. (2020, data: https://doi.org/10.22008/promice/data/ice_discharge/d/v02).

In situ observations are provided via 15 mostly terrestrial Danish Meteorological Institute (DMI) weather stations and eight on-ice automatic weather station transects from the Programme for Monitoring of the Greenland Ice Sheet (PROMICE) at the Geological Survey of Greenland and Denmark (GEUS; Fausto et al. 2021). PROMICE stations recorded surface air temperatures within ± 1 std. dev. of monthly means for June and July. Late July and August, however, included three extreme melt episodes (Fig. 5.12b). The first, on 19 July, had melt across 702,000 km^2 (~43%) of the ice sheet surface. A second melt episode on 28 July extended across 54% of the ice sheet surface, and a third melt episode concentrated on 14 August had extended across 53% of the ice sheet surface and reached the highest ice sheet elevations at the National Science Foundation's (NSF) Summit Station (3216 m a.s.l.).

The mid-summer rapid rise in ice loss is reflected in ice ablation measurements taken at some PROMICE stations

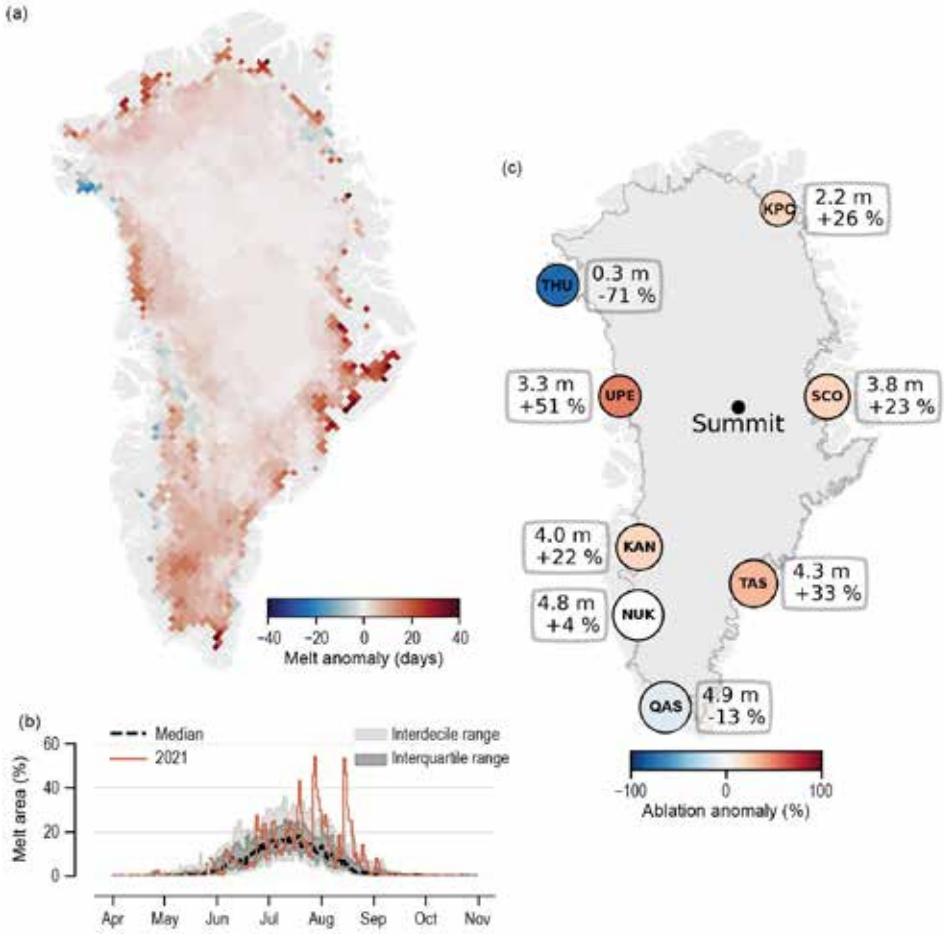

Fig. 5.12. (a) 2021 melt anomaly (in number of melting days) with respect to a 1981–2010 reference period. (b) Surface melt extent as a percentage of the ice sheet area during 2021 (solid red). Surface melt duration and extent measurements are derived from daily Special Sensor Microwave Imager/Sounder (SSMIS) 37 GHz, horizontally polarized passive microwave radiometer satellite data (Mote 2007). (c) Net ablation (represents ice loss) in 2021 measured by PROMICE weather transects and referenced to a 1981–2010 standard period. Circle size is scaled to the ablation in m of ice equivalent and color-scaled with anomaly value. White circles indicate anomaly values not exceeding methodological and measurement uncertainty. Stations are: Thule (THU), Upernavik (UPE), Kangerlussuaq (KAN), Nuuk (NUK), Qassimuit (QAS), Tasiliiq (TAS), Scorebysund (SCO), and Kronprins Christians Land (KPC). NSF Summit Station is also marked.

(following Van As et al. 2016), which show significantly above-average ablation along the central western and eastern Greenland coasts (Fig. 5.12c).

The stark contrast between ice sheet conditions in early and late summer is also reflected in measurements of ice sheet broadband albedo (relative amount of energy reflected by the surface in all wavelength bands) and bare glacial ice exposure (Fig. 5.13). A low albedo (dark) ice sheet surface absorbs sunlight and can enhance ice melt, while a high albedo (bright) surface can reflect sunlight and reduce melt potential. Snow can create a high albedo surface while a dark surface can result from exposure of bare glacial ice, snow grain growth, organic and inorganic surface materials (e.g., microbes or black carbon), etc.

An above-average July albedo was offset by a below-average August albedo, creating an overall average June–August albedo (Fig. 5.13b). Regionally, brighter-than-normal southwest conditions and darker-than-normal northern conditions are evident (Fig. 5.13a). The regionally-opposing anomalies obscure a temporal shift that is clearer in the bare ice area variation (Fig. 5.13c), which reached extremely large area values that rivaled 2019, an extreme ice loss year. August 2021 had the latest peak in bare ice area during the past five years (2017–21). The local ablation (Fig. 5.12b) and albedo anomalies (Fig. 5.13a) may not intuitively align due to factors such as summer snowfall, surface atmospheric conditions, and extreme melt events (e.g., Box et al. 2022).

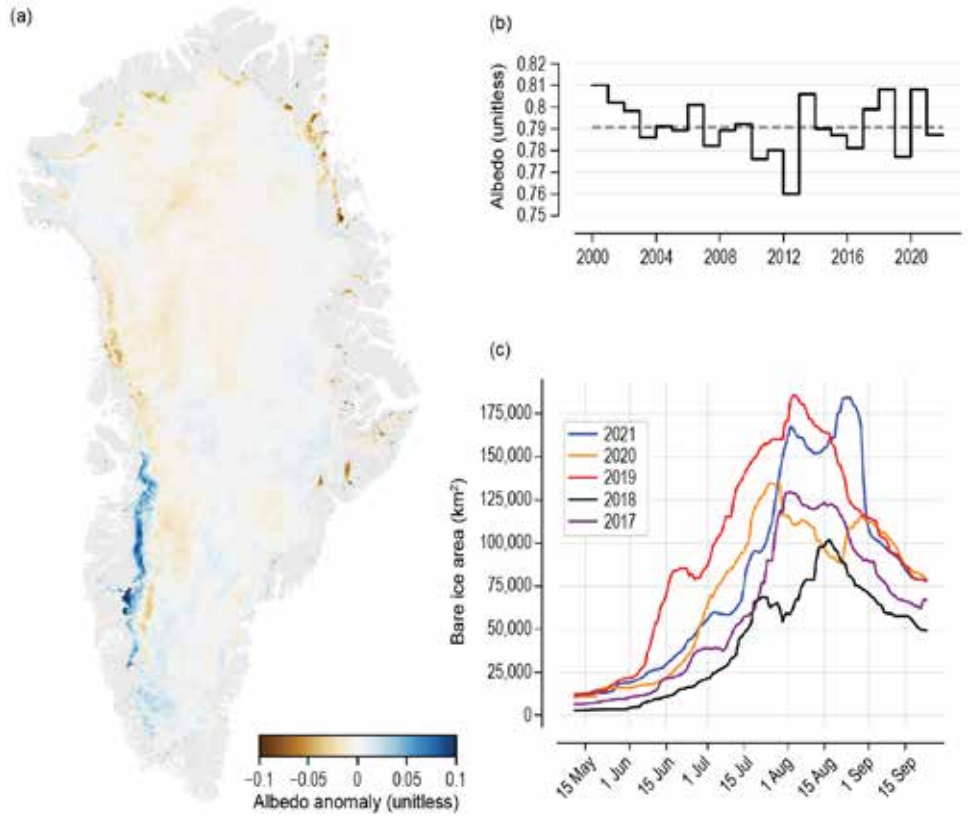

Fig. 5.13. (a) Albedo anomaly for summer 2021, relative to a 2000–09 reference period. NASA MODIS satellite data provide multi-decadal albedo monitoring (Box et al. 2017). (b) Time series for average Greenland Ice Sheet summer albedo from MODIS. (c) Bare ice area (km^2) from the Sentinel-3 SICE product (Kokhanovsky et al. 2020; Wehrlé et al. 2021).

Along with ice loss via melt, the Greenland Ice Sheet also loses mass via breaking off of solid ice, hereafter 'discharge', into the ocean at the ice sheet–ocean boundaries (Fig. 5.14), though mass loss variability is dominated by surface mass gain/loss, not solid ice discharge (Mankoff et al. 2020). The 2010–19 solid ice discharge averaged ~−487 ± 46 Gt yr^{-1}, and the 1981–2010 average is ~−444 ± 47 Gt yr^{-1}. Solid ice discharge for January–December 2021 was −496 ± 48 Gt, with the southeast remaining the largest contributor (Fig. 5.14a).

If solid ice discharge is more rapid than replacement from ice flow, the glacier front retreats and glacier area is lost. For 2020/21, net glacier surface area loss due to retreat was −18.9 km^2 for 47 major and representative Greenland tidewater glaciers (Fig. 5.14b,c), substantially lower than the mean annual area loss of −103.3 km^2 for these glaciers since 2002 (Andersen et al. 2019).

Despite moderate ice loss for 2020/21, the year brought unprecedented conditions to the ice sheet. Based on the 1978–present satellite record, the anomalous melt event centered on 14 August was the latest on record that affected more than half of the ice sheet (> 815,000 km^2). Further, 2021 is only the second year on record (the other is 2012) with more than one melt event on this scale. Year 2021 was also the first time that rainfall was reported at NSF's Summit Station (operations began in 1989), though surface melting without rainfall was observed at Summit in 1995, 2012, and 2019. The exceptional August rainfall was associated with an atmospheric river (a concentrated poleward flow of heat and moisture). This rain episode increased snow and ice melt and lowered surface albedo between 0.4 and 0.1, contributing to anomalously high late meltwater production in 2021. According to the MARv3.12 model forced by fifth ECMWF Reanalysis (ERA5; Hersbach et al. 2020) data, the amount of rainfall across the ice sheet (75 Gt yr^{-1}) in 2021 was the highest since at least 1950, with an anomaly of +103% with respect to the 1991–2020 baseline. The model-derived meltwater runoff (−445 Gt yr^{-1}) was 20% larger in 2021 than the baseline, with 2021 producing the fifth-highest surface melt after 2012, 2019, 2010, and 2016. Along with the

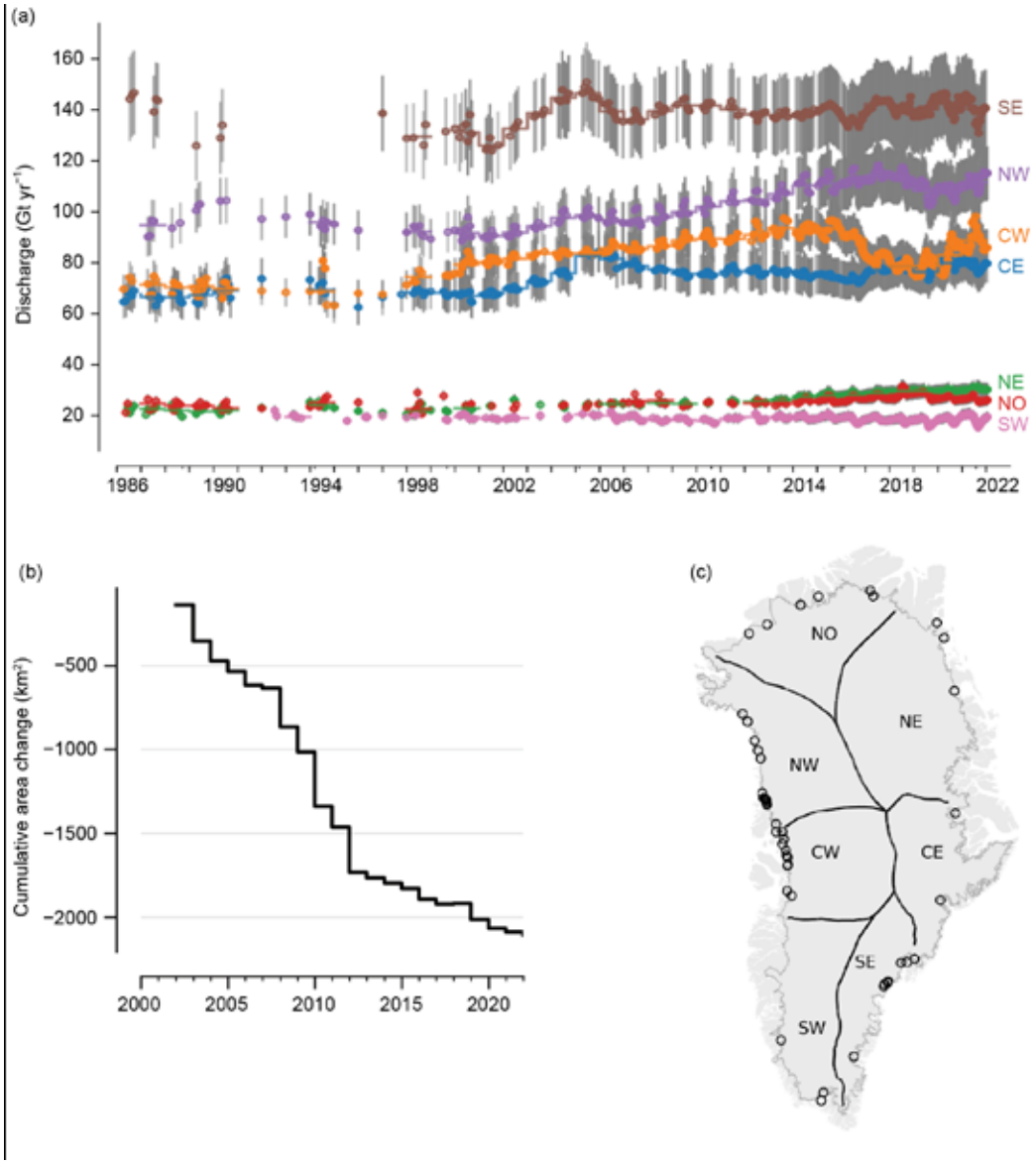

Fig. 5.14. (a) Solid ice discharge (Gt yr^{-1}; gray bars show ±10% uncertainty range). PROMICE combines ice thickness estimates with ice velocity measurements based on Sentinel-1 satellite data to create a high temporal resolution solid ice discharge product (representing ice loss) integrated over Greenland (following Mankoff et al. 2020). (b) Cumulative total area change at 47 major Greenland tidewater glaciers. (c) Regions for solid ice discharge (a): north (NO), northeast (NE), central east (CE), southeast (SE), southwest (SW), central west (CW), and northwest (NW) and sampled glaciers for (b) indicated with open circles.

exceptional summer rainfall (73 Gt yr^{-1}, representing an anomaly of +120%), 10% larger snowfall accumulation than average (711 Gt yr^{-1}) counterbalanced the excess of melt to give a total surface mass balance close to the 1991–2020 average.

f. Glaciers and ice caps outside Greenland—D. Burgess, G. Wolken, B. Wouters, L. M. Andreassen, J. Kohler, F. Pálsson, E. Baker, B. Luks, L. Thomson, and T. Thorsteinsson

The Arctic hosts 63% of the world's mountain glaciers and ice caps by area outside of the ice sheets of Greenland and Antarctica (RGI Consortium 2017; Fig. 5.15). While their potential longer-term contribution to sea level rise is small compared to the ice sheets, they are sensitive to changes in climate and have been a large contributor to recent sea level rise in response to continued atmospheric warming (Ciracì et al. 2020; Hugonnet et al. 2021; Millan et al. 2017; Wouters et al. 2019). Recent increases in global temperature, amplified at high northern latitudes (section 5b, Fig. 5.1), have accelerated melt rates of Arctic glaciers and ice caps three-fold since the mid-1990s

(Zemp et al. 2019). Observations of monitored Arctic glaciers and ice caps from 2020 and 2021 show regional and inter-annual variations in mass change, with a continuing trend of significant ice loss throughout the Arctic, especially in Alaska and Arctic Canada.

Glaciers and ice caps gain mass through surface accumulation (snow, rime, freezing rain) and lose mass by surface melt and runoff, and by iceberg calving where they terminate in oceans or lakes. The total mass balance is thus defined as the difference between annual accumulation and annual mass losses (by iceberg calving plus runoff; Ostrem and Brugman 1991). Of the 27 Arctic glaciers currently monitored, only Kongsvegen, Hansbreen, and Devon Ice Cap (NW) lose mass by iceberg calving, which is not accounted for in this study (World Glacier Monitoring Service [https://wgms.ch/] 2021). For all glaciers discussed, we report the climatic mass balance (B_{clim}, the difference between annual accumulation and annual runoff), which is a measure of annual thickness change (millimeters water equivalent, mm w.e.) averaged across the entire glacier or ice cap basin.

We report B_{clim} for the 2020/21 mass balance year (September 2020 to August 2021) for the 20 monitored Arctic glaciers for which mass balance data were available. These glaciers are located in Arctic Canada (three), Svalbard (three), Alaska (three), Iceland (nine), and Norway (two). Because some of these data are still provisional, we provide added context to recent changes in pan-Arctic glacier mass balance by also reporting on the 24 glaciers measured in the previous mass balance year of 2019/20 (World Glacier Monitoring Service [https://wgms.ch/] 2021; Kjøllmoen et al. 2021). These glaciers are located in Alaska (three), Arctic Canada (four), Iceland (nine), Svalbard (three), Norway (two), and Sweden (three; Fig. 5.15). Cumulative measurements of B_{clim} record regional variations in thinning which range from ~–14 m w.e. across glaciers in Arctic Canada (1959–2021) to ~–35 m w.e. for glaciers in Alaska (1953–2021), with an overall average of ~–24 m w.e. for all regions combined (Fig. 5.16).

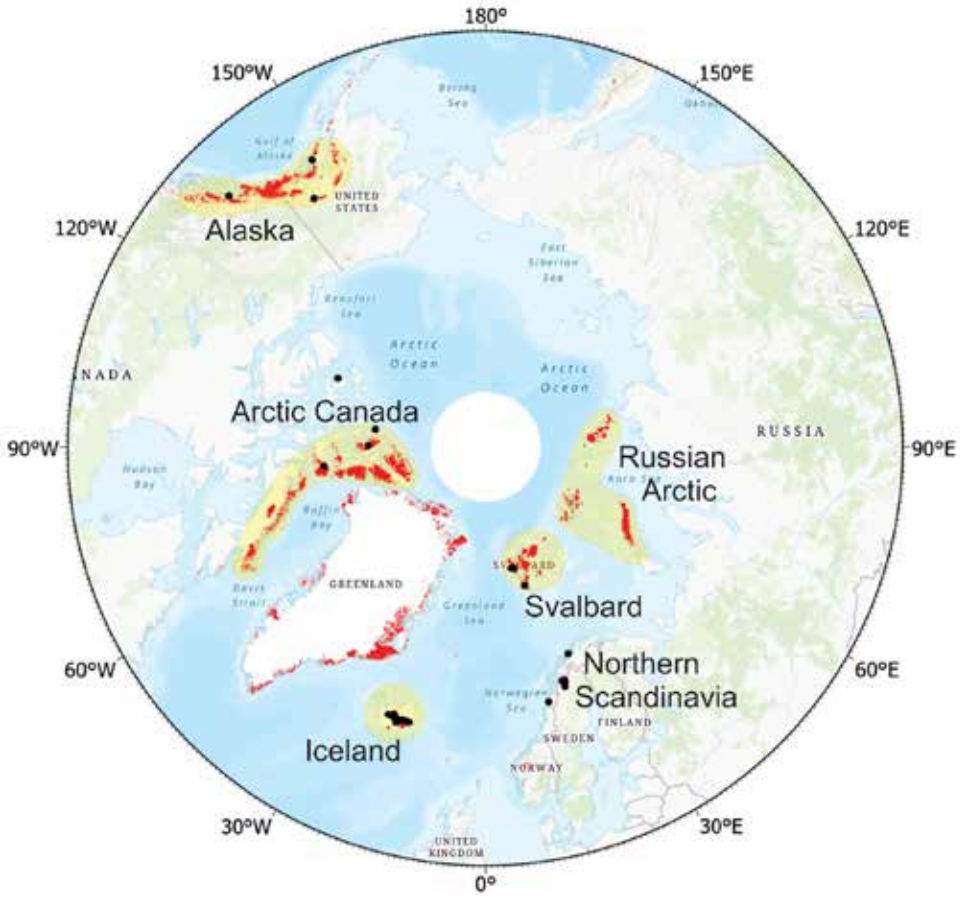

Fig. 5.15. Arctic glaciers and ice caps (red), including ice caps in Greenland that are separate from the ice sheet. Yellow shading shows the GRACE- and GRACE-FO-derived mass anomaly domains, used to estimate changes in regional annual glacier mass balance for heavily glacierized Arctic regions. Black dots indicate long-term Arctic glacier monitoring sites.

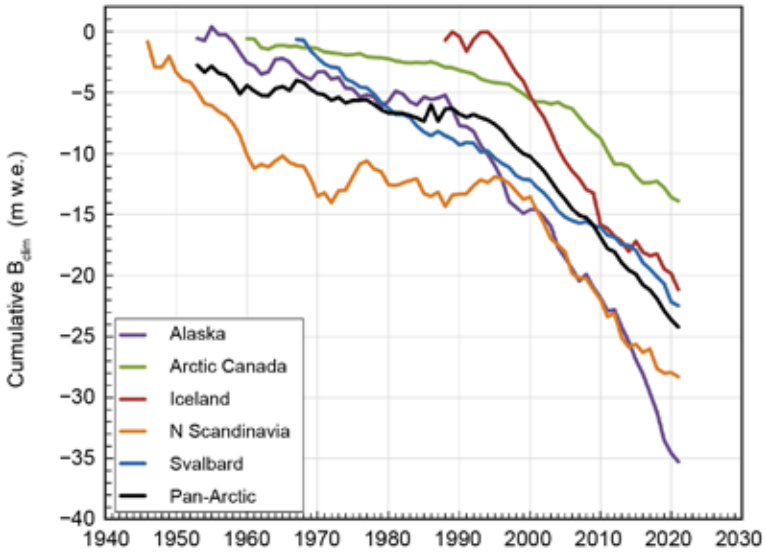

Fig. 5.16. Cumulative B_{clim} in meters of water equivalent (m w.e.) for monitored glaciers in five regions of the Arctic and for the Arctic as a whole (pan-Arctic). Regional climatic mass balances are derived as arithmetic means for all monitored glaciers within each region for each year, and these means are summed over the period of record. Due to homogenization and calibration of mass balance datasets from Norwegian glaciers (Andreassen et al. 2016), post-1970 cumulative thickness change values for North Scandinavia are more negative than reported previously in Wolken et al. (2020). (Source: Data are from the World Glacier Monitoring Service [WGMS 2021: https://wgms.ch/].)

Average B_{clim} of –735 mm w.e. across pan-Arctic glaciers and ice caps in the mass balance year 2019/20 represented the 14th most negative balance since 1960. Regionally, the greatest thinning occurred over Svalbard, where record negative values of B_{clim} were recorded for Midtre Lovénbreen (–1590 mm w.e.), Austre Brøggerbreen (–1740 mm w.e.), and Kongsvegen (–1140 mm w.e.). Negative B_{clim} of –795 mm w.e. averaged across monitored glaciers and ice caps in the Canadian Arctic Archipelago was consistent with post-2005 melting which has been about four times greater than the 1960–2004 average (Sharp et al. 2011). Thinning by ~1 m across Alaskan glaciers in 2019/20 mass balance year corresponded to a moderately negative B_{clim} anomaly (–446 mm w.e.) relative to the 1981–2010 mean.

Surface mass balance and overall state-of-health of Arctic glaciers and ice caps is closely linked with summer warmth (Box et al. 2019). Strongly negative values of B_{clim} for glaciers and ice caps across Svalbard in the 2019/20 balance year were associated with summer (June–August, JJA) atmospheric temperature (925 hPa; NCEP/NCAR) anomalies 2.5° to 3°C above the 1981–2010 mean (Ballinger et al. 2020). Similarly, near-record high melting across glaciers and ice caps in the Canadian Arctic coincided with positive temperature anomalies (+1.5° to +2°C; NCEP/NCAR) recorded for summer 2020 (Ballinger et al. 2020). Radiosonde temperature data (JJA, 850 hPa) collected by the Government of Canada in 2020 registered the first and second highest JJA (850 hPa) positive anomalies on record at Resolute Bay and Eureka, Nunavut, weather stations, respectively (Fig. 5.17). In the 2019/20 balance year, a strong positive B_{clim} anomaly for Engabreen in northern Scandinavia (522 mm w.e. higher than the 1981–2010 average) coincided with the fifth-highest winter accumulation on record (WGMS 2021).

Average surface mass balance of pan-Arctic glaciers and ice caps in 2020/21 was overall less negative (by 132 mm w.e.) than in the 2019/20 balance year (Fig. 5.17b). Strongly negative balances, however, prevailed across Icelandic glaciers for which an average B_{clim} of –1278 mm w.e. represented the third most negative mass balance across this region since measurements began in 1986. Enhanced glacier melt over northern Iceland, relative to southern Iceland, was associated with summer (July–September) temperatures in excess of 3°C above the 1981–2010 average (section 5b).

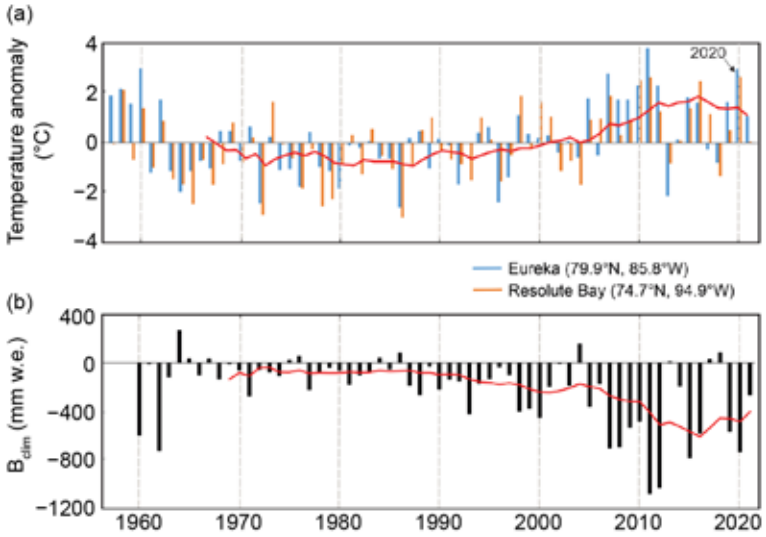

Fig. 5.17. (a) Annual temperature anomalies (°C) derived from the Integrated Global Radiosonde Archive (Imke et al. 2016) and (b) average climatic mass balance (B_{clim}; mm w.e.) for monitored glaciers in the Canadian High Arctic. Solid red lines indicate decadal averages. Summer temperature anomalies (JJA 850 hPa) and B_{clim} are strongly correlated with Pearson correlation coefficients of −0.8 and −0.97 for annual and decadal correlations, respectively, over approximately six decades for which overlapping measurements are available. Near-record high temperature anomalies in 2020 correspond to the fifth most negative B_{clim} measured since 1960.

Glaciers and ice caps at high northern latitudes have been increasingly important contributors to global sea level rise since the early 1990s (Box et al. 2018). Gravity anomalies measured from the combined GRACE (2002–16) and GRACE-FO (2018–21) satellite missions indicate that pan-Arctic glaciers and ice caps have consistently lost mass since 2002 at an average rate of –174 ± 24 Gt yr^{-1} (Fig. 5.18), or ~66% of the annual mass loss from the Greenland Ice Sheet (including Greenland peripheral glaciers and ice caps) over the same period (section 5e). Uncertainties in the GRACE measurements were estimated at two standard deviations and include corrections for glacial isostatic adjustment and terrestrial hydrology as per Wouters et al. (2019). An increase in the rate of annual mass loss over the 19-year period (2002–21), relative to the previously reported

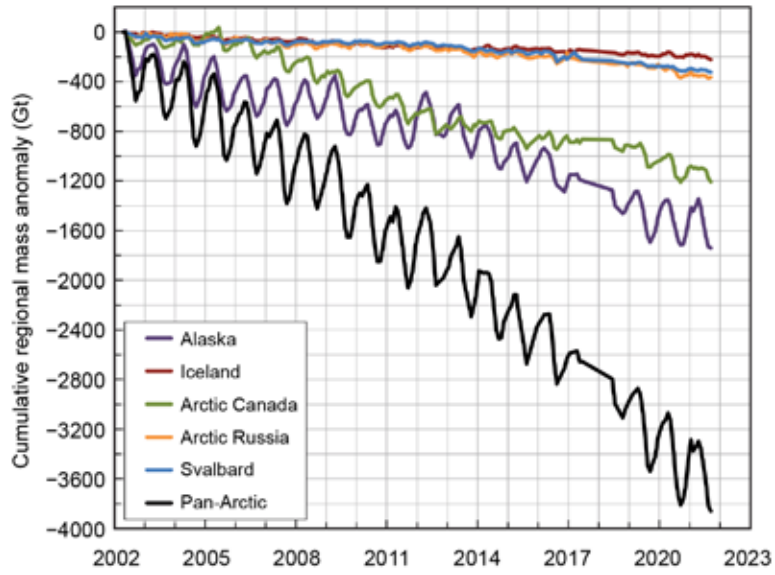

Fig. 5.18. Cumulative changes in regional total stored water (Gt) for 2002–21 derived from GRACE (https://www.nasa.gov/mission_pages/Grace/index.html) and GRACE-FO (https://gracefo.jpl.nasa.gov/) satellite gravimetry for the five regions shown in Fig. 5.15 and for the total of these five regions (i.e., pan-Arctic). Linear interpolation is applied through a measurement gap between the GRACE and GRACE-FO missions from Jul 2017 to May 2018.

annual average of –165 ± 26 Gt yr^{-1} (Wolken et al. 2020) for 2002–16, was driven largely by extreme mass losses of –432 ± 28 Gt in the 2018/19 balance year. Sustained losses in 2019/20 (–272 ± 30 Gt) were influenced primarily by Arctic Canada (44%) and the Russian Arctic (27%) where glaciers and ice caps lost mass about five times faster than the 2002–21 average. For the 2020/21 balance year, near-zero change in glacier mass was measured across both the Alaska (–24 ± 46 Gt) and Arctic Canada (+3 ± 23 Gt) regions. Total loss of –752 ± 52 Gt from pan-Arctic glaciers and ice caps between September 2018 and August 2021 contributed 2.05 ± 0.14 mm to global sea level rise, or 0.69 ± 0.05 mm yr^{-1} over this 3-year period.

g. Terrestrial snow cover—L. Mudryk, A. Elias Chereque, C. Derksen, K. Luojus, and B. Decharme

Many components of the Arctic land surface are directly influenced by snow cover from autumn through spring, including the surface energy budget and ground thermal regime, with implications on the carbon cycle, permafrost, and terrestrial and freshwater ecosystems (Brown et al. 2017; Meredith et al. 2019 and references therein). Even following the snow cover season, the influence of spring snow melt timing persists through impacts on river discharge timing and magnitude, surface water, soil moisture, vegetation phenology, and fire risk (Meredith et al. 2019).

Historical snow cover extent (SCE) anomalies during spring are shown separately for the North American and Eurasian terrestrial sectors of the Arctic in Fig. 5.19 relative to the 1981–2010 baseline (data from the NOAA snow chart climate data record; Robinson et al. 2012). In 2021, Eurasian Arctic SCE anomalies were strongly negative during both May (fifth lowest in the record since 1967) and June (third lowest). North American Arctic SCE anomalies in 2021 were also below average (14th and 16th lowest, respectively).

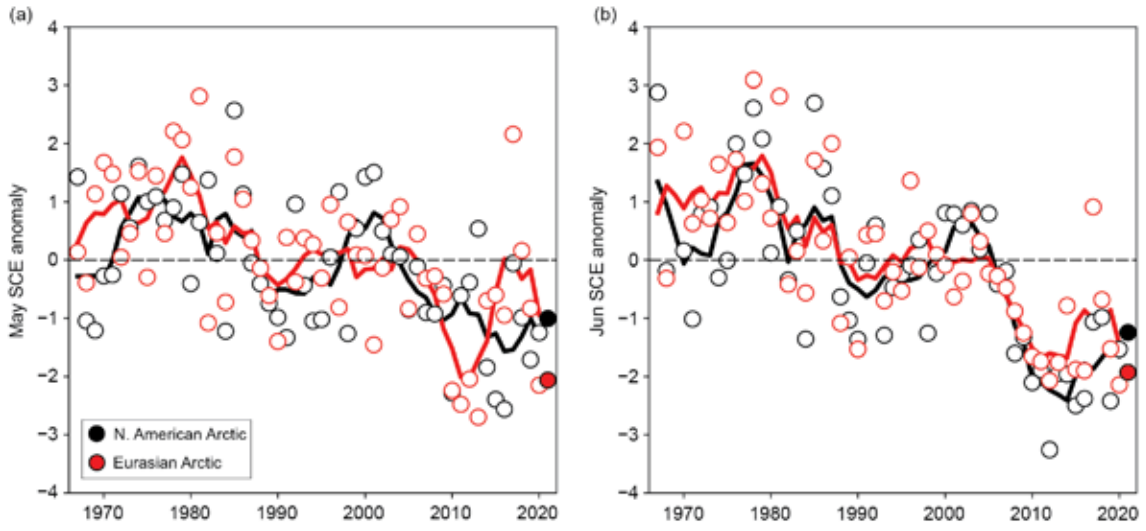

Fig. 5.19. Monthly snow cover extent (SCE) anomalies for Arctic terrestrial land areas (> 60°N) for (a) May and (b) Jun from 1967 to 2021. Anomalies are relative to the average for 1981–2010 and standardized (each observation differenced from the mean and divided by the standard deviation, and thus unitless). Solid black and red lines depict 5-yr running means for North America and Eurasia, respectively. Filled circles are used to highlight 2021 anomalies. (Source: Robinson et al. 2012.)

Snow cover duration (SCD) anomalies (1999–2021 baseline) across the Arctic region for the 2020/21 snow season are shown in Figs. 5.20a,b as percent differences relative to the climatological number of snow-free days (data from the NOAA daily Interactive Multisensor Snow and Ice Mapping System snow cover product; U.S. National Ice Center 2008). Anomalies in the total number of days with snow cover were computed separately for each half of the snow season: August 2020 to January 2021, referred to as "onset period," and February to July 2021, referred to as "melt period." Onset anomalies indicate snow cover during autumn 2020 began later than normal over much of Eurasia, particularly in eastern Siberia, as well as over much of Alaska and the western

Canadian Arctic (Fig. 5.20a). Spring 2021 (Fig. 5.20b) had early snow melt and hence shorter snow cover duration over almost the entire Arctic. In particular, across broad expanses of Eurasia the duration of the spring snow-free period was 30–50% longer than normal. The early Eurasian melt in 2021 was driven by persistent, above-average temperatures during April–June (section 5b).

Snow water equivalent (SWE; equivalent mass where the snowpack is converted to water) characterizes the amount of snow at a location as well as the contribution of that snow to the hydrological cycle once it melts. March–June SWE fields were obtained from four daily-frequency gridded products over the 1981–2021 period: (1) the European Space Agency Snow CCI SWE version1 product derived through a combination of satellite passive microwave brightness temperatures

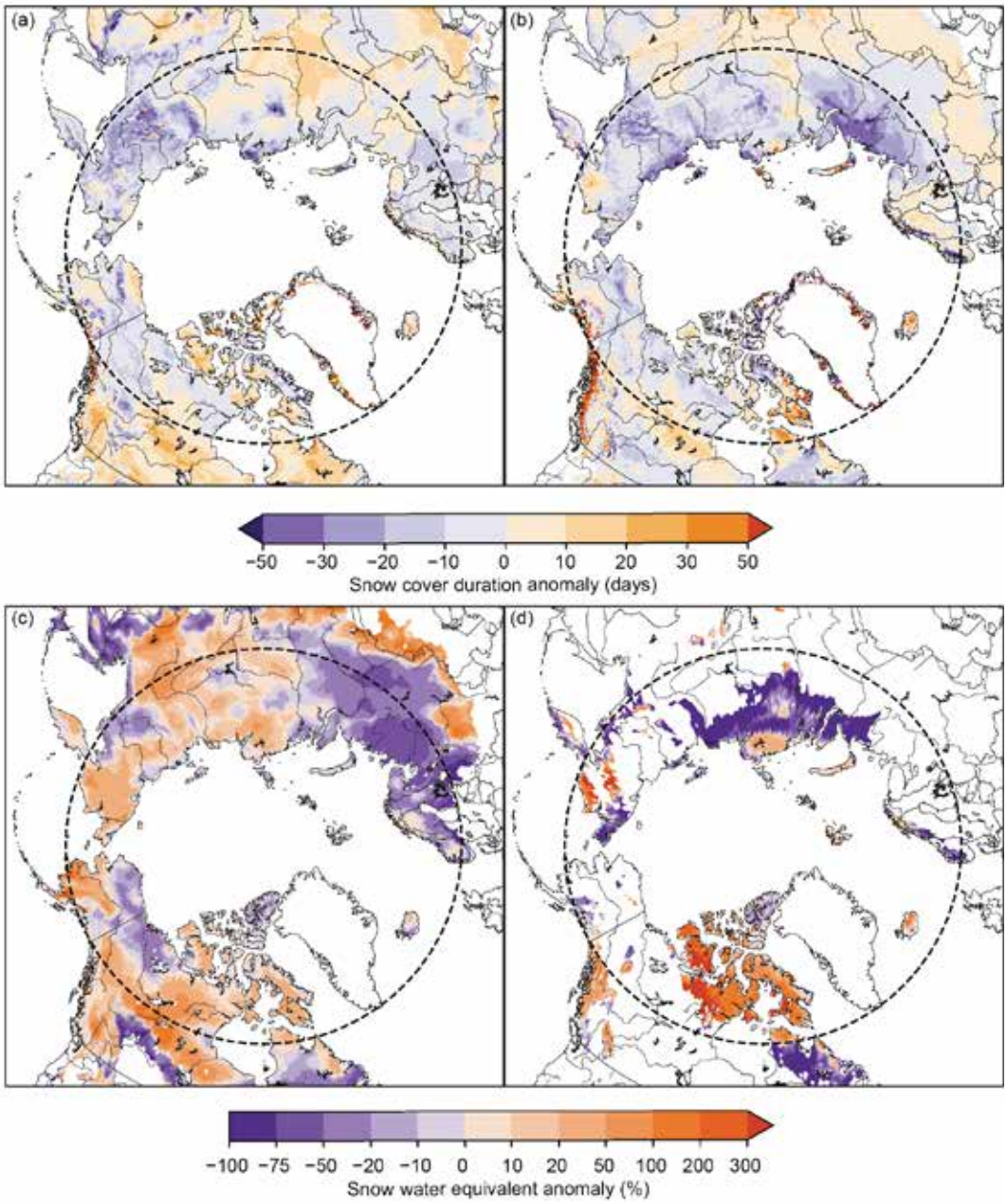

Fig. 5.20. Snow cover duration (SCD) anomalies (% difference relative to climatological number of snow-free days for the 1999–2021 baseline) for the 2020/21 snow year: (a) snow onset period (Aug 2020–Jan 2021) and (b) snow melt period (Feb 2021–Jul 2021). Purple (orange) indicates fewer (more) days with snow cover relative to the 1999–2021 mean. Snow water equivalent (SWE) anomalies (% difference from the 1981–2010 baseline) in 2021 for (c) Apr and (d) Jun. Purple (orange) indicates less (more) snow than average. Latitude 60°N marked by gray dashed circle; land north of this defines the Arctic terrestrial area considered in this study. (Sources: (a,b) U.S. National Ice Center (2008); (c,d) four SWE products from Snow CCI [Luojus et al. 2020], MERRA2 [GMAO 2015]; ERA5 [Muñoz Sabater 2019], Crocus [Brun et al. 2013].)

and climate station snow depth observations (Luojus et al. 2020); (2) the Modern-Era Retrospective Analysis for Research and Applications version 2 (MERRA-2, GMAO 2015) daily SWE fields; (3) SWE output from the ERA5-Land analysis (Muñoz Sabater 2019); and (4) the physical snowpack model Crocus (Brun et al. 2013) driven by ERA5 meteorological forcings. Reduced availability of climate station snow depth measurements limits the accuracy of the Snow CCI SWE product during May and June, hence it is only used during March and April. An approach using gridded products is required because in situ observations are too sparse to be representative of hemispheric snow conditions, especially in the Arctic.

For April, the SWE fields from each product are aggregated across Arctic land regions (> 60°N) for both North American and Eurasian sectors and standardized relative to the 1981–2010 baseline to produce standardized April snow mass anomalies. The ensemble mean anomalies and the range of estimates among the products are presented in Fig. 5.21. April is chosen because it is the approximate seasonal snow mass peak for the terrestrial pan-Arctic region, reflecting total snowfall accumulations since the preceding autumn before increasing temperatures during May and June lead to melt. The 2021 anomalies highlighted in Fig. 5.20 indicate above-normal total snow accumulation during the 2020/21 snow season in the North American Arctic and slightly below-average accumulation over the Eurasian Arctic. Figure 5.20c illustrates the SWE spatial distribution during both April and June, presented as percent differences of the ensemble-mean field relative to the 1981–2010 baseline. While snow accumulation across Eurasia was near-normal through March (not shown), the high spring temperatures (mentioned above) began to drive SWE reductions across western Eurasia by April (also see April–June temperature anomaly pattern in section 5b). Eastern Eurasian SWE was still above normal in April as seen in Fig 5.20 but decreased to below normal by May (not shown; also see April–June temperature anomaly pattern in section 5b). In contrast to Eurasia, SWE across North America generally remained above normal through June, particularly in the Canadian Arctic Archipelago (Fig. 5.20d). However, even where SWE was seasonally above average, complete snow melt tended to occur slightly earlier than usual over most of the region. This combination of increased snow accumulation (expressed as April SWE in Fig. 5.20c) but early snow melt (expressed by shorter snow cover duration in Fig. 5.20b) is consistent with the expected changes to Arctic snow cover in a warmer Arctic (Meredith et al. 2019) and also reflected in earlier and larger peak river discharge as observed over Eurasia during spring 2020 (Holmes et al. 2021).

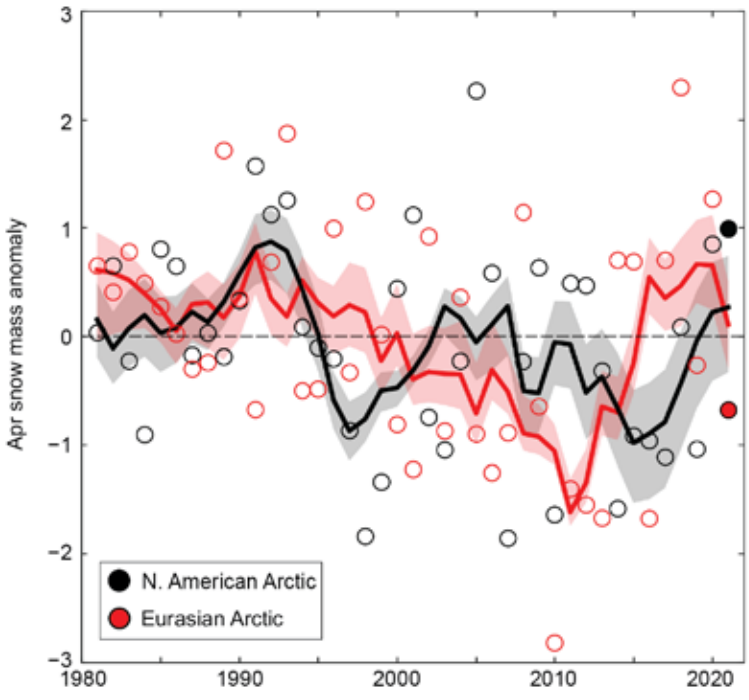

Fig. 5.21. Mean April snow mass anomalies for Arctic terrestrial areas calculated for North American (black) and Eurasian (red) sectors of the Arctic for 1981–2021. Anomalies are relative to the average for 1981–2010 and standardized (each observation differenced from the mean and divided by the standard deviation, and thus unitless). Filled circles are used to highlight 2021 anomalies. Solid black and red lines depict 5-yr running means for North America and Eurasia, respectively, and the spread among the running means for individual datasets is shown in shading. (Sources: four SWE products from Snow CCI [Luojus et al. 2020], MERRA2 [GMAO 2015]; ERA5 [Muñoz Sabater 2019], and Crocus [Brun et al. 2013].)

In summary, snow accumulation during the 2020/21 winter was near-normal across the Eurasian Arctic and above normal across the North American Arctic. Despite no significant negative trend in

snow mass (Fig. 5.21), spring snow extent has been persistently below normal for the last 15 years (Fig. 5.19), reflecting earlier snow melt. Since 2006, North American June SCE has been below the long-term average every year, while Eurasian June SCE has been below the long-term average for all but one year.

h. Permafrost—S. L. Smith, V. E. Romanovsky, K. Isaksen, K. E. Nyland, A. L. Kholodov, N. I. Shiklomanov, D. A. Streletskiy, D. S. Drozdov, G. V. Malkova, and H. H. Christiansen

Permafrost refers to earth materials (e.g., bedrock, mineral soil, organic matter) that remain at or below 0°C for at least two consecutive years and underlies extensive regions of the high-latitude landscape (Brown et al. 1997). Overlying the permafrost is the active layer, which thaws and refreezes annually. Permafrost, especially where it contains large volumes of ice, can play a critical role in the stability of Arctic landscapes. Warming of permafrost, active layer thickening, and ground ice melt cause changes in surface topography, hydrology, and landscape stability, with implications for Arctic infrastructure and ecosystem integrity and human lifestyles (Romanovsky et al. 2017; Bjella 2019; Wolken et al. 2021). Changes in permafrost conditions can also affect the rate of carbon dioxide and methane release to the atmosphere, with the potential to accelerate global warming (Schuur 2020).

Permafrost conditions respond to shifts in the surface energy balance through a combination of interrelated changes in ground temperature and active layer thickness (ALT). Ground temperatures fluctuate seasonally near the surface, while below the depth of seasonal temperature variation, ground temperature reflects longer-term changes in climate. Long-term changes in permafrost temperatures are driven by changes in air temperature (Romanovsky et al. 2017); however, permafrost temperature trends also show local variability due to other important influences such as snow cover, vegetation characteristics, and soil moisture. Monitoring sites across the Arctic (Fig. 5.22) have been recording ground temperature in the upper 30 m for up to five decades, providing critical data on changes in permafrost stability. Observed changes in ALT are more reflective of shorter-term (year-to-year) fluctuations in climate and are especially sensitive to changes in summer air temperature and precipitation.

Data collection was affected less by COVID-19 related travel restrictions in 2021 compared to 2020. However, for some sites there has been data loss for 2020 and 2021 (Figs. 5.23, 5.24).

1) PERMAFROST TEMPERATURES

Permafrost temperatures continue to increase across the Arctic. Greater increases in permafrost temperature are generally observed in colder permafrost at higher latitudes (Smith et al. 2021, 2022), where the largest increases in air temperature were observed (Figs. 5.22, 5.23). Although permafrost temperatures in 2021 were higher than those observed in 2020 and the highest on record at many sites, recent cooling occurred at some sites (Fig. 5.23, Table 5.1). In northern Alaska for example, permafrost temperatures in 2021 were up to 0.2°C lower than in 2020 at some sites while at others, such as Utqiaġvik (Barrow), permafrost temperatures continue to increase (Fig. 5.23a). Observed permafrost cooling was a result of decreasing mean annual air temperatures (e.g., at Deadhorse station air temperatures were 2.5°C lower in 2020 and 2021 compared to 2018 and 2019). Lower permafrost temperatures were also observed in northwestern Canada in the northern Mackenzie region (NC–01). In the Alaskan interior, the 2021 permafrost temperature was higher at all sites except for Old Man, where the temperature was slightly lower in 2021 than in 2020 (Fig. 5.23b). In the Nordic high-Arctic cold permafrost of Svalbard, each year since 2005 has been warmer than the previous one until 2019/20 (Smith et al. 2021). Although permafrost temperatures decreased in 2021 (Fig. 5.23d), these values were the third highest in the longest record dating back to 1998 (Janssonhaugen).

Throughout the Arctic, the response of permafrost with temperatures close to 0°C (i.e., warm permafrost sites at temperatures > –2°C) is slower (generally < 0.3°C decade^{-1}) than

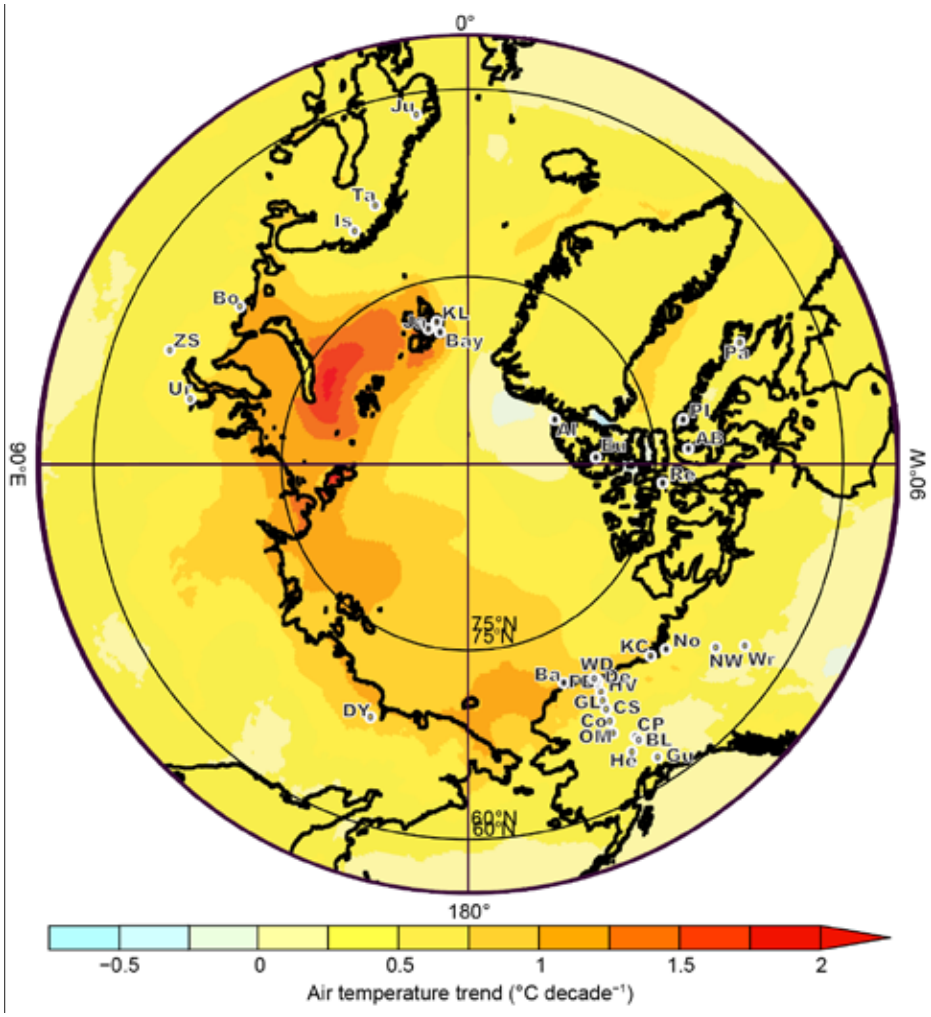

Fig. 5.22. Locations of the permafrost temperature monitoring sites (for which data are shown in Fig. 5.23), superimposed on average surface air temperature trend (°C decade^{-1}) during 1981–2020 from the ERA5-reanalysis (Hersbach et al. 2020). Reanalysis data provided by the COPERNICUS climate data store (https://cds.climate.copernicus.eu). See Table 5.1 for site names. Information about these sites is available at http://gtnpdatabase.org/, http://permafrost.gi.alaska.edu/sites_map, https://www2.gwu.edu/~calm/.

colder permafrost sites due to latent heat effects related to melting ground ice. At cold continuous permafrost sites in the Beaufort-Chukchi region, permafrost temperatures have increased by 0.33–0.76°C decade^{-1} (Fig. 5.23a; Table 5.1). In the eastern and high Canadian Arctic, similar increases (0.4–0.7°C decade^{-1}) have been observed (Fig. 5.23c; Table 5.1). Permafrost on Svalbard at the Janssonhaugen and Kapp Linne sites (Table 5.1), has warmed by 0.7°C decade^{-1} since 2000.

Although rates of warming were lower in warm permafrost, temperatures in these locations generally increased. In the discontinuous permafrost regions of Scandinavia (Juvvasshøe and Iskoras), warming reported by Etzelmüller et al. (2020) is continuing, with 2021 permafrost temperatures being the highest measured (Fig. 5.23d). Similar rates of warming were found for warm permafrost in Russia (e.g., Bolvansky #56; Malkova et al. 2022) and northwestern North America (Figs. 5.23b,d).

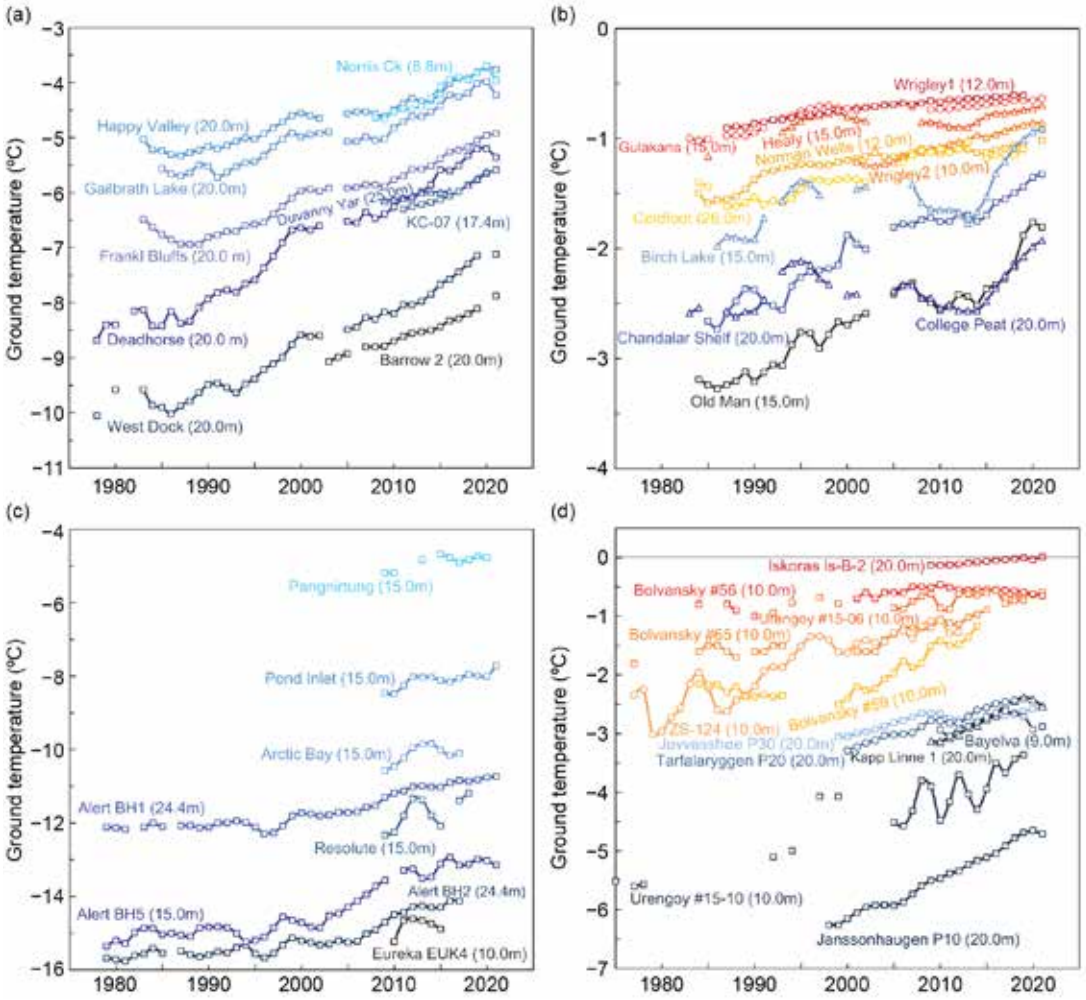

Fig. 5.23. Time series of mean annual ground temperature (°C) at depths of 9–26 m below the surface at selected measurement sites that fall roughly into Adaptation Actions for a Changing Arctic Project priority regions (see Romanovsky et al. 2017): (a) cold continuous permafrost of northwestern North America and northeastern East Siberia (Beaufort–Chukchi region); (b) discontinuous permafrost in Alaska and northwestern Canada; (c) cold continuous permafrost of eastern and High Arctic Canada (Baffin Davis Strait); (d) continuous to discontinuous permafrost in Scandinavia, Svalbard, and Russia/Siberia (Barents region). Temperatures are measured at or near the depth of zero annual amplitude where the seasonal variations of ground temperature are less than 0.1°C. Note differences in y-axis value range. Borehole locations are shown in Fig. 5.22. (Sources: Data are updated from Christiansen et al. 2010; Smith et al. 2021; Boike et al. 2018; and Etzelmüller et al. 2020.)

Table 5.1. Rate of change in mean annual ground temperature (°C decade^{-1}) for permafrost monitoring sites shown in Fig. 5.22. For sites where measurements began prior to 2000, the rate of change for the entire available record and the period after 2000 are provided. The periods of record are shown in parenthesis below the rates of change. The names of the stations with record high temperatures in 2021 are shown in red. * denotes sites not reporting in 2021.

Subregions	Sites	Entire Record	Since 2000
Beaufort-Chukchi Region			
North of East Siberia	Duvany Yar (DY)*	NA	+0.44 (2009–20)
Alaskan Arctic plain	West Dock (WD), Deadhorse (De), Franklin Bluffs (FB), Barrow (Ba)	+0.40 to +0.76 (1978–2021)	+0.47 to +0.67 (2000–21)
Northern foothills of the Brooks Range, Alaska	Happy Valley (HV), Galbraith Lake (GL)	+0.33 to +0.36 (1983–2021)	+0.36 to +0.47 (2000–21)
Northern Mackenzie Valley	Norris Ck (No), KC-07(KC)	NA	+0.7 (2008–21)
Discontinuous Permafrost Alaska and Northwestern Canada			
Southern foothills of the Brooks Range, Alaska	Coldfoot (Co), Chandalar Shelf (CS), Old Man (OM)	+0.12 to +0.36 (1983–2021)	+0.21 to +0.4 (2000–21)
Interior Alaska	College Peat (CP), Birch Lake (BL), Gulkana (Gu), Healy (He)	+0.09 to +0.30 (1983–2021)	+0.04 to +0.26 (2000–21)
Central Mackenzie Valley	Norman Wells (NW), Wrigley (Wr)	Up to +0.1 (1984–2021)	<+0.1 to +0.2 (2000–21)
Baffin Davis Strait Region			
Baffin Island	Pangnirtung (Pa)*, Pond Inlet (PI)	NA	+0.4 (2009–21)
High Canadian Arctic	Resolute (Re)*	NA	+0.7 (2009–18)
High Canadian Arctic	Alert (Al) @15m Alert (Al) @24m	+0.6 +0.4 (1979–2021)	+0.9 +0.6 (2000–21)
Barents Region			
North of West Siberia	Urengoy 15-06 and 15-08 (Ur)*	+0.20 to +0.48 (1974–2021)	+0.08 to +0.81 (2005–21)
Russian European North	Bolvansky 56, and 65 (Bo)	+0.09 to +0.27 (1984–2021)	+0.02 to +0.51 (2001–21)
Svalbard	Janssonhaugen (Ja), Bayelva (Bay), Kapp Linne 1 (KL)	+0.7 (1998–2021)	+0.5 to +0.7 (2000–21)
Northern Scandinavia	Tarfalarggen (Ta)*, Iskoras Is-B-2 (Is)	NA	+0.1 to +0.5 (2000–21)
Southern Norway	Juvvasshøe (Ju)	+0.2 (1999–2021)	+0.2 (2000–21)

2) ACTIVE LAYER THICKNESS

Three common methods for monitoring active layer thickness (ALT) are: direct measurement with mechanical probing, interpolation of the maximum seasonal depth of the 0°C isotherm from borehole temperatures, or thaw tube records. The majority of sites comprising trends shown in Fig. 5.24 are based on mechanical probing to determine the top of permafrost (Shiklomanov et al. 2012).

Distinct positive trends in ALT are evident since 1996 for the interior of Alaska, Greenland, Svalbard, the Russian European North, and West Siberia (Fig. 5.24), but trends are less apparent for the Alaskan North Slope, Canada, and East Siberia (Smith et al. 2022). Sites in interior Alaska and Greenland experienced ALTs in 2021 well above the 2003 to 2012 mean, similar to the preceding three years. Positive anomalies in 2021 were also reported for the Russian European North and West and East Siberia (Kaverin et al. 2021). The interior of Alaska and the Russian European North are experiencing the greatest rates of ALT increase over the 25-year observation period at 0.015 and 0.013 m yr^{-1}, respectively. The reduced ALT reported in 2021 for sites in Svalbard and East Siberia, for example, could be due to short-term cooling, as significant thickening trends have been reported for these regions (Strand et al. 2021; Abramov et al. 2021).

Average ALT in 2021 for the North Slope of Alaska and Chukotka were within 0.01 m of the 2003 to 2012 mean values. Thaw-induced consolidation (subsidence), which is common in ice-rich permafrost, is not accounted for in manual probing measurements, and these data alone may underestimate ALT (Nyland et al. 2021). Correcting manual probing data for ground surface displacement can therefore allow better detection of climate trends.

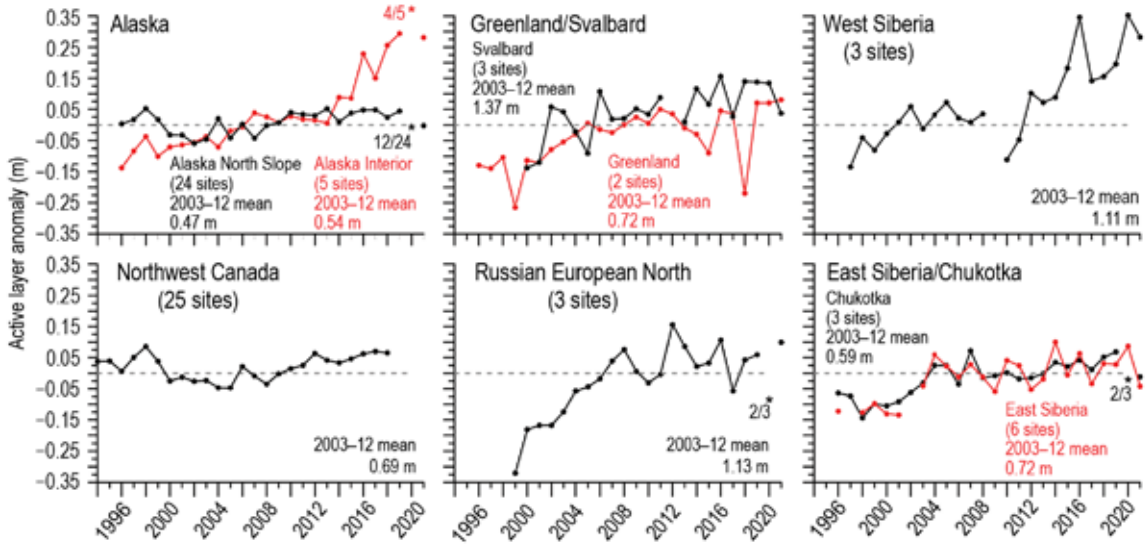

Fig. 5.24. Long-term active layer thickness anomalies in six different Arctic regions as observed by the Circumpolar Active Layer Monitoring (CALM) program. The data are shown as annual anomalies (m) relative to the mean value for the reference period 2003–12. Positive and negative anomaly values indicate the active layer is thicker or thinner than the 10-yr mean values, respectively. The number of sites varies by region (numbers provided on figure) because only sites with > 20 years of continuous thaw depth observations from the end of the thaw season were included. Asterisks on the figure represent 2020 and 2021 data, as observations from fewer sites (number provided beside asterisks) were possible due to pandemic-related restrictions. Note that there are no ALT data for northwestern Canada after 2018 due to travel restrictions (measurements are made by thaw tubes and observations represent maximum thaw depths from the previous year). Site-specific data and metadata are available at www2.gwu.edu/~calm/.

i. Tundra greenness—G. V. Frost, M. J. Macander, U. S. Bhatt, L. T. Berner, J. W. Bjerke, H. E. Epstein, B. C. Forbes, S. J. Goetz, M. M. P. D. Heijmans, M. J. Lara, R. Í Magnússon, T. Park, G. K. Phoenix, J. E. Pinzon, S. P. Serbin, H. Tømmervik, C. J. Tucker, D. A. Walker, and D. Yang

Earth's northernmost continental landmasses and island archipelagos are home to the Arctic tundra biome, a 5.1 million km^2 region characterized by low-growing, treeless vegetation adapted to short, cool summers (CAVM Team 2003). The Arctic tundra biome has become a "hotspot" of global environmental change because vegetation and underlying permafrost soils are strongly influenced by ongoing climatic warming and sea ice loss on the nearby Arctic Ocean (Bhatt et al. 2021; sections 5b,d). In the late 1990s, a strong increase in the productivity of tundra vegetation began to emerge in global satellite observations, a phenomenon known as "the greening of the Arctic." Arctic greening is dynamically linked with Earth's changing climate, permafrost, seasonal snow, and sea ice cover, and has motivated multi-disciplinary scientific efforts to understand its causes and consequences (Myers-Smith et al. 2020).

Tundra greenness has been monitored from space for 40 years using the Normalized Difference Vegetation Index (NDVI), a spectral metric that is strongly correlated with the biomass of aboveground vegetation (Raynolds et al. 2012). Here, we analyze tundra greenness trends using two spaceborne datasets. The first satellite record of tundra greenness began in 1982 using the Advanced Very High Resolution Radiometer (AVHRR), a sensor that continues to operate onboard polar-orbiting satellites. Tundra greenness has also been independently monitored since 2000 by the Moderate Resolution Imaging Spectroradiometer (MODIS), a separate satellite-based sensor with improved calibration and 500-m spatial resolution. For AVHRR, we analyze the Global Inventory Modeling and Mapping Studies 3g V1.2 dataset (GIMMS-3g+) that is produced using daily observations at approximately 8-km spatial resolution (Pinzon and Tucker 2014). For MODIS, we analyze daily Nadir Bidirectional Reflectance Distribution Function Adjusted Reflectance data at 500-m spatial resolution (MCD43A4, version 6; Schaaf 2021). All data were masked to include only ice-free land within the extent of the Circumpolar Arctic Vegetation Map (CAVM Team 2003; as shown in Figs. 5.25 and 5.27). We summarize the AVHRR and MODIS records for annual maximum NDVI (MaxNDVI), representing the annual peak greenness which is achieved in midsummer.

Both AVHRR and MODIS records indicate that MaxNDVI increased across most of the Arctic tundra biome since 1982 and 2000, respectively (Figs. 5.25a,b). Several Arctic regions display particularly strong trends in both records. In North America, increases have been strongest in

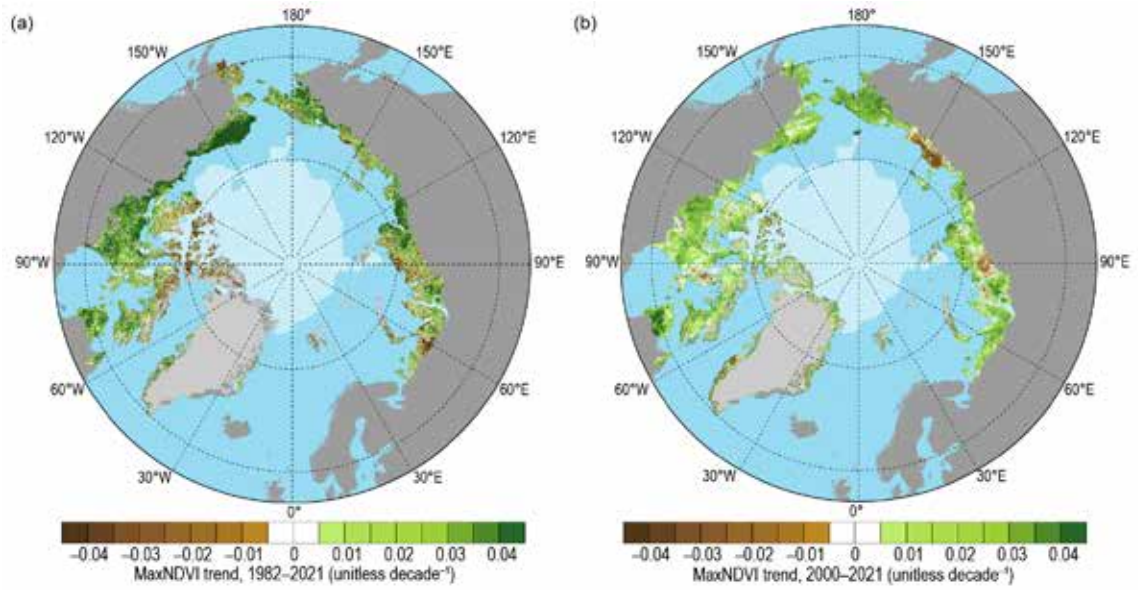

Fig. 5.25. Magnitude of the MaxNDVI trend calculated as the change decade^{-1} via ordinary least squares regression for (a) 1982–2021 based on the AVHRR GIMMS 3-g+ dataset and (b) 2000–21 based on the MODIS MCD43A4 dataset. The 2021 minimum sea ice extent is indicated by light shading in each panel.

northern Alaska and mainland Canada, while flat or negative trends are evident in parts of the Canadian Arctic Archipelago and southwestern Alaska. In Eurasia, strong greening has occurred in Chukotka, but MaxNDVI declines are evident in the East Siberian Sea sector and parts of the Taymyr Peninsula. AVHRR and MODIS have recorded divergent trends in northwestern Siberia and the European Arctic, potentially due to the different observational periods of the two records.

In 2021, circumpolar mean MaxNDVI declined from the record high values set the previous year for both datasets. AVHRR-observed MaxNDVI declined 8.3% from 2020; nonetheless, the 2021 value still exceeded the 1991–2010 mean value and represented the 15th highest value recorded in the full 40-year record (Fig. 5.26). The 2021 decline in MaxNDVI from 2020 was less pronounced for MODIS (2.7%); the 2021 value was the second highest value in the 22-year record for that sensor, and circumpolar values have now exceeded the 2000–20 mean for the last 11 growing seasons. Circumpolar MaxNDVI time series for the two sensors show virtually identical trends for the period of overlap (2000–20), although the AVHRR record displays higher variability (i.e., "noise"), particularly over the last 10 years of the record. This is likely due in part to AVHRR's lower spatial resolution and less advanced calibration compared to MODIS.

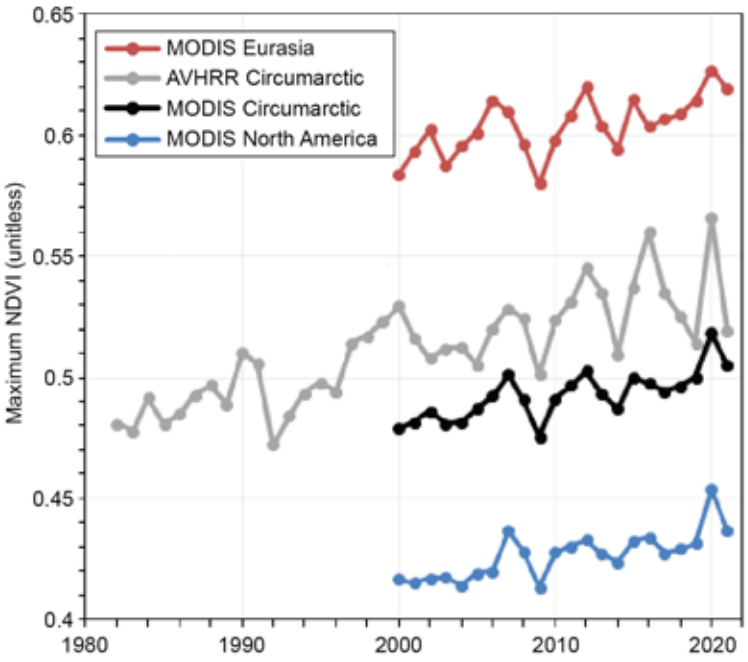

Fig. 5.26. Time series of MaxNDVI from the MODIS MCD43A4 (2000–21) dataset for the Eurasian Arctic (red), North American Arctic (blue), and the circumpolar Arctic (black), and from the long-term AVHRR GIMMS-3g+ dataset (1982–2021) for the circumpolar Arctic (gray).

Regional contrasts in greenness highlight the dynamic linkages between tundra ecosystems and the local characteristics of sea ice, permafrost, seasonal snow, soil composition and moisture, disturbance regimes, wildlife, and human activities (Campbell et al. 2021; Heijmans et al. 2022; Seider et al. 2022). For example, in 2021, several regional MaxNDVI anomalies suggest potential relationships to surface air temperature and sea ice extent (Fig. 5.27). Strong positive and negative MaxNDVI anomalies were evident in the Taymyr Peninsula and the Canadian Arctic Archipelago, respectively, coincident with unusually warm and cool growing season temperatures in the two regions (section 5b).

What biological and physical mechanisms underlie satellite observations of Arctic greening, and what types of change might be apparent to a field observer? Persistent increases in the abundance and height of Arctic shrubs have been widely documented across the Arctic, with wide-ranging impacts to tundra biomass, biodiversity, surface energy balance, permafrost temperatures, biogeochemical cycling, and wildlife (Kropp et al. 2021; Way and Lapalme 2021; Mekonnen et al. 2021; Tape et al. 2021). Circumpolar greening also signals changes to the timing of phenological events and the duration of the Arctic growing season (Parmentier et al. 2021; Karlsen et al. 2021; see section 2h4), with implications for seasonal movements and life-history events of migratory animals such as caribou and reindeer (Severson et al. 2021).

Although spaceborne observations provide unequivocal evidence of Arctic greening, substantial regional variability exists, and some parts of the Arctic exhibit little or no long-term trend (Berner et al. 2020; Huemmrich et al. 2021). Some regions, most notably the East Siberian Sea sector, exhibit declining tundra productivity, which is thought to be related to surface subsidence

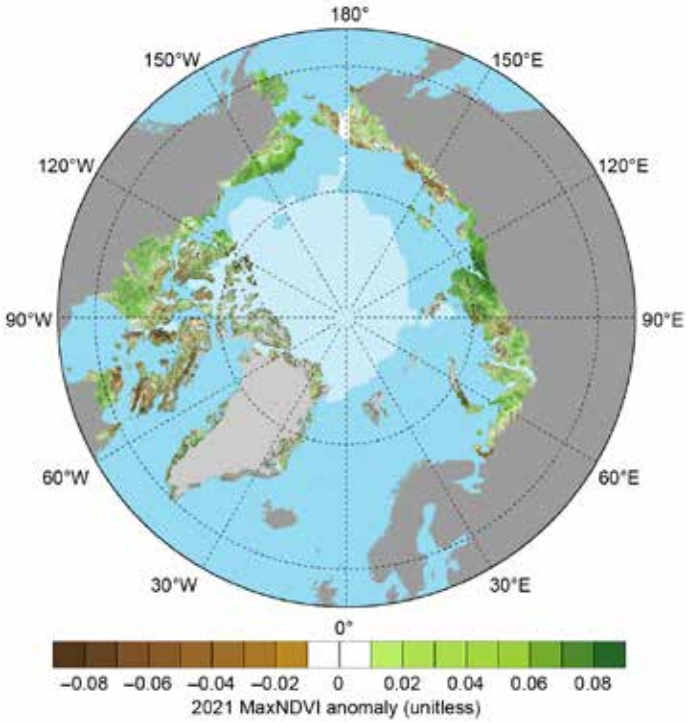

Fig. 5.27. Circumpolar MaxNDVI anomalies for the 2021 growing season relative to mean values (2000–20) from the MODIS MCD43A4 dataset. The 2021 minimum sea ice extent is indicated by light shading.

and increased surface water resulting from thaw of ice-rich permafrost (van Huissteden et al. 2021; Veremeeva et al. 2021; section 5h). Wildfire, extreme weather events, herbivory, and other ecological disturbances introduce additional complexity in Arctic greenness trends (Gaglioti et al. 2021; Magnússon 2021; Veselkin 2021; Talucci et al. 2022). While warming is likely to continue to drive Arctic greening, extreme events and other causes of regional or localized NDVI decline are also increasing in frequency (Christensen et al. 2021), highlighting the emergence of increased variability as a component of Arctic climate change.

j. Ozone and UV radiation—G. H. Bernhard, V. E. Fioletov, J.-U. Grooß, I. Ialongo, B. Johnsen, K. Lakkala, G. L. Manney, R. Müller, and T. Svendby

Past emissions of man-made chlorine-containing substances, such as chlorofluorocarbons (CFCs), have caused substantial chemical depletion of stratospheric ozone (WMO 2018). The resulting ozone loss led to increases of ultraviolet (UV) radiation at Earth's surface with adverse effects on human health and the environment (Barnes et al. 2019; EEAP 2019). The chemical destruction of polar ozone occurs within a cold stratospheric cyclone known as the polar vortex, which forms over the North Pole every winter (WMO 2018). The polar vortex between November 2020 and April 2021 was weakened by a Sudden Stratospheric Warming (SSW; see Sidebar 5.2) event in early January 2021 that decreased depletion of stratospheric ozone in the Northern Hemisphere until at least April. A similar SSW event occurred in January 2013. The progressions of chemical ozone loss in the winters of 2012/13 and 2020/21 are therefore compared below.

1) OZONE

Chemical processes that drive ozone depletion in the polar stratosphere are initiated at temperatures below about 195 K (–78°C) at altitudes of approximately 15 to 25 km. These low temperatures lead to the formation of polar stratospheric clouds (PSCs), which act as a catalyst to transform inactive forms of chlorine-containing substances into active, ozone-destroying chlorine species such as chlorine monoxide (ClO).

Temperatures were low enough for PSC formation by mid-November 2020 as observed by the Aura Microwave Limb Sounder (MLS, 2005–present; Waters et al. 2006). Activation of chlorine started in late November 2020, and ClO concentrations at ~16 km altitude between 20 December 2020 and 10 January 2021 were exceeded only by those in 2012/13 in the MLS data record (Fig. 5.28a). If cold conditions had persisted beyond December 2020, this could have led to large Arctic ozone depletion in spring 2021, like that observed in spring 2020 (Manney et al. 2020). Instead, similar to the behavior in 2012/13 (Manney et al. 2015a), an unusually early major SSW on 5 January 2021 warmed the lower stratosphere above temperatures at which active chlorine can be maintained. ClO concentrations subsequently declined to near-zero between 10 and 25 January as ClO was converted back to inactive forms of chlorine.

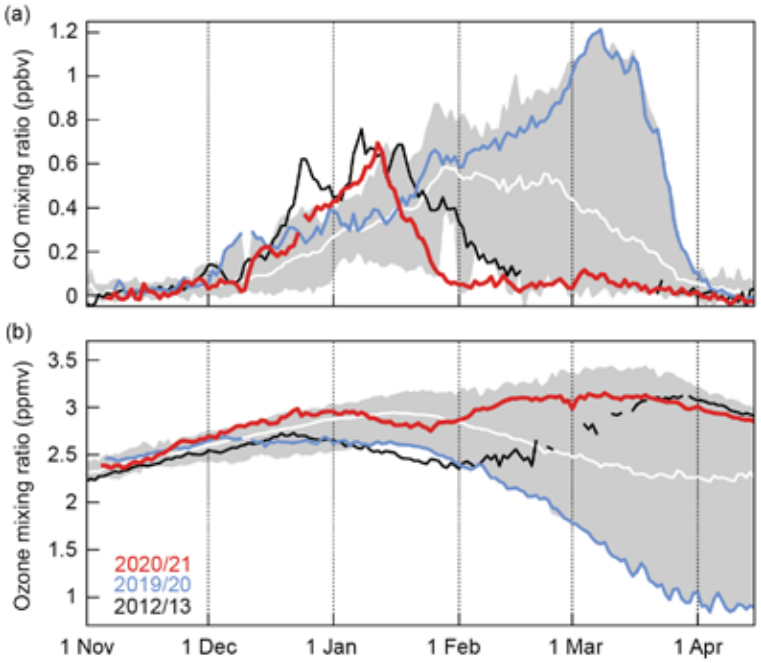

Fig. 5.28. Average (a) daytime ClO (expressed as ClO mixing ratio in ppbv) and (b) ozone concentrations (ozone mixing ratio in ppmv) measured by Aura MLS at an altitude of ~16 km for the area bounded by the Arctic stratospheric polar vortex. Data from 2012/13 (black), 2019/20 (blue), and 2020/21 (red) are compared with the average (solid white) and minimum/maximum range (gray shading) from 2004/05 to 2019/20, excluding 2012/13. Gaps in the 2012/13 record are periods where the polar vortex was not well defined (Manney et al. 2015a).

In both winters of 2012/13 and 2020/21, chemical ozone destruction involving ClO started in late December and continued through January, as evidenced by the decline in ozone mixing ratios (Fig. 5.28b). The rapid drop in ClO halted further chemical ozone loss in late January in both years, and ozone mixing ratios rebounded to be among the highest in the MLS record by mid-March. The faster rebound in 2021 compared to 2013 can be explained by the differences in the polar vortex structure between the two years and may also be related to differences in planetary wave activity (see Sidebar 5.2), which affects ozone transport from low to polar latitudes. The high ozone concentrations at ~16 km between mid-February and April 2021 were exceeded only by those in 2013 (Manney et al. 2015a), 2015 (Manney et al. 2015b), and 2019.

The evolution of ozone in 2020/21 is in stark contrast to that in 2019/20, when the lowest ozone values in the MLS record resulted from an exceptionally strong, cold, and persistent stratospheric polar vortex (e.g., Lawrence et al. 2020; Manney et al. 2020).

The early termination of chemical ozone loss in the lower stratosphere during winter/spring 2020/21 led to average Arctic total ozone columns (TOC; i.e., ozone amounts integrated from Earth's surface to the top of the atmosphere) between January and July. Figure 5.29 illustrates the variation in TOC between 1979 and 2021 for March by showing the minimum of the daily mean TOC within an area that encloses the polar vortex and is surrounded by the 63°N contour of "equivalent latitude" (Butchart and Remsberg 1986). March was selected because this has historically been the month with the largest potential for chemical ozone depletion in the Arctic (WMO 2018). In March 2021, the minimum Arctic daily TOC was 374 Dobson units (DU), which was identical to the average TOC since the start of satellite observations in 1979 and 2% (8 DU) above the average of 365 DU for the period of measurements (2005–present) by MLS and the Ozone Monitoring Instrument (OMI).

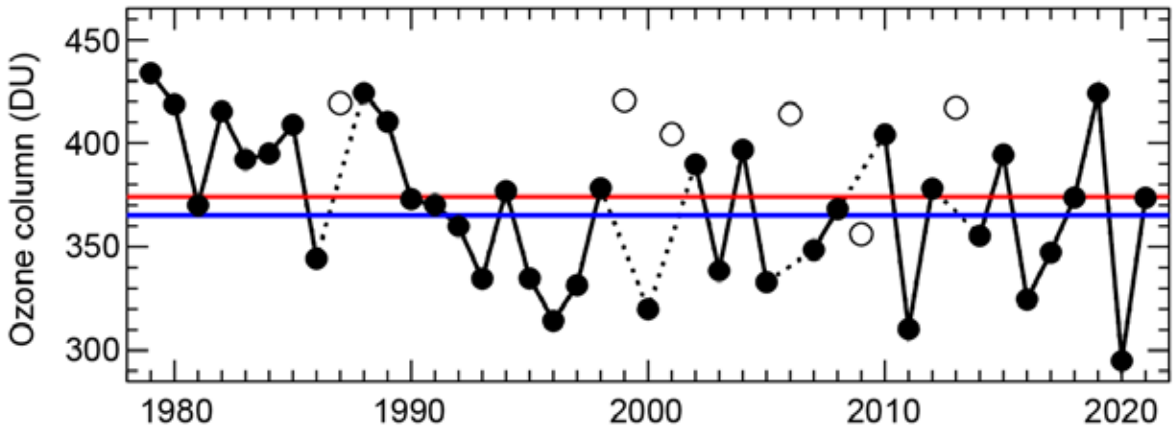

Fig. 5.29. Minimum of the daily average total ozone column (Dobson units, DU) for Mar poleward of 63°N equivalent latitude (Butchart and Remsberg 1986). Open circles represent years in which the polar vortex was not well-defined in Mar, resulting in relatively high values owing to mixing with lower latitude air masses and a lack of significant chemical ozone depletion. Red and blue lines indicate the average total ozone column for 1979–2020 and 2005–20, respectively. Ozone data for 1979–2019 are based on the combined NIWA-BS total column ozone database version 3.5.1 (Bodeker et al. 2021). Ozone data for 2020/21 are from the OMI. The graph is adapted from Müller et al. (2008) and WMO (2018), and updated using ERA5 reanalysis data (Hersbach et al. 2020) for determining equivalent latitude.

2) ULTRAVIOLET RADIATION

Ultraviolet radiation is quantified with the UV index (UVI), which measures the ability of UV radiation to cause erythema (sunburn) in human skin (WHO 2002). In addition to its dependence on TOC, the UVI depends on the sun angle, clouds, aerosols, and surface albedo (Weatherhead et al. 2005). In the Arctic, the UVI scale ranges from 0 to about 7; UVI values north of 80°N remain below 3. For comparison, the summertime UVI at midlatitudes may reach 12 ([Bernhard at al. 2022]).

Figures 5.30c,d quantify spatial differences in monthly average noontime UVIs from past (2005–20) averages based on measurements by OMI. UVI differences in March 2021 (Fig. 5.30c) varied by up to ± 58% but remained within 2 std. dev. of past observations, with few exceptions. The larger variability compared to TOC (Fig. 5.30a) can be explained by the added effect from clouds. UVIs in April 2021 (Fig. 5.30d) were elevated beyond 2 std. dev. north of Alaska (consistent with the low TOCs for this region; Fig. 5.30b), a small band east of Greenland, and a small region in Northwest Russia. Since TOCs for these regions were close to average, the elevated UVI was likely caused by unusually clear skies. While UVI anomalies assessed with satellite (OMI) data provide complete spatial coverage, they can sometimes indicate spurious anomalies of up to 59% (Bernhard et al. 2015), for example when the surface albedo (reflectivity) assumed in the retrieval algorithm (Tanskanen et al. 2003) deviates from the actual albedo. UVI anomalies for 2021 derived from OMI data generally agree with ground-based measurements at 10 Arctic and sub-Arctic sites (indicated in Figs. 5.30c,d) within ± 11%. The only exception is Eureka in April where measurements at the ground indicate a 14% larger anomaly than OMI data, likely due to the uncertainty in the OMI albedo climatology.

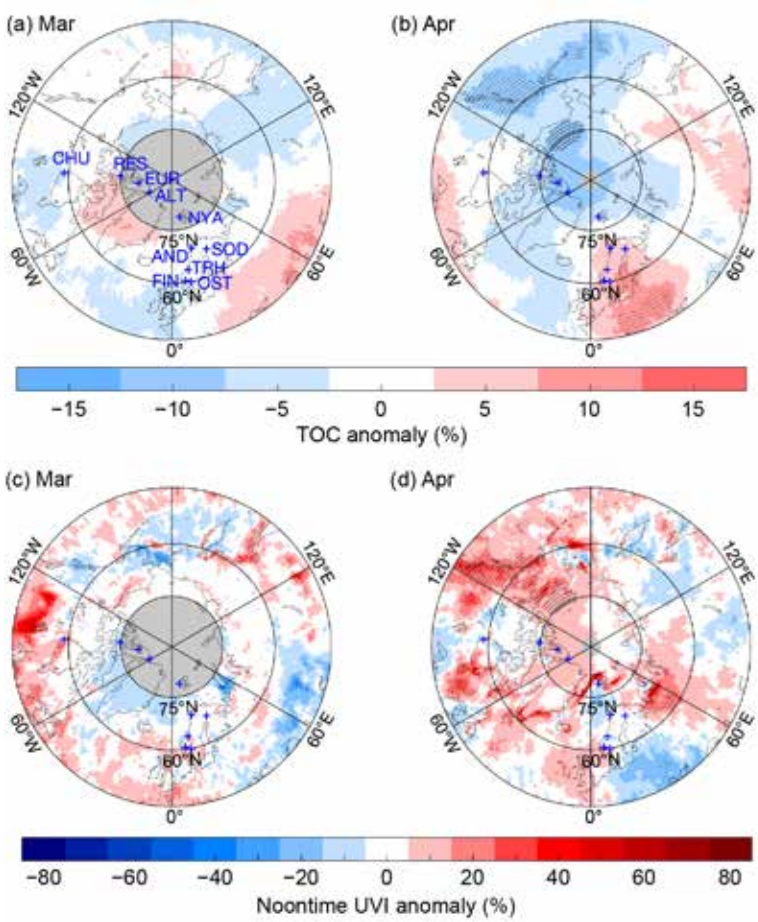

Fig. 5.30. Monthly mean anomaly maps of (a,b) TOC (%) and (c,d) noontime UVI (%) for Mar and Apr 2021 relative to 2005–20 means. Stippling indicates pixels where anomalies exceed 2 std. dev. Gray-shaded areas centered at the North Pole indicate latitudes where no OMI data are available because of polar darkness. Locations of ground stations are indicated by blue crosses in every map, with labels added to the first map. Maps are based on the OMTO3 Level 3 total ozone product (Bhartia and Wellemeyer 2002). Site abbreviations are ALT: Alert (83°N); EUR: Eureka (80°N); NYA: Ny-Ålesund (79°N); RES: Resolute (75°N); AND: Andøya (69°N); SOD: Sodankylä (67°N); TRH: Trondheim (63°N); FIN: Finse (61°N); OST: Østerås (60°N); and CHU: Churchill (59°N).

SIDEBAR 5.2: THE 2021 ARCTIC SUDDEN STRATOSPHERIC WARMING—A. H. BUTLER AND S. H. LEE

A major Sudden Stratospheric Warming (SSW) occurred in the Arctic on 5 January 2021 (Lee 2021). During an SSW, the climatological westerly winds of the wintertime polar stratosphere—the stratospheric polar vortex—decelerate and temperatures in the polar stratosphere rapidly increase (Baldwin et al. 2021). Large perturbations in stratospheric temperatures and winds can descend to the lower stratosphere where they persist for many weeks, affecting both the stratospheric ozone layer (section 5j), as well as the likelihood of cold Arctic air outbreaks and other weather extremes (Domeisen and Butler 2020). This sidebar describes the January 2021 SSW and its influence on stratospheric ozone and weather in the weeks that followed.

Cause and evolution of the event

Tropospheric and stratospheric winds are strongly coupled via interactions between the mean wind flow and planetary-scale atmospheric waves, which are generated primarily by land–sea contrasts, topography, and convective heating. Disturbances to the stratospheric polar vortex in the form of SSWs arise when these large-scale waves either amplify vertically from the troposphere into the stratosphere or when waves are created within the stratosphere from resonance (Baldwin et al. 2021).

In late December 2020, persistent tropospheric weather patterns led to the amplification of planetary-scale atmospheric

waves into the stratosphere. In particular, a low pressure system over the North Pacific and a high pressure system over the North Atlantic and Eurasia formed a "wavenumber-1" type pattern (i.e., one trough and one ridge around a latitude circle) that then amplified into the stratosphere. A wavenumber-2 pattern (i.e., two troughs and two ridges around a latitude circle) also contributed during the onset of the event (Lu et al. 2021).

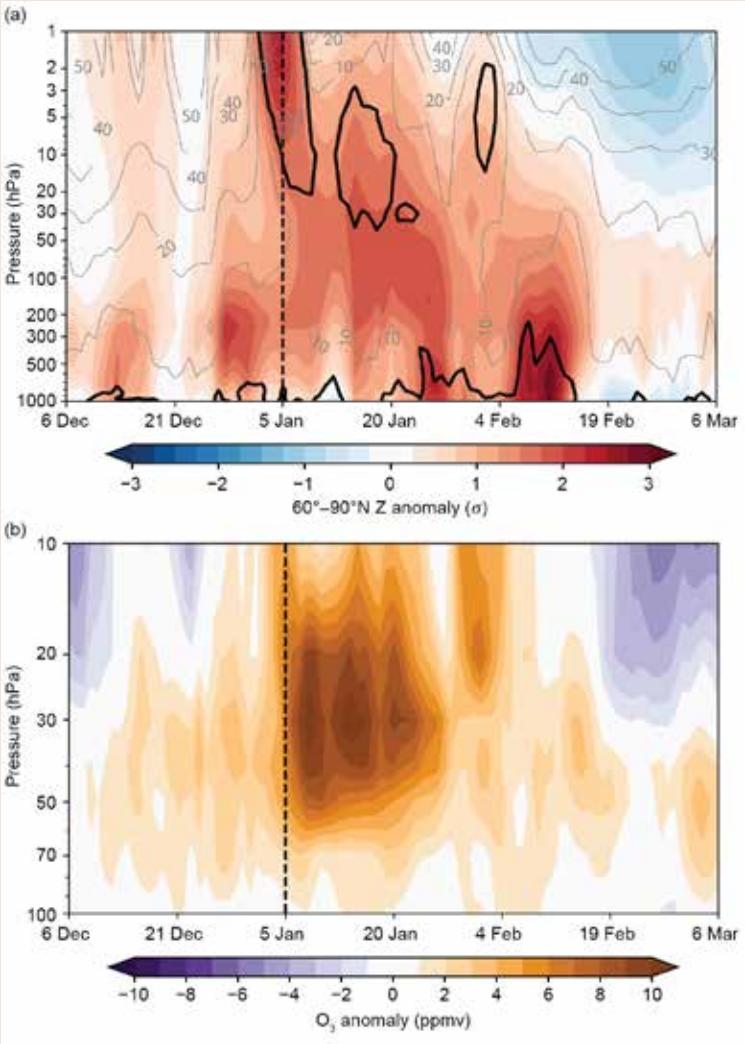

Fig. SB5.3. The vertical coupling for 30 days before to 60 days after the 5 January 2021 SSW, shown as pressure–time cross-sections of daily-mean (a) 60°–90°N geopotential height anomalies (std. dev.; shading) and 60°N zonal-mean zonal winds (m s^{-1}; gray contours, with the zero wind line in black) from the ERA5 reanalysis, and (b) 65°–90°N ozone anomalies (ppmv) from the MERRA2 reanalysis. All anomalies are created with respect to the daily climate over 1991–2020. The geopotential height anomalies are additionally normalized at each pressure level by the standard deviation of all days in the 90-day window shown during 1991–2020. The dashed black vertical line indicates the date of the SSW.

From a peak wind speed near 44 m s^{-1} on 24 December 2020, the 10 hPa (~30 km) 60°N zonal-mean zonal winds rapidly decelerated over the next 12 days until they reversed direction on 5 January 2021, which defines the central date of the SSW (Fig. SB5.3a). During this same time, average temperatures at 10 hPa within the polar cap (latitudes ≥ 60°N) increased by about 30°C (Lee 2021).

Influence on stratospheric ozone

There can be significant changes to atmospheric composition over the Arctic when the polar vortex becomes disturbed during an SSW (de la Camara et al. 2018). The barrier that the polar vortex creates in the stratosphere between ozone-poor polar air and ozone-rich mid-latitude air is degraded by rapid mixing. Additionally, the large-scale waves that drive the SSW also accelerate the stratospheric overturning circulation, transporting more ozone from the tropical to the polar stratosphere.

These changes were evident during the 2021 SSW, with anomalously high ozone in the mid-to-lower stratosphere as the zonal-mean winds reversed direction on 5 January (Fig. SB5.3b). While the recovery of the polar vortex winds in February led to anomalously low ozone in the mid-stratosphere, anomalously high ozone persisted in the lower stratosphere through March. Given the lack of solar insolation at the pole in January when the SSW occurred, concurrent changes in ozone likely had minimal effects on UV radiation at the surface or feedbacks on the circulation (section 5j).

Influence on weather patterns and their predictability

The 2021 SSW showed a downward influence on the polar atmospheric circulation from the upper stratosphere to the surface for six weeks after the event (as is typical of most SSWs), with anomalously high geopotential heights (Fig. SB5.3a) and sea level pressure over the Arctic, and anomalously low sea level pressure over the North Atlantic (Figs. SB 5.4b,d). This pattern is a signature of the downward influence of the stratosphere and represents the negative phase of the North Atlantic Oscillation (NAO). The January NAO was at its lowest value since 2010 (Lee 2021). During the 6-week period following the SSW, surface temperatures were anomalously high over Greenland and the Canadian Arctic and anomalously low over Europe, northern Asia, and the United States, with a cold air outbreak first occurring over Europe and northern Asia during January and then over North America in the first two weeks of February (section 5b).

This SSW, like most other SSWs (Domeisen et al. 2020), was not well predicted by sub-seasonal to seasonal forecast systems more than two weeks in advance (Rao et al. 2021). However, only those forecast members that predicted a reversal of the polar vortex winds were able to predict the persistent cold anomalies over Eurasia following the event (Rao et al. 2021). Recent research (Kretschmer et al. 2018) suggests that the location of the polar vortex as the SSW evolves may be linked to where the most significant weather extremes occur. The SSW in 2021 provided at least anecdotal evidence for these effects. The coldest temperature anomalies first occurred over Eurasia in mid-January (Fig. SB5.4b), as the vortex became elongated and shifted towards that region (Fig. SB5.4a; Wright et al. 2021; Zhang et al. 2022). During this time, most of the United States was anomalously warm. As the vortex began to elongate towards Canada in early February (Fig. SB5.4c; Cohen et al. 2021), an extreme cold air outbreak occurred over the central United States (Fig. SB5.4d), leading to massive power outages, damage to infrastructure, loss of life, and economic losses estimated at $130 billion (U.S. dollars) in Texas alone (Busby et al. 2021; see section 7b2). Nonetheless, though the SSW increased the likelihood of cold-air outbreaks in the subsequent weeks (Huang et al. 2021), model experiments suggest limited direct influence of the SSW itself on the central United States cold-air outbreak (Davis et al. 2022; Zhang et al. 2022.)

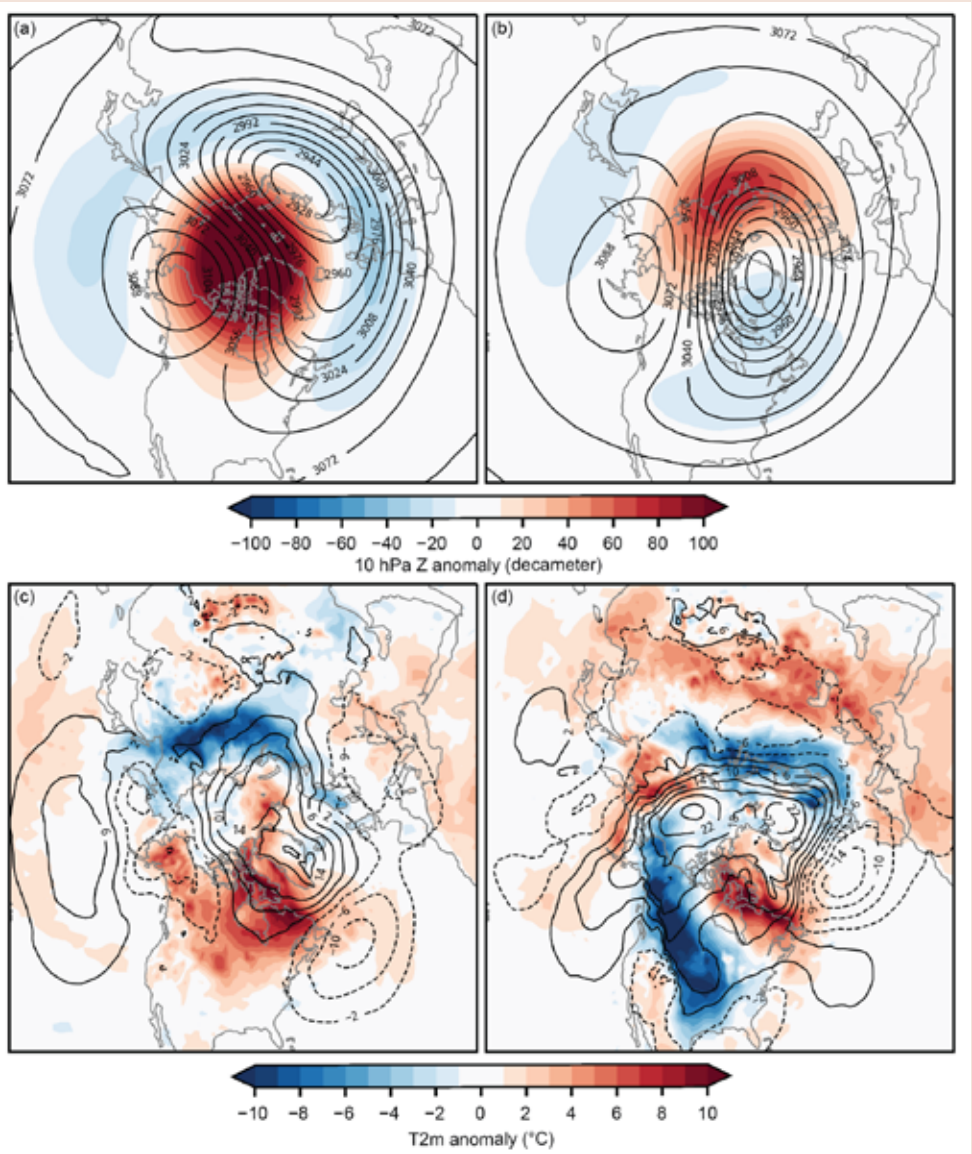

Fig. SB5.4. Stratospheric evolution and associated surface impacts of the January 2021 SSW, according to ERA5 reanalysis. Two periods following the SSW are shown, (a,b) 5–30 January and (c,d) 1–16 February. (a,c) shows the 10-hPa geopotential heights (dam; contours) and anomalies (dam; shading), while (b,d) shows the sea level pressure anomalies (hPa; contours) and near-surface (2m) temperature anomalies (°C; shading).

Acknowledgments

The editors wish to thank the six anonymous reviewers and the general editors for providing reviews of the full chapter. Their careful readthrough and thoughtful input improved each of the sections and led to better coherency between the sections.

a (Overview)

Matthew Druckenmiller and Twila Moon appreciate support from NOAA's Arctic Research Office. Rick Thoman appreciates support from NOAA's Climate Program Office.

e (Greenland ice sheet)

Data from the Programme for Monitoring of the Greenland Ice Sheet (PROMICE) were provided by the Geological Survey of Denmark and Greenland (GEUS) at http://www.promice.dk.

Twila Moon was supported by the University of Colorado Boulder Cooperative Institute for Research in Environmental Sciences. Marco Tedesco was supported by National Science Foundation ANS #1713072, National Science Foundation PLR-1603331, NASA MAP #80NSSC17K0351, NASA #NNX17AH04G, and the Heising-Simons foundation.

Thomas Mote was supported by National Science Foundation #1900324. Sentinel-3 SICE data processing via PolarView.org is made possible by the European Space Agency (ESA) Network of Resources. Summit Station is owned and operated by the National Science Foundation Office of Polar Programs with permission from the Government of Greenland. Data from land-based weather stations in Greenland were provided by the Danish Meteorological Institute, and Summit Station data provided by NOAA GEOSummit.

j (Ozone and UV radiation)

Germar Bernhard and coauthors acknowledge the support of Biospherical Instruments, San Diego; the Research Council of Norway through its Centres of Excellence funding scheme, project number 223268/F50; the Academy of Finland for supporting UV measurements through the FARPOCC, SAARA, and CHAMPS (grant no. 329225) projects; the European Space Agency for supporting the DACES project; the Norwegian Environment Agency for funding UV measurements at Andøya and Ny-Ålesund; and the European Union for supporting e-shape. The authors also would like to thank Bodeker Scientific, funded by the New Zealand Deep South National Science Challenge, for providing the combined NIWA-BS total column ozone database; the Microwave Limb Sounder team at NASA's Jet Propulsion Laboratory for data-processing and analysis support; the European Centre for medium-range weather forecasts for providing reanalysis data; and Juha M. Karhu, Tomi Karppinen, and Markku Ahponen from the Finnish Meteorological Institute for operating the Brewer UV spectroradiometer at Sodankylä.

Appendix 1: Chapter 5 – Acronyms

ALT	active layer thickness
AMJ	April, May, June
AMSR2	Advanced Microwave Scanning Radiometer
AO	Arctic Oscillation
AON	Arctic Observing Network
ARC	Arctic Report Card
AVHRR	Advanced Very High Resolution Radiometer
AWS	Automated Weather Station
B_{clim}	climatic mass balance
CALM	Circumpolar Active Layer Monitoring program
CCI	Climate Change Initiative
CRUTEM	Climatic Research Unit Temperature
DMI	Danish Meteorological Institute
DMSP	Defense Meteorological Satellite Program
DU	Dobson unit
EASE-	Grid Equal Area Scalable Earth Grid
ECMWF	European Centre for Medium-range Weather Forecasts
ERA	ECMWF Reanalysis
ESA	European Space Agency
GEUS	Geological Survey of Denmark and Greenland
GIMMS-3g+	Global Inventory Modeling and Mapping Studies 3g V1.2 dataset
GRACE	Gravity Recovery and Climate Experiment
ICESat-2	Ice, Cloud, and land Elevation 2 laser altimeter
IMS	Interactive Multisensor Snow and Ice Mapping System snow cover product
JAS	July, August, September
JFM	January, February, March
JJA	June, July, August
MaxNDVI	Maximum Normalized Difference Vegetation Index
MERRA-2	Modern-Era Retrospective Analysis for Research and Applications version 2 product
MLS	Microwave Limb Sounder
MODIS	Moderate Resolution Imaging Spectroradiometer
NCEP	National Center for Environmental Prediction
NCAR	National Center for Atmospheric Research
NDVI	Normalized Difference Vegetation Index
NSIDC	National Snow and Ice Data Center
OISSTv2	Optimum Interpolation (OI) SST Version 2 product
OMI	Ozone Monitoring Instrument
OND	October, November, December
PM	Passive Microwave
PROMICE	Program for the Monitoring of the Greenland Ice Sheet
PSC	polar stratospheric clouds

SAT	surface air temperature
SCD	snow cover duration
SCE	snow cover extent
SMB	surface mass balance
SLP	sea level pressure
SMOS	Soil Moisture and Ocean Salinity mission
SSMIS	Special Sensor Microwave Imager/Sounder
SSTs	sea surface temperature
SSW	Sudden Stratospheric Warming
SWE	snow water equivalent
TOC	Total Ozone Columns
UV	Ultraviolet
UVI	Ultraviolet Index
VIIRS	Visible Infrared Imaging Radiometer Suite
VIR	Visible and Infrared

References

Abramov, A., and Coauthors, 2021: Two decades of active layer thickness monitoring in northeastern Asia. *Polar Geogr.*, **44**, 186–202, https://doi.org/10.1080/1088937X.2019.1648581.

Andersen, J. K., and Coauthors, 2019: Update of annual calving front lines for 47 marine terminating outlet glaciers in Greenland (1999–2018). *Geol. Surv. Denmark Greenl. Bull.*, **43**, e2019430202, https://doi.org/10.34194/GEUSB-201943-02-02.

Andreassen, L. M., H. Elvehøy, B. Kjøllmoen, and R. V. Engeset, 2016: Reanalysis of long-term series of glaciological and geodetic mass balance for 10 Norwegian glaciers. *Cryosphere*, **10**, 535–552, https://doi.org/10.5194/tc-10-535-2016.

Baldwin, M. P., and Coauthors, 2021: Sudden stratospheric warmings. *Rev. Geophys.*, **59**, e2020RG000708, https://doi.org/10.1029/2020RG000708.

Ballinger, T. J., and Coauthors, 2020: Surface air temperature. *Arctic Report Card 2020*, R. L. Thoman, J. Richter-Menge, and M. L. Druckenmiller, Eds., NOAA, 7 pp., https://doi.org/10.25923/gcw8-2z06.

——, and Coauthors, 2021: Surface air temperature. *Arctic Report Card 2021*, T. A. Moon, M. L. Druckenmiller, and R. L. Thoman, Eds., NOAA, 8–14, https://doi.org/10.25923/53xd-9k68.

Barnes, P. W., and Coauthors, 2019: Ozone depletion, ultraviolet radiation, climate change and prospects for a sustainable future. *Nat. Sustainability*, **2**, 569–579, https://doi.org/10.1038/s41893-019-0314-2.

Barrett, A. P., J. C. Stroeve, and M. Serreze, 2020: Arctic Ocean precipitation from atmospheric reanalyses and comparisons with North Pole drifting station records. *J. Geophys. Res. Oceans*, **125**, e2019JC015415, https://doi.org/10.1029/2019JC015415.

Barton, B. I., Y. D. Lenn, and C. Lique, 2018: Observed Atlantification of the Barents Sea causes the Polar Front to limit the expansion of winter sea ice. *J. Phys. Oceanogr.*, **48**, 1849–1866, https://doi.org/10.1175/JPO-D-18-0003.1.

Berner, L. T., and Coauthors, 2020: Summer warming explains widespread but not uniform greening in the Arctic tundra biome. *Nat. Commun.*, **11**, 4621, https://doi.org/10.1038/s41467-020-18479-5.

Bernhard, G., and Coauthors, 2015: Comparison of OMI UV observations with ground-based measurements at high northern latitudes. *Atmos. Chem. Phys.*, **15**, 7391–7412, https://doi.org/10.5194/acp-15-7391-2015.

——, R. L. McKenzie, K. Lantz, and S. Stierle, 2022: Updated analysis of data from Palmer Station, Antarctica (64° S), and San Diego, California (32° N), confirms large effect of the Antarctic ozone hole on UV radiation. *Photochem. Photobiol. Sci.*, **21**, 373–384, https://doi.org/10.1007/s43630-022-00178-3.

Bhartia, P. K., and C. W. Wellemeyer, 2002: TOMS-V8 total O3 algorithm. OMI Algorithm Theoretical Basis Document Volume II, NASA Goddard Space Flight Center Tech. Doc. ATBD-OMI-02, 15–31, https://eospso.gsfc.nasa.gov/sites/default/files/atbd/ATBD-OMI-02.pdf.

Bhatt, U. S., and Coauthors, 2021: Climate drivers of Arctic tundra variability and change using an indicators framework. *Environ. Res. Lett.*, **16**, 055019, https://doi.org/10.1088/1748-9326/abe676.

Bjella, K., 2019: Warming and thawing permafrost and impacts on infrastructure [in "State of the Climate in 2018"]. *Bull. Amer. Meteor. Soc.*, **100** (9), S157–S159, 10.1175/2019BAMSStateoftheClimate.1.

Blackwell, S., and A. Thode, 2021: Effects of noise. *The Bowhead Whale: Balaena mysticetus: Biology and Human Interactions*, J. C. George and J. G. M. Thewissen, Eds., Academic Press, 565–576, https://doi.org/10.1016/B978-0-12-818969-6.00035-2.

Bodeker, G. E., and S. Kremser, 2021: Indicators of Antarctic ozone depletion: 1979 to 2019. *Atmos. Chem. Phys.*, **21**, 5289–5300, https://doi.org/10.5194/acp-21-5289-2021.

Boike, J., and Coauthors, 2018: A 20-year record (1998–2017) of permafrost, active layer, and meteorological conditions at a High Arctic permafrost research site (Bayelva, Spitsbergen). *Earth Syst. Sci. Data*, **10**, 355–390, https://doi.org/10.5194/essd-10-355-2018.

Bolch, T., L. S. Sørensen, S. B. Simonsen, N. Mölg, H. Machguth, P. Rastner, and F. Paul, 2013: Mass loss of Greenland's glaciers and ice caps 2003–2008 revealed from ICESat laser altimetry data. *Geophys. Res. Lett.*, **40**, 875–881, https://doi.org/10.1002/grl.50270.

Box, J. E., D. van As, and K. Steffen, 2017: Greenland, Canadian and Icelandic land ice albedo grids (2000–2016). *Geol. Surv. Denmark Greenl. Bull.*, **38**, 53–56, https://doi.org/10.34194/geusb.v38.4414.

——, W. Colgan, B. Wouters, D. Burgess, S. O'Neel, L. Thomson, and S. Mernild, 2018: Global sea-level contribution from Arctic land ice: 1971–2017. *Environ. Res. Lett.*, **13**, 125012, https://doi.org/10.1088/1748-9326/aaf2ed.

——, and Coauthors, 2019: Key indicators of Arctic climate change: 1971–2017. *Environ. Res. Lett.*, **14**, 045010, https://doi.org/10.1088/1748-9326/aafc1b.

——, A. Wehrlé, D. van As, R. S. Fausto, K. K. Kjeldsen, A. Dachauer, A. P. Ahlstrøm, and G. Picard, 2022: Greenland ice sheet rainfall, heat and albedo feedback impacts from the mid-August 2021 atmospheric river. *Geophys. Res. Lett.*, **49**, e2021GL097356, https://doi.org/10.1029/2021GL097356.

Brown, J., O. J. Ferrians Jr., J. A. Heginbottom, and E. S. Melnikov, 1997: Circum-Arctic map of permafrost and ground-ice conditions. U.S. Geological Survey Circum-Pacific Map CP-45, 1:10,000,000, https://doi.org/10.3133/cp45.

Brown, R., D. Vikhamar Schuler, O. Bulygina, C. Derksen, K. Luojus, L. Mudryk, L. Wang, and D. Yang, 2017: Arctic terrestrial snow cover. *Snow, Water, Ice and Permafrost in the Arctic (SWIPA) 2017*, Arctic Monitoring and Assessment Programme, 25–64.

Brun, E., V. Vionnet, A. Boone, B. Decharme, Y. Peings, R. Valette, F. Karbou, and S. Morin, 2013: Simulation of Northern Eurasian local snow depth, mass, and density using a detailed snowpack model and meteorological reanalyses. *J. Hydrometeor.*, **14**, 203–219, https://doi.org/10.1175/JHM-D-12-012.1.

Busby, J. W., and Coauthors, 2021: Cascading risks: Understanding the 2021 winter blackout in Texas. *Energy Res. Soc. Sci.*, **77**, 102106, https://doi.org/10.1016/j.erss.2021.102106.

Butchart, N., and E. E. Remsberg, 1986: The area of the stratospheric polar vortex as a diagnostic for tracer transport on an isentropic surface. *J. Atmos. Sci.*, **43**, 1319–1339, https://doi.org/10.1175/1520-0469(1986)043<1319:TAOTSP>2.0.CO;2.

Campbell, T. K. F., T. C. Lantz, R. H. Fraser, and D. Hogan, 2021: High Arctic vegetation change mediated by hydrological conditions. *Ecosystems*, **24**, 106–121, https://doi.org/10.1007/s10021-020-00506-7.

CAVM Team, 2003: Circumpolar arctic vegetation map (1:7,500,000 scale). Conservation of Arctic Flora and Fauna (CAFF) Map No. 1, U.S. Fish and Wildlife Service, https://www.geobotany.uaf.edu/cavm/.

CHNL, 2022: Statistics page. Center for High North Logistics, Nord University, https://arctic-lio.com/category/statistics/.

Christensen, T. R., and Coauthors, 2021: Multiple ecosystem effects of extreme weather events in the Arctic. *Ecosystems*, **24** 122–136, https://doi.org/10.1007/s10021-020-00507-6.

Christiansen, H., and Coauthors, 2010: The thermal state of permafrost in the Nordic area during the International Polar Year 2007–2009. *Permafrost Periglacial Processes*, **21**, 156–181, https://doi.org/10.1002/ppp.687.

Ciracì, E., I. Velicogna, and S. Swenson, 2020: Continuity of the mass loss of the world's glaciers and ice caps from the GRACE and GRACE Follow-On missions. *Geophys. Res. Lett.*, **47**, e2019GL086926, https://doi.org/10.1029/2019GL086926.

Cohen, J., L. Agel, M. Barlow, C. Garfinkel, and I. White, 2021: Linking Arctic variability and change with extreme winter weather in the United States. *Science*, **373**, 1116–1121, https://doi.org/10.1126/science.abi9167.

Davis, N. A., J. H. Richter, A. A. Glanville, J. Edwards, and E. LaJoie, 2022: Limited surface impacts of the January 2021 sudden stratospheric warming. *Nat. Commun.*, **13**, 1136, https://doi.org/10.1038/s41467-022-28836-1.

de la Cámara, A., M. Abalos, P. Hitchcock, N. Calvo, and R. R. Garcia, 2018: Response of Arctic ozone to sudden stratospheric warmings. *Atmos. Chem. Phys.*, **18**, 16 499–16 513, https://doi.org/10.5194/acp-18-16499-2018.

Domeisen, D. I. V., and A. H. Butler, 2020: Stratospheric drivers of extreme events at the Earth's surface. *Commun. Earth Environ*., **1**, 59, https://doi.org/10.1038/s43247-020-00060-z.

——, and Coauthors, 2020: The role of the stratosphere in subseasonal to seasonal prediction: 1. Predictability of the stratosphere. *J. Geophys. Res. Atmos.*, **125**, e2019JD030920, https://doi.org/10.1029/2019JD030920.

Durre, I., X. Yin, R. S. Vose, S. Applequist, and J. Arnfield, 2016: Integrated Global Radiosonde Archive (IGRA), Version 2. Subset: IGRA 2 Monthly-Mean Files. NOAA National Centers for Environmental Information, accessed January 2022, https://doi.org/10.7289/V5X63K0Q.

EEAP, 2019: Environmental Effects and Interactions of Stratospheric Ozone Depletion, UV Radiation, and Climate Change. 2018 Assessment Report. Environmental Effects Assessment Panel, United Nations Environment Programme, 390 pp. https://ozone.unep.org/sites/default/files/2019-04/EEAP_assessment-report-2018%20%282%29.pdf.

Eisner, L. B., Y. I. Zuenko, E. O. Basyuk, L. L. Britt, J. T. Duffy-Anderson, S. Kotwicki, C. Ladd, and W. Cheng, 2020: Environmental impacts on walleye pollock (*Gadus chalcogrammus*) distribution across the Bering Sea shelf. *Deep-Sea Res. II*, **181–182**, 104881, https://doi.org/10.1016/j.dsr2.2020.104881.

Etzelmüller, B., and Coauthors, 2020: Twenty years of European mountain permafrost dynamics—The PACE legacy. *Environ. Res. Lett.*, **15**, 104070, https://doi.org/10.1088/1748-9326/abae9d.

Fausto, R. S., and Coauthors, 2021: Programme for Monitoring of the Greenland Ice Sheet (PROMICE) automatic weather station data. *Earth Syst. Sci. Data*, **13**, 3819–3845, https://doi.org/10.5194/essd-13-3819-2021.

Fetterer, F., K. Knowles, W. N. Meier, M. Savoie, and A. K. Windnagel, 2017: Sea Ice Index, version 3. National Snow and Ice Data Center, accessed 27 August 2021, https://doi.org/10.7265/N5K072F8.

Gaglioti, B. V., and Coauthors, 2021: Tussocks enduring or shrubs greening: Alternate responses to changing fire regimes in the Noatak River Valley, Alaska. *J. Geophys. Res. Biogeosci.*, **126**, e2020JG006009, https://doi.org/10.1029/2020JG006009.

GMAO, 2015: MERRA-2tavg1_2d_lnd_Nx:2d, 1-Hourly, Time-Averaged, Single-Level, Assimilation, Land Surface Diagnostics V5.12.4. Goddard Earth Sciences Data and Information Services Center, accessed 11 August 2021, https://doi.org/10.5067/RKPHT8KC1Y1T.

Heijmans, M. M. P. D., and Coauthors, 2022: Tundra vegetation change and impacts on permafrost. *Nat. Rev. Earth Environ.*, **3**, 68–84, https://doi.org/10.1038/s43017-021-00233-0.

Henson, B., and J. Masters, 2021: Western Canada burns and deaths mount after world's most extreme heat wave in modern history. Yale Climate Connections, https://yaleclimateconnections.org/2021/07/western-canada-burns-and-deaths-mount-after-worlds-most-extreme-heat-wave-in-modern-history/.

Hersbach, H., and Coauthors, 2020: The ERA5 global reanalysis. *Quart. J. Roy. Meteor. Soc.*, **146**, 1999–2049, https://doi.org/10.1002/qj.3803.

Holmes, R. M., A. I. Shiklomanov, A. Suslova, M. Tretiakov, J. W. McClelland, L. Scott, R. G. M. Spencer, and S. E. Tank, 2021: River discharge. *Arctic Report Card 2021*, T. A. Moon, M. L. Druckenmiller, and R. L. Thoman, Eds., NOAA, 78–84, https://doi.org/10.25923/zevf-ar65.

Huang, J., P. Hitchcock, A. C. Maycock, C. M. McKenna, and W. Tian, 2021: Northern Hemisphere cold air outbreaks are more likely to be severe during weak polar vortex conditions. *Commun. Earth Environ.*, **2**, 147, https://doi.org/10.1038/s43247-021-00215-6.

Huemmrich, K. F., S. Vargas Zesati, P. Campbell, and C. Tweedie, 2021: Canopy reflectance models illustrate varying NDVI responses to change in high latitude ecosystems. *Ecol. Appl.*, **31**, e02435, .

Hugonnet, R., and Coauthors, 2021: Accelerated global glacier mass loss in the early twenty-first century. *Nature*, **592**, 726–731, https://doi.org/10.1038/s41586-021-03436-z.

Humpert, M., 2021: Winter transits along the Northern Sea Route open up a new frontier in Arctic shipping. Arctic Today, 25 January, https://www.arctictoday.com/winter-transits-along-the-northern-sea-route-open-up-a-new-frontier-in-arctic-shipping/.

IMO, 2021: Prevention of pollution by garbage from ships. International Maritime Organization, accessed 7 June 2022, https://www.imo.org/en/OurWork/Environment/Pages/Garbage-Default.aspx.

IPCC, 2021: *Climate Change 2021: The Physical Science Basis*. V. Masson-Delmotte et al., Eds., Cambridge University Press, 3949 pp., https://doi.org/10.1017/9781009157896.

Ivanova, N., O. M. Johannessen, L. T. Pedersen, and R. T. Tonboe, 2014: Retrieval of Arctic sea ice parameters by satellite passive microwave sensors: A comparison of eleven sea ice concentration algorithms. *IEEE Trans. Geosci. Remote Sens.*, **52**, 7233–7246, https://doi.org/10.1109/TGRS.2014.2310136.

Karlsen, S. R., L. Stendardi, H. Tømmervik, L. Nilsen, I. Arntzen, and E. J. Cooper, 2021: Time-series of cloud-free Sentinel-2 NDVI data used in mapping the onset of growth of central Spitsbergen, Svalbard. *Remote Sens.*, **13**, 3031, https://doi.org/10.3390/rs13153031.

Kaverin, D., and Coauthors, 2021: Long-term active layer monitoring at CALM sites in the Russian European North. *Polar Geogr.*, **44**, 203–216, https://doi.org/10.1080/1088937X.2021.1981476.

Kjøllmoen, B., L. Andreassen, H. Elvehøy, and K. Melvold, 2021: Glaciological investigations in Norway 2021. NVE Rep. 33/2021, 92 pp., https://publikasjoner.nve.no/rapport/2021/rapport2021_31.pdf.

Kokhanovsky, A., J. E. Box, B. Vandecrux, K. D. Mankoff, M. Lamare, A. Smirnov, and M. Kern, 2020: The determination of snow albedo from satellite measurements using fast atmospheric correction technique. *Remote Sens.*, **12**, 234, https://doi.org/10.3390/rs12020234.

Kretschmer, M., J. Cohen, V. Matthias, J. Runge, and D. Coumou, 2018: The different stratospheric influence on cold-extremes in Eurasia and North America. *npj Climate Atmos. Sci.*, **1**, 44, https://doi.org/10.1038/s41612-018-0054-4.

Kropp, H., and Coauthors, 2021: Shallow soils are warmer under trees and tall shrubs across Arctic and Boreal ecosystems. *Environ. Res. Lett.*, **16**, 015001, https://doi.org/10.1088/1748-9326/abc994.

Lavergne, T., and Coauthors, 2019: Version 2 of the EUMETSAT OSI SAF and ESA CCI sea-ice concentration climate data records. *Cryosphere*, **13**, 49–78, https://doi.org/10.5194/tc-13-49-2019.

Lawrence, Z. D., J. Perlwitz, A. H. Butler, G. L. Manney, P. A. Newman, S. H. Lee, and E. R. Nash, 2020: The remarkably strong Arctic stratospheric polar vortex of winter 2020: Links to record-breaking Arctic oscillation and ozone loss. *J. Geophys Res. Atmos*, **125**, e2020JD033271, https://doi.org/10.1029/2020JD033271.

Lee, S. H., 2021: The January 2021 sudden stratospheric warming. *Weather*, **76**, 135–136, https://doi.org/10.1002/wea.3966.

Lind, S., R. B. Ingvaldsen, and T. Furevik, 2018: Arctic warming hotspot in the northern Barents Sea linked to declining sea ice import. *Nat. Climate Change*, **8**, 634–639, https://doi.org/10.1038/s41558-018-0205-y.

Lu, Q., J. Rao, Z. Liang, D. Guo, J. Luo, S. Liu, C. Wang, and T. Wang, 2021: The sudden stratospheric warming in January 2021. *Environ. Res. Lett.*, **16**, 084029, https://doi.org/10.1088/1748-9326/ac12f4.

Luojus, K., and Coauthors, 2020: ESA Snow Climate Change Initiative (Snow_cci): Snow Water Equivalent (SWE) level 3C daily global climate research data package (CRDP) (1979 – 2018), version 1.0. Centre for Environmental Data Analysis, accessed 19 July 2021, https://doi.org/10.5285/fa20aaa2060e40cabf5fedce7a9716d0.

Łupikasza, E. B., and K. Cielecka-Nowak, 2020: Changing probabilities of days with snow and rain in the Atlantic sector of the Arctic under the current warming trend. *J. Climate*, **33**, 2509–2532, https://doi.org/10.1175/JCLI-D-19-0384.1.

Magnússon, R. Í., 2021: Shrub decline and expansion of wetland vegetation revealed by very high resolution land cover change detection in the Siberian lowland tundra. *Sci. Total Environ.*, **782**, 146877, https://doi.org/10.1016/j.scitotenv.2021.146877.

Malkova, G., and Coauthors, 2022: Spatial and temporal variability of permafrost in the western part of the Russian Arctic. *Energies*, **15**, 2311, https://doi.org/10.3390/en15072311.

Mankoff, K. D., A. Solgaard, W. Colgan, A. P. Ahlstrøm, S. A. Khan, and R. S. Fausto, 2020: Greenland Ice Sheet solid ice discharge from 1986 through March 2020. *Earth Syst. Sci. Data*, **12**, 1367–1383, https://doi.org/10.5194/essd-12-1367-2020.

Manney, G. L., Z. D. Lawrence, M. L. Santee, N. J. Livesey, A. Lambert, and M. C. Pitts, 2015a: Polar processing in a split vortex: Arctic ozone loss in early winter 2012/2013. *Atmos. Chem. Phys.*, **15**, 5381–5403, https://doi.org/10.5194/acp-15-5381-2015.

——, and Coauthors, 2015b: A minor sudden stratospheric warming with a major impact: Transport and polar processing in the 2014/2015 Arctic winter. *Geophys. Res. Lett.*, **42**, 7808–7816, https://doi.org/10.1002/2015GL065864.

——, and Coauthors, 2020: Record-low Arctic stratospheric ozone in 2020: MLS observations of chemical processes and comparisons with previous extreme winters. *Geophys. Res. Lett.*, **47**, e2020GL089063, https://doi.org/10.1029/2020GL089063.

McCrystall, M. R., J. Stroeve, M. Serreze, B. C. Forbes, and J. A. Screen, 2021: New climate models reveal faster and larger increases in Arctic precipitation than previously projected. *Nat. Commun.*, **12**, 6765, https://doi.org/10.1038/s41467-021-27031-y.

Meier, W. N., F. Fetterer, A. K. Windnagel, and J. S. Stewart, 2021a: NOAA/NSIDC climate data record of passive microwave sea ice concentration, version 4. Subset: 1982–2021, National Snow and Ice Data Center, accessed 11 February 2022, https://doi.org/10.7265/efmz-2t65.

——, ——, ——, and ——, 2021b: Near-real-time NOAA/NSIDC climate data record of passive microwave sea ice concentration, version 2. Subset: 1982–2021, accessed 11 February 2022, https://doi.org/10.7265/tgam-yv28.

Mekonnen, Z. A., and Coauthors, 2021: Arctic tundra shrubification: A review of mechanisms and impacts on ecosystem carbon balance. *Environ. Res. Lett.*, **16**, 053001, https://doi.org/10.1088/1748-9326/abf28b.

Meredith, M., and Coauthors, 2019: Polar regions. *IPCC Special Report on the Ocean and Cryosphere in a Changing Climate*, H.-O. Pörtner et al., Eds., Cambridge University Press, 203–320, https://www.ipcc.ch/srocc/.

Millan, R., J. Mouginot, and E. Rignot, 2017: Mass budget of the glaciers and ice caps of the Queen Elizabeth Islands, Canada from 1991-2015. *Environ. Res. Lett.*, **12**, 024016, .

Moon, T. A., and Coauthors, 2021: Greenland Ice Sheet. *Arctic Report Card 2021*, T. A. Moon, M. L. Druckenmiller, and R. L. Thoman, Eds., NOAA, 23–31, https://doi.org/10.25923/546g-ms61.

Morlighem, M., and Coauthors, 2017: BedMachine v3: Complete bed topography and ocean bathymetry mapping of Greenland from multibeam echo sounding combined with mass conservation. *Geophys. Res. Lett.*, **44**, 11 051–11 061, https://doi.org/10.1002/2017GL074954.

Mote, T., 2007: Greenland surface melt trends 1973–2007: Evidence of a large increase in 2007. *Geophys. Res. Lett.*, **34**, L22507, https://doi.org/10.1029/2007GL031976.

Müller, R., J.-U. Grooß, C. Lemmen, D. Heinze, M. Dameris, and G. Bodeker, 2008: Simple measures of ozone depletion in the polar stratosphere. *Atmos. Chem. Phys.*, **8**, 251–264, https://doi.org/10.5194/acp-8-251-2008.

Muñoz Sabater, J., 2019: ERA5-Land hourly data from 1981 to present. Copernicus Climate Change Service (C3S) Climate Data Store (CDS), accessed 11 August 2021, https://doi.org/10.24381/cds.e2161bac.

Myers-Smith, I. H., and Coauthors, 2020: Complexity revealed in the greening of the Arctic. *Nat. Climate Change*, **10**, 106–117, https://doi.org/10.1038/s41558-019-0688-1.

Nyland, K. E., N. I. Shiklomanov, D. A. Streletskiy, F. E. Nelson, A. E. Klene, and A. L. Kholodov, 2021: Long-term Circumpolar Active Layer Monitoring (CALM) program observations in northern Alaskan tundra. *Polar Geogr.*, **44**, 167–185, https://doi.org/10.1080/1088937X.2021.1988000.

PAME, 2019: Underwater noise in the Arctic: A state of knowledge report. Protection of the Arctic Marine Environment Secretariat, 58 pp., https://www.pame.is/projects/arctic-marine-shipping/underwater-noise-in-the-arctic.

Parmentier, F.-J. W., L. Nilsen, H. Tømmervik, and E. J. Cooper, 2021: A distributed time-lapse camera network to track vegetation phenology with high temporal detail and at varying scales. *Earth Syst. Sci. Data*, **13**, 3593–3606, https://doi.org/10.5194/essd-13-3593-2021.

Peltier, W. R., D. F. Argus, and R. Drummond, 2018: Comment on "An assessment of the ICE-6G_C (VM5a) glacial isostatic adjustment model" by Purcell et al. *J. Geophys. Res. Solid Earth*, **123**, 2019–2028, https://doi.org/10.1002/2016JB013844.

Peng, G., W. N. Meier, D. J. Scott, and M. H. Savoie, 2013: A long-term and reproducible passive microwave sea ice concentration data record for climate studies and monitoring. *Earth Syst. Sci. Data*, **5**, 311–318, https://doi.org/10.5194/essd-5-311-2013.

Petty, A. A., N. T. Kurtz, R. Kwok, T. Markus, and T. A. Neumann, 2020: Winter Arctic sea ice thickness from ICESat-2 freeboards. *J. Geophys. Res.*, **125**, e2019JC015764, https://doi.org/10.1029/2019JC015764.

——, ——, ——, ——, and ——, 2021: ICESat-2 L4 monthly gridded sea ice thickness, version 1. National Snow and Ice Data Center Distributed Active Archive Center, accessed 9 September 2021, https://doi.org/10.5067/CV6JEXEE31HF.

Pinzon, J., and C. Tucker, 2014: A non-stationary 1981–2012 AVHRR NDVI3g time series. *Remote Sens.*, **6**, 6929–6960, https://doi.org/10.3390/rs6086929.

Ponomarev, E., A. Zabrodin, and T. Ponomareva, 2022: Classification of fire damage to boreal forests of Siberia in 2021 based on the dNBR index. *Fire*, **5**, 19, https://doi.org/10.3390/fire5010019.

Rao, J., C. I. Garfinkel, T. Wu, Y. Lu, Q. Lu, and Z. Liang, 2021: The January 2021 sudden stratospheric warming and its prediction in subseasonal to seasonal models. *J. Geophys. Res. Atmos.*, **126**, e2021JD035057, https://doi.org/10.1029/2021JD035057.

Raynolds, M. K., D. A. Walker, H. E. Epstein, J. E. Pinzon, and C. J. Tucker, 2012: A new estimate of tundra-biome phytomass from trans-Arctic field data and AVHRR NDVI. *Remote Sens. Lett.*, **3**, 403–411, https://doi.org/10.1080/01431161.2011.609188.

Reynolds, R. W., N. A. Rayner, T. M. Smith, D. C. Stokes, and W. Wang, 2002: An improved in situ and satellite SST analysis for climate. *J. Climate*, **15**, 1609–1625, https://doi.org/10.1175/1520-0442(2002)015<1609:AIISAS>2.0.CO;2.

——, T. M. Smith, C. Liu, D. B. Chelton, K. S. Casey, and M. G. Schlax, 2007: Daily high-resolution-blended analyses for sea surface temperature. *J. Climate*, **20**, 5473–5496, https://doi.org/10.1175/2007JCLI1824.1.

Ricker, R., S. Hendricks, L. Kaleschke, X. Tian-Kunze, J. King, and C. Haas, 2017: A weekly Arctic sea-ice thickness data record from merged CryoSat-2 and SMOS satellite data. *Cryosphere*, **11**, 1607–1623, https://doi.org/10.5194/tc-11-1607-2017.

RGI Consortium, 2017: Randolph glacier inventory—A dataset of global glacier outlines, version 6. National Snow and Ice Data Center, https://doi.org/10.7265/4m1f-gd79

Robinson, D. A., T. W. Estilow, and NOAA CDR Program, 2012: NOAA Climate Data Record (CDR) of Northern Hemisphere (NH) Snow Cover Extent (SCE), version 1 [r01]. NOAA National Centers for Environmental Information, https://doi.org/10.7289/V5N014G9.

Rolland, R. M., S. E. Parks, K. E. Hunt, M. Castellote, P. J. Corkeron, D. P. Nowacek, S. K. Wasser, and S. D. Kraus, 2012: Evidence that ship noise increases stress in right whales. *Proc. Roy. Soc.*, **B279**, 2363–2368, https://doi.org/10.1098/rspb.2011.2429.

Romanovsky, V., and Coauthors, 2017: Changing permafrost and its impacts. Snow, Water, Ice and Permafrost in the Arctic (SWIPA) 2017, Arctic, Monitoring and Assessment Programme, 65–102, https://www.amap.no/documents/doc/snow-water-ice-and-permafrost-in-the-arctic-swipa-2017/1610.

Schaaf, C. B., 2021: MCD43A4 v006 MODIS/Terra+Aqua Nadir BRDF-Adjusted Reflectance (NBAR) Daily L3 Global 500 m SIN Grid, accessed 1 September 2021, https://doi.org/10.5067/MODIS/MCD43A4.006.

Schuur, E. A. G., 2020: Permafrost carbon [in "State of the Climate in 2019"]. *Bull. Amer. Meteor. Soc.*, **101** (8), S270–S271, https://doi.org/10.1175/BAMS-D-20-0086.1.

Seider, J. H., T. C. Lantz, T. Hermosilla, M. A. Wulder, and J. A. Wang, 2022: Biophysical determinants of shifting tundra vegetation productivity in the Beaufort Delta region of Canada. *Ecosystems*, https://doi.org/10.1007/s10021-021-00725-6, in press.

Severson, J. P., H. E. Johnson, S. M. Arthur, W. B. Leacock, and M. J. Suitor, 2021: Spring phenology drives range shifts in a migratory Arctic ungulate with key implications for the future. *Global Change Biol.*, **27**, 4546–4563, https://doi.org/10.1111/gcb.15682.

Sharp, M., D. Burgess, J. Cogley, M. Ecclestone, C. Labine, and G. Wolken, 2011: Extreme melt on Canada's Arctic ice caps in the 21st century. *Geophys. Res. Lett.*, **38**, L11501, https://doi.org/10.1029/2011GL047381.

Sheffield, G., A. Ahmasuk, F. Ivanoff, A. Noongwook, and J. Koonooka, 2021: 2020 foreign marine debris event–Bering Strait. *Arctic Report Card 2021*, T. A. Moon, M. L. Druckenmiller, and R. L. Thoman, Eds., NOAA, 85–92, https://doi.org/10.25923/jwag-eg41.

Shiklomanov, N. I., D. A. Streletskiy, and F. E. Nelson, 2012: Northern Hemisphere component of the global Circumpolar Active Layer Monitoring (CALM) program. *Proc. 10th Int. Conf. on Permafrost*, Vol. 1, Salekhard, Russia, Tyumen Oil and Gas University, 377–382.

Smedsrud, L. H., and Coauthors, 2022: Nordic Seas heat loss, Atlantic inflow, and Arctic sea ice cover over the last century. *Rev. Geophys.*, **60**, e2020RG000725, https://doi.org/10.1029/2020RG000725.

Smith, R. B., 2021: Russian tanker passes through Bering Strait in the midst of winter. *The Nome Nugget*, 15 January, http://www.nomenugget.com/news/russian-tanker-passes-through-bering-strait-midst-winter.

Smith, S. L., and Coauthors, 2021: Permafrost [in "State of the Climate in 2020"]. *Bull. Amer. Meteor. Soc.*, **102** (8), S293–S297, https://doi.org/10.1175/BAMS-D-21-0086.1.

——, H. B. O'Neill, K. Isaksen, J. Noetzli, and V. E. Romanvsky, 2022: The changing thermal state of permafrost. *Nat. Rev. Earth Environ.*, **3**, 10–23, https://doi.org/10.1038/s43017-021-00240-1.

Spies, I., K. M. Gruenthal, D. P. Drinan, A. B. Hollowed, D. E. Stevenson, C. M. Tarpey, and L. Hauser, 2020: Genetic evidence of a northward range expansion in the eastern Bering Sea stock of Pacific cod. *Evol. Appl.*, **13**, 362–375, https://doi.org/10.1111/eva.12874.

Stafford, K. M., 2021: The changing Arctic marine soundscape. *Arctic Report Card 2021*, T.A. Moon, M. L. Druckenmiller, and R. L. Thoman, Eds., NOAA, 102–108, https://doi.org/10.25923/jagc-4a84.

Stevenson, D. E., and R. R. Lauth, 2019: Bottom trawl surveys in the northern Bering Sea indicate recent shifts in the distribution of marine species. *Polar Biol.*, **42**, 407–421, https://doi.org/10.1007/s00300-018-2431-1.

Strand, S. M., H. H. Christiansen, M. Johansson, J. Akerman, and O. Humlum, 2021: Active layer thickening and controls on interannual variability in the Nordic Arctic compared to the circum-Arctic. *Permafrost Periglacial Processes*, **32**, 47–58, https://doi.org/10.1002/ppp.2088.

Stroh, J. N., G. Panteleev, S. Kirillov, M. Makhotin, and N. Shakhova, 2015: Sea-surface temperature and salinity product comparison against external in situ data in the Arctic Ocean. *J. Geophys. Res. Oceans*, **120**, 7223–7236, https://doi.org/10.1002/2015JC011005.

Talucci, A. C., M. M. Loranty, and H. D. Alexander, 2022: Siberian taiga and tundra fire regimes from 2001–2020. *Environ. Res. Lett.*, **17**, 025001, https://doi.org/10.1088/1748-9326/ac3f07.

Tanskanen, A., A. Arola, and J. Kujanpää, 2003: Use of the moving time-window technique to determine surface albedo from the TOMS reflectivity data. *Proc. SPIE*, **4896**, 239–250, https://doi.org/10.1117/12.483407.

Tape, K. D., J. A. Clark, B. M. Jones, H. C. Wheeler, P. Marsh, and F. Rosell, 2021. Beaver engineering: Tracking a new disturbance in the Arctic. *Arctic Report Card 2021*, T. A. Moon, M. L. Druckenmiller, and R. L. Thoman, Eds., NOAA, 66–71, https://doi.org/10.25923/0jtd-vv85.

Tervo, O., S. Blackwell, S. Ditlevsen, A. Conrad, A. Samson, E. Garde, R. Hansen, and M. P. Heide-Jørgensen, 2021: Narwhals react to ship noise and airgun pulses embedded in background noise. *Biol. Lett.*, **17**, 20210220, https://doi.org/10.1098/rsbl.2021.0220.

Thoman, R., and Coauthors, 2020: The record low Bering Sea ice extent in 2018: Content, impacts, and an assessment of the role of anthropogenic climate change. *Bull. Amer. Meteor. Soc.*, **101**, S53–S58, https://doi.org/10.1175/BAMS-D-19-0175.1.

Timmermans, M.-L., Z. M. Labe, and C. Ladd, 2020: Sea surface temperature [in "State of the Climate in 2019"]. *Bull. Amer. Meteor. Soc.*, **101** (8), S249–S251, https://doi.org/10.1175/BAMS-D-20-0086.1.

Tschudi, M., W. N. Meier, J. S. Stewart, C. Fowler, and J. Maslanik, 2019a: EASE-Grid Sea Ice Age, version 4. Subset: March 1984–2020, National Snow and Ice Data Center Distributed Active Archive Center, accessed 1 September 2021, https://doi.org/10.5067/UTAV7490FEPB.

——, ——, and ——, 2019b: Quicklook Arctic Weekly EASE-Grid Sea Ice Age, version 1. Subset: March 2021, National Snow and Ice Data Center Distributed Active Archive Center, accessed 1 September 2021, https://doi.org/10.5067/2XXGZY3DUGNQ.

——, ——, and ——, 2020: An enhancement to sea ice motion and age products at the National Snow and Ice Data Center (NSIDC). *Cryosphere*, **14**, 1519–1536, https://doi.org/10.5194/tc-14-1519-2020.

USCMTS, 2019: A ten-year projection of maritime activity in the U.S. Arctic region, 2020–2030. U.S. Committee on the Marine Transportation System, 153 pp., https://www.cmts.gov/downloads/CMTS_2019_Arctic_Vessel_Projection_Report.pdf.

U.S. National Ice Center, 2008: IMS Daily Northern Hemisphere Snow and Ice Analysis at 1 km, 4 km, and 24 km resolutions, version 1. National Snow and Ice Data Center, accessed 11 August 2021, https://doi.org/10.7265/N52R3PMC.

van As, D., R. S. Fausto, J. Cappelen, R. S. van de Wal, R. J. Braithwaite, and H. Machguth, 2016: Placing Greenland ice sheet ablation measurements in a multi-decadal context. *Geol. Surv. Denmark Greenl. Bull.*, **35**, 71–74, https://doi.org/10.34194/geusb.v35.4942.

van Huissteden, J., K. Teshebaeva, Y. Cheung, R. Í. Magnússon, H. Noorbergen, S. V. Karsanaev, T. C. Maximov, and A. J. Dolman, 2021: Geomorphology and InSAR-tracked surface displacements in an ice-rich Yedoma landscape. *Front. Earth Sci.*, **9**, 680565, https://doi.org/10.3389/feart.2021.680565.

Veremeeva, A., I. Nitze, F. Günther, G. Grosse, and E. Rivkina, 2021: Geomorphological and climatic drivers of thermokarst lake area increase trend (1999–2018) in the Kolyma Lowland Yedoma region, north-eastern Siberia. *Remote Sens.*, **13**, 178, https://doi.org/10.3390/rs13020178.

Veselkin, D. V., L. M. Morozova, and A. M. Gorbunova, 2021: Decrease of NDVI values in the southern tundra of Yamal in 2001–2018 correlates with the size of domesticated reindeer population. *Sovrem. Probl. Distantsionnogo Zondirovaniya Zemli Kosmosa*, **18**, 143–155, https://doi.org/10.21046/2070-7401-2021-18-2-143-155.

Walsh, J. E., T. J. Ballinger, E. S. Euskirchen, E. Hanna, J. Mård, J. E. Overland, H. Tangen, and T. Vihma, 2020: Extreme weather and climate events in northern areas: A review. *Earth-Sci. Rev.*, **209**, 103324, https://doi.org/10.1016/j.earscirev.2020.103324.

Wang, C., R. M. Graham, K. Wang, S. Gerland, and M. A. Granskog, 2019: Comparison of ERA5 and ERA-Interim near-surface air temperature, snowfall and precipitation over Arctic sea ice: effects on sea ice thermodynamics and evolution. *Cryosphere*, **13**, 1661–1679, https://doi.org/10.5194/tc-13-1661-2019.

Waters, J. W., and Coauthors, 2006: The Earth Observing System Microwave Limb Sounder (EOS MLS) on the Aura satellite. *IEEE Trans. Geosci. Remote Sens.*, **44**, 1075–1092, https://doi.org/10.1109/TGRS.2006.873771.

Way, R. G., and C. M. Lapalme, 2021: Does tall vegetation warm or cool the ground surface? Constraining the ground thermal impacts of upright vegetation in northern environments. *Environ. Res. Lett.*, **16**, 054077, https://doi.org/10.1088/1748-9326/abef31.

Weatherhead, B., A. Tanskanen, and A. Stevermer, 2005: Ozone and ultraviolet radiation. *Arctic Climate Impact Assessment*, Cambridge University Press, 151–182, www.amap.no/documents/download/1086/inline.

Wehrlé, A., J. E. Box, A. M. Anesio, and R. S. Fausto, 2021: Greenland bare-ice albedo from PROMICE automatic weather station measurements and Sentinel-3 satellite observations. *Geol. Surv. Denmark Greenl. Bull.*, **47**, https://doi.org/10.34194/geusb.v47.5284.

WGMS, 2021: Fluctuations of Glaciers Database. World Glacier Monitoring Service, accessed 7 May 2021, https://doi.org/10.5904/wgms-fog-2021-05.

WHO, 2002: Global Solar UV Index: A Practical Guide. WHO/SDE/OEH/02.2, 28 pp., https://apps.who.int/iris/handle/10665/42459.

——, 2018: Scientific Assessment of Ozone Depletion: 2018. Global Ozone Research and Monitoring Project Rep. 58, World Meteorological Organization, 588 pp., https://csl.noaa.gov/assessments/ozone/2018/.

Wolken, G. J., B. Wouters, M. Sharp, L. M. Andreassen, D. Burgess, J. Kohler, and B. Luks, 2020: Glaciers and ice caps outside Greenland. *Arctic Report Card 2020*, R. L. Thoman, J. Richter-Menge, and M. L. Druckenmiller, Eds., NOAA, 8 pp., https://doi.org/10.25923/nwqq-8736.

——, and Coauthors, 2021: Glacier and permafrost hazards. *Arctic Report Card 2021*, T. A. Moon, M. L. Druckenmiller, and R. L. Thoman, Eds., NOAA, 93–101, https://doi.org/10.25923/v40r-0956.

Wouters, B., A. Gardner, and G. Moholdt, 2019: Global glacier mass loss during the GRACE satellite mission (2002–2016). Front. *Earth Sci.*, **7**, https://doi.org/10.3389/feart.2019.00096.

Wright, C. J., R. J. Hall, T. P. Banyard, N. P. Hindley, I. Krisch, D. M. Mitchell, and W. J. M. Seviour, 2021: Dynamical and surface impacts of the January 2021 sudden stratospheric warming in novel Aeolus wind observations, MLS and ERA5. *Wea. Climate Dyn.*, **2**, 1283–1301, https://doi.org/10.5194/wcd-2-1283-2021.

York, A., U. S. Bhatt, E. Gargulinski, Z. Grabinski, P. Jain, A. Soja, R. L. Thoman, and R. Ziel, 2020: Wildland fire in the high northern latitudes. *Arctic Report Card 2020*, R. L. Thoman, J. Richter-Menge, and M. L. Druckenmiller, Eds., NOAA, 11 pp., https://doi.org/10.25923/2gef-3964.

Zemp, M., and Coauthors, 2019: Global glacier mass changes and their contributions to sea-level rise from 1961 to 2016. *Nature*, **568**, 382–386, https://doi.org/10.1038/s41586-019-1071-0.

Zhang, M., X.-Y. Yang, and Y. Huang, 2022: Impacts of sudden stratospheric warming on extreme cold events in early 2021: An ensemble-based sensitivity analysis. *Geophys. Res. Lett.*, **49**, e2021GL096840, https://doi.org/10.1029/2021GL096840.